

**Universidad de los Andes**

PHYSICS DEPARTMENT

MEASUREMENT AND CHARACTERIZATION OF  
GRANULATION PATTERNS IN THE IAG SOLAR FLUX  
SPECTRUM

BSc Physics Final Project

**Author:**

Claudia Alejandra Cuellar Nieto

**Advisor:**

Benjamin Oostra Vannoppen

Nov 2025

## Abstract

For decades, the solar spectrum has served as the fundamental reference for stellar spectroscopic analysis. As our nearest star, the Sun provides a unique laboratory for understanding stellar physics, with granulation patterns from convective motion offering critical insights. These patterns are characterized by three key hydrodynamic signatures: line broadening, line profile asymmetry, and the line-depth dependence of convective blueshift.

Inspired by the foundational work of David Gray, this project presents a detailed characterization of convective blueshift and a newly identified anomalous chromodependence across these three signatures, using the high-precision IAG Solar Flux Atlas. We produced a refined, blend-free list of Fe I lines, from which granulation patterns were derived with minimal scatter. Our analysis statistically justifies a spectral window of  $0.1 \text{ \AA}$  around the line core as optimal for examination. A major outcome is the establishment of color-dependent standard granulation curves across the solar spectrum. We demonstrate that the anomalous chromodependence—whereby shorter wavelength lines exhibit greater blueshifts and more positive bisector slopes for a given depth—is not caused by solar rotation. Furthermore, we provide a general characterization for the atlas’s full wavelength range: a linear bisector slope shift with depth in the near-infrared, and distinct individual granulation curves in the visible. This work not only underscores the unparalleled quality of the IAG atlas but also delivers a refined framework and a public-ready line list for future stellar spectroscopic studies.

## Acknowledgements

I want to acknowledge everyone who has helped and supported me to reach this point.

A long time ago, I was a young girl who dreamed of the stars. I never thought I would reach that goal, because I thought I wasn't smart enough, and because I was afraid of throwing away my future on a dream. Every person I met at the university gave me a new perspective and the strength to keep pursuing my dreams. This is my way of saying thank you for believing in me.

Specifically, I want to offer my sincere gratitude to my advisor, Professor Benjamin. Thank you not only for guiding me through this project, but for encouraging me during a difficult time in my life and for believing in me and my work. Thank you for always responding to the questions of a first-semester girl who just wanted to look at the stars and learn about spectrographs. Literally, for being there throughout my entire degree, for listening to me, my projects, my ideas, and my mistakes, even when he wasn't my official professor. He may not realize it, but he gave me the purpose to believe in myself and to pursue physics to the end.

To my *Liebeleid*, my lover, who supports and loves me unconditionally. Even when I didn't believe in myself, he did, and he encouraged me to take steps I never thought I would take.

To my sister, so that she can see that it is possible to achieve great things.

To Toto, who believed in me without a doubt and encouraged me to enter this career. She is with the stars now, see the great things that she knew, cause she always knew everything, I can do.

To my friend Thomas, who supported me throughout my entire degree and stayed by my side, even when things didn't seem to be working out. Thank you for all the time shared on this Path of pain, and the coffee shared.

To every person who gave me the strength to do this crazy thing, family and friends, even those who are no longer here.

And to my past self: We did it. We can see the stars now.

# Contents

<b>List of Figures</b>	<b>3</b>
<b>1 The solar granulation patterns</b>	<b>8</b>
1.1 The three signatures of convection . . . . .	8
1.2 The IAG solar flux atlas . . . . .	10
1.3 The IAG spatially resolved quiet Sun atlas . . . . .	10
1.4 Motivation and goals . . . . .	11
<b>2 Convective motion in the Sun</b>	<b>12</b>
2.1 The solar interior and the solar outer atmosphere . . . . .	12
2.2 The solar convection zone . . . . .	14
2.2.1 The Schwarzschild criterion . . . . .	15
2.3 The solar photosphere . . . . .	16
2.3.1 Static photosphere: Limb darkening phenomenon . . . . .	17
2.3.2 Dynamic photosphere: The C-curved profile bisector. . . . .	19
2.4 The three signatures of convection . . . . .	20
2.4.1 First signature of convection: Line broadening . . . . .	21
2.4.2 Second signature of convection: Line profile asymmetry . . . . .	22
2.4.3 Third signature of convection: Line depth-dependent wavelength shifts .	23
2.4.4 The third signature plot . . . . .	23
2.4.5 Convective Blueshift . . . . .	24
2.4.6 Chromodependence characterization . . . . .	25

2.5	Anomalous chromodependence . . . . .	26
<b>3</b>	<b>The blend-free list of Fe I lines</b>	<b>27</b>
3.1	Computational approach . . . . .	27
3.1.1	Statistical analysis . . . . .	28
3.2	Blend-free Fe I line Nave list . . . . .	33
3.2.1	Selection process for blend-free Fe I lines . . . . .	33
<b>4</b>	<b>The three signatures of convection</b>	<b>35</b>
4.1	The first signature: Line broadening . . . . .	35
4.1.1	Line depth-dependence of line core curvature . . . . .	35
4.2	The second signature: Line profile asymmetry . . . . .	41
4.2.1	The line core bisector slope . . . . .	41
4.3	The third signature: Line depth-dependence of wavelength shifts . . . . .	47
4.3.1	Line depth-dependence of wavelength shifts . . . . .	47
4.3.2	Line depth-dependence on excitation potential . . . . .	57
4.3.3	Characterization of chromodependence on granulation pattern . . . . .	65
<b>5</b>	<b>Wavelength and line depth dependences</b>	<b>71</b>
<b>A</b>	<b>Z-score Standardization</b>	<b>74</b>
<b>B</b>	<b>The third derivative relation</b>	<b>76</b>
<b>C</b>	<b>Visualizer for outliers</b>	<b>79</b>
C.1	Test example . . . . .	82

# List of Figures

2.1	The general structure of the Sun. Images modified from [10]. . . . .	13
2.2	The first clear photograph of the photosphere where the granulation pattern is visible taken by Janssen in 1885. Image taken from [11]. . . . .	14
2.3	Diagram for the parcel of material displaced so slowly that the only force it feels is the pressure in a direction parallel to itself, keeping it in a constant horizontal movement. Image taken from [10]. . . . .	15
2.4	A view of granulation on the Sun's surface. Image taken from [13]. . . . .	17
2.5	A time sequence showing granule evolution where the time intervals are about a minute. Image taken from [4]. . . . .	17
2.6	Simple model illustration for a spherical blackbody emitting continuous radiation $B_\nu$ , assuming that the radiation source function $S(\tau)$ varies continuously with depth.	18
2.7	Squared profile for the disk intensity at increasing wavelengths, where $5\mu m$ refers to the infrared range and $0.32\mu m$ the violet range. Image taken from [4]. . . . .	19
2.8	The C-curved line profile bisector with the corresponding diagram of wavelength displacement due to convective blueshift. Imagen taken from [3]. . . . .	20
2.9	The third signature plot for the IAG spatially resolved quiet Sun atlas, shows a strong trend blueshift in the shallow lines. Image taken from [9]. . . . .	24
2.10	Standard curve proposed by Gray and Oostra on the spectral range of $6020\text{\AA}$ to $6340\text{\AA}$ . Image taken from [16]. . . . .	25
3.1	Variance and standard deviation for several observed wavelength altering the width of the window on the fourth-order polynomial fit. . . . .	29

3.2	Plots of optimal width in the visible range for the IAG solar flux atlas. . . . .	31
3.3	Plots of optimal width in the near infrared range for the IAG solar flux atlas. . . .	32
4.1	Line core curvatures for the IAG solar flux atlas separated in wavelength ranges. .	36
4.2	Line core curvatures in the IAG solar flux atlas. For shallow lines (depth less than 0.3), while the J band for the near infrared range adjust to the general trend, the H band follows a totally different trend. . . . .	37
4.3	Linear fit applied to the range (0.0 – 0.1) of line depth in the visible range of the IAG solar flux atlas. . . . .	38
4.4	Line core curvatures for the visible range of the disk center data from the IAG spatially resolved quiet Sun atlas. . . . .	39
4.5	Linear fit applied to the range (0.0 – 0.1) of line depth in the visible range of the IAG spatially resolved quiet Sun atlas. . . . .	40
4.6	Line core bisector slopes for the IAG solar flux atlas separated in wavelength ranges. The behavior of both plots is according to the C-curved shape of the line profile bisector affected by convection movement. . . . .	42
4.7	Linear fit adjusted to the range (0.3 – 0.6) of line core bisector slopes in the IAG solar flux atlas, where an anomalous wavelength-dependence becomes evident. .	43
4.8	Line profile bisector slopes for the visible range in the IAG spatially resolved quiet Sun atlas for $\mu = 1$ . . . . .	44
4.9	Linear fit adjusted to the range (0.3 – 0.6) of line core bisector slopes in the disk-center spectrum, where also the anomalous wavelength-dependence is evident. .	45
4.10	Line depth bins of 0.1 for the visible range of the IAG solar flux atlas, where wavelength-dependence of the slopes becomes apparent. The same analysis was performed on the disk-center spectrum. . . . .	45
4.11	Individual plots of line core bisector slope against wavelength representing each bin of line depth for the visible range of the IAG solar flux atlas. . . . .	46
4.12	Individual plots of line bisector slope against wavelength representing each bin of line depth for the Spatially Resolved Quiet Sun Atlas. . . . .	47

4.13	Third signature plots obtained for both wavelength ranges in the IAG solar flux atlas, in both plots the relative velocity is wavelength-dependent. . . . .	48
4.14	Velocity bins for the relation between wavelength and line depth for the visible range in the IAG solar flux atlas. . . . .	49
4.15	Velocity bins for the relation between wavelength and line depth for the near infrared range in the IAG solar flux atlas. . . . .	50
4.16	Individual plots of line depth against wavelength representing each bin of velocity separated in natural bands J and H for the near infrared range of IAG solar flux atlas. . . . .	51
4.17	Individual plots of line depth against wavelength representing each bin of velocity in the visible range for the IAG solar flux atlas. . . . .	52
4.18	Third signature plot obtained for the visible range in the IAG spatially resolved quiet sun atlas. . . . .	53
4.19	Individual plots of line depth against wavelength representing each bin of velocity in the visible range for the IAG spatially resolved quiet Sun atlas. . . . .	54
4.20	Coefficients of each lineal fit plotted against velocity bins separated by natural bands for the near infrared range in the IAG solar flux atlas. . . . .	55
4.21	Coefficients of each linear fit plotted against velocity bins for the visible range in both atlases. . . . .	56
4.22	Relative velocity against excitation potential ( $\chi$ ) of the IAG solar flux atlas. . .	58
4.23	Velocity bins of 100 m/s across Figure 4.22, with this separation is visible the excitation potential shift across line depth. . . . .	59
4.24	Individual plots for the range (2.5 to 5.0) eV of excitation potential across line depth, representing each bin of velocity for the near infrared range of IAG solar flux atlas. . . . .	60
4.25	Individual plots for the range (2.5 to 5.0) eV of excitation potential across line depth, representing each bin of velocity for the visible range of IAG solar flux atlas. . . . .	61
4.26	Relative velocity against excitation potential of lowest energy level in the visible range for the IAG spatially resolved quiet sun atlas. . . . .	62

4.27	Individual plots for the range (2.5 to 5.0) eV of excitation potential of lowest energy level across line depth, representing each bin of velocity for the IAG spatially resolved quiet sun atlas. . . . .	63
4.28	Lineal fit coefficients for both atlases across velocity bins, the values show an increment with the velocity. In both atlas one plot mirrors the other, this is a consequence of the great uncertainty of these measurements. . . . .	64
4.29	Different color curves adjusted to a specific range of the third signature plot for the visible range in the IAG solar flux atlas. The inclination on the curves is more pronounced in the violet than the red range. . . . .	66
4.30	Different color granulation lines fitted to specific ranges on the third signature plot for the near infrared range in the Solar Flux Atlas. . . . .	67
4.31	Second order coefficients for the visible range in the Solar Flux Atlas. . . . .	68
4.32	Lineal coefficient relation for the near infrared range in the Solar Flux Atlas. . . . .	69
B.1	Illustration for the points $a$ , $b$ , $c$ and the height which defines the line Core Bisector Slope CBS (see Equation (B.1)). . . . .	76
C.1	Tools bar for the visualizer, containing a classification system of labels, the option to save images, and add to a Dataframe for dropping. . . . .	79
C.2	The messages shows the index, wavelength and classification for the line added or updated. . . . .	80
C.3	Confirmation message for save the image in format JPG of the graph with the information of the line. . . . .	80
C.4	Navigation bar for the visualizer, helps to locate a specific line or exploring the different graphs using a slider, writing box, and buttons for moves. . . . .	81
C.5	General view for the results of the first filter. It shows the line core and the fourth-order polynomial fit with the line profile bisector. . . . .	81
C.6	General view for the results of the second filter. It shows the three signatures of convection with the line profile. . . . .	82

C.7 Examples for discarded lines with the first filter of the visualizer. The line cores and line bisectors of the two plots shows one or more of the conditions presented.	86
C.8 Examples for accepted lines with the first filter of the visualizer. . . . .	87
C.9 Examples for discarded lines with the second filter of the visualizer. . . . .	90
C.10 Examples for accepted lines with the second filter of the visualizer. . . . .	91

# 1. Introduction

## The solar granulation patterns

For decades, the solar spectrum has served as the fundamental reference point for spectroscopic analysis. As our nearest star, the Sun enables detailed studies of stellar composition. However, advances in optical instrumentation have revealed previously undetected spectral details, providing new insights into fundamental solar properties. One key insight is the granulation patterns caused by convective motion, which are characterized by three distinct hydrodynamic signatures: Line broadening, line profile asymmetry, and the line-depth dependence of convective blueshift. Inspired by David Gray's foundational research, this project aims to extract the granulation patterns from the IAG Solar Flux Atlas to calculate relative velocities and perform a detailed analysis based on the three signatures of convection.

### 1.1 The three signatures of convection

The stellar spectrum serves as astronomy's primary source of information, encoding details about a star's composition and velocity. However, in some stars this spectrum is modified due to fluid motions caused by density and temperature fluctuations in the outermost layer, where each spectral line exhibits a distinct velocity shift. These persistent convective motions generate a granular structure in the solar photosphere, a phenomenon supported by extensive research (see [1, 2, 3]). The granulation in the solar photosphere was first observed as a moving granular structure by Janssen in 1885. Later, in 1901, Plaskett associated this pattern with the convective cells ob-

served in Bénard’s experiment [4], where fluids heated from below produce rising elements of hot gas convecting heat to the surface. This characteristic configuration produces three signatures of granulation in stellar spectra: Line broadening, line profile asymmetry, and line-depth dependence of convective blueshift [5], all three related to line depth. The method for quantifying these relations are known as the *granulation patterns*; which characterize the signatures mentioned above [1]. The physical origin of these patterns lies in the convective process on the solar photosphere itself.

When the Sun pushes material up through its outer layer, the spectrum exhibits a blueshift. As this material subsequently cools and falls back through the atmosphere, it produces a redshift but emits less light, making the blueshift dominant. This characteristic is called *convective blueshift*. Neutral iron (Fe I) lines are optimal for calibrating this phenomenon due to their high abundance, minimal thermal broadening, limited isotopic variation and availability of accurate laboratory measurements of natural wavelengths. Furthermore, the even number of nucleons in the most abundant isotope resulting in no hyperfine structure shown. The use of a single chemical species offers the additional advantage of retrieving natural wavelengths from a single source, thereby eliminating potential discrepancies [6]. The project used the Nave list of Fe I lines, which presented the values of laboratory measurements [7].

The study of granulation patterns has been significantly documented by David Gray, whose work has improved the precision of stellar radial velocity measurements (see [1] and references therein). This improvement stems primarily from his observation that granulation patterns in solar-type stars closely resemble the granulation pattern from the third signature of convection. The line depth-dependence of convective blueshift for different solar-type stars differing primarily by a scaling factor from the solar one. This is particularly significant given the considerable challenges of obtaining such precise measurements for other stars, which are often affected by spectral noise, stellar proper motions, and velocity uncertainties [1]. Furthermore, analyzing solar granulation patterns is crucial for validating photospheric hydrodynamic models [3], enabling improved calibration and testing of dynamic atmospheric models.

Following the motivation of treating the Sun as any other star, which does not have the angular resolution necessary to study the spatial granulation structure, the most accurate solar flux atlas

is necessary.

## 1.2 The IAG solar flux atlas

In 2016, Reiners and collaborators published the unprecedented precision *Institut für Astrophysik und Geophysik* (IAG) solar flux atlas obtained with the FTS *Fourier Transform Spectrograph* at Göttingen, simultaneously reporting convective blueshifts for a sample of Fe I lines. This atlas provides highly precise and accurate data, with radial velocity uncertainties on the order of  $\pm 10$  m/s across the wavelength range from 4050 Å to 10 650 Å. In contrast to other FTS atlases, the entire visible wavelength range was observed simultaneously using only one spectrograph setting [8].

Despite the exceptional quality of the spectrum, the first derived granulation pattern for the third signature of convection appeared notably scattered and noisy. This was attributable to a rudimentary line position measurement methodology and a poor line selection which included numerous blended features, outdated wavelength references, and incomplete spectral coverage. Even if the atlas contains the dataset for the near infrared range, no analysis was implemented on this part of the spectrum. Consequently, the full potential of the IAG solar flux atlas for determining precise convective blueshifts remains unrealized, highlighting the need for the refined analytical methods applied in this project.

## 1.3 The IAG spatially resolved quiet Sun atlas

In 2023, Ellwarth and collaborators [9] published the *Institut für Astrophysik und Geophysik* (IAG) spatially resolved quiet sun atlas, also obtained with the FTS *Fourier Transform Spectrograph* at Göttingen. This atlas has the advantage of its coverage from the disk center ( $\mu = 1.0$ ) towards the solar limb ( $\mu = 0$ ), where  $\mu = \cos(\theta)$  with  $\theta$  being the angle between the surface normal and the observer's position. This spatial resolution enables the study of how convective blueshifts vary across the solar disk due to changing projection angles, a dependence that is not observed in other stars.

The principal goal of this project is to characterize the solar granulation patterns by treating the Sun as any other star. To achieve this, the disk-integrated IAG solar flux atlas serves as our primary data source. However, a precise analysis of the relative velocities in this integrated light requires correcting for the center-to-limb variations that are uniquely quantified by the IAG spatially resolved quiet Sun atlas.

## 1.4 Motivation and goals

In the first semester of 2025, Manuel Fuentes, a physics student at the Universidad de los Andes, implemented these improvements in a computational project focused on the visible spectral range. By developing enhanced measurement techniques and employing a carefully curated line list that fully covers the visible range with updated wavelength references, Fuentes achieved significantly sharper granulation patterns than previous analyses. This work demonstrated that proper line selection and modern wavelength standards can reliably extract convective signatures from high-quality solar spectra.

Under the guidance of Professor Benjamin, the present project studies the visible range and extends the analysis into the near infrared range. This region contains spectral lines that originate from deeper photospheric layers. Although these lines are consequently weaker, they represent a rich source of information. This project also extends previous efforts by measuring the line profile asymmetry and line broadening, other spectral signs of granulation beyond convective blueshift; and exploring how these signatures depend on wavelength. This last is our principal target to characterize: The observational fact of granulation patterns showing individual behaviors with wavelength dependence.

By addressing these challenges, this project intended to produce a robust characterization of the solar granulation patterns emphasizing in the anomalous chromodependence. These efforts were guided by the central research question: What are the direct spectroscopic consequences of solar convection?

## 2. Literature Review

### Convective motion in the Sun

As previously mentioned, David Gray has significantly advanced the study of granulation patterns in the solar photosphere, with a particular focus on measuring relative velocities with high precision. This chapter explores the physical origins of the three signatures of convective motion in the solar photosphere, and how this reveals the hydrodynamics on the outermost layer.

#### 2.1 The solar interior and the solar outer atmosphere

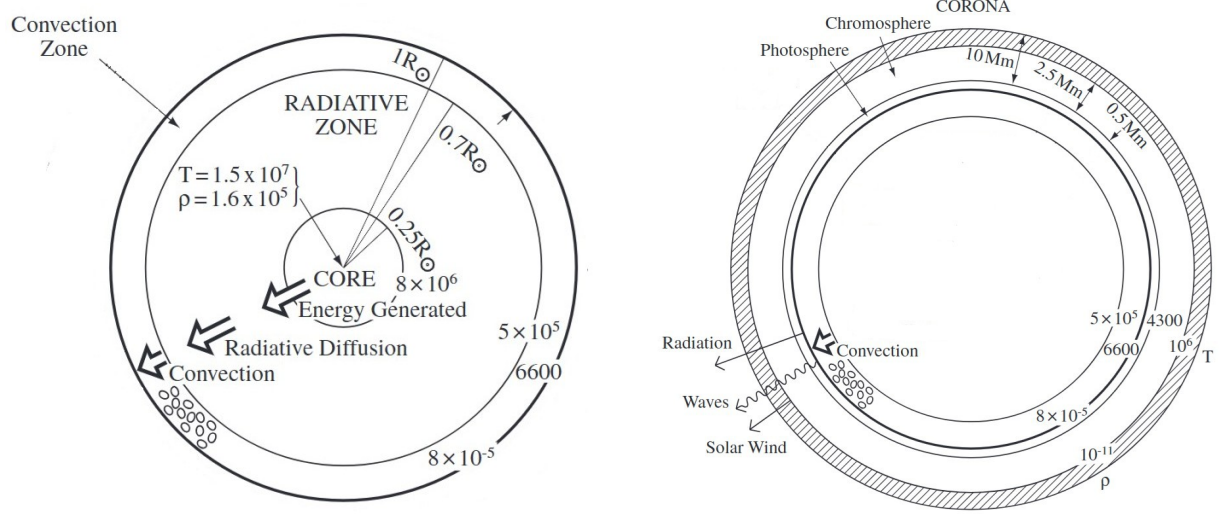
The Sun is classified as a yellow dwarf star of spectral type G2V. Its chemical structure is primarily composed of a large fraction of ionized hydrogen and a smaller proportion of helium. What makes the Sun unique in astronomical studies is its proximity to Earth, which allows for detailed observation unmatched by any other star. Structurally, the Sun is divided into two main regions: The solar interior and the solar outer atmosphere.

As illustrated in Figure 2.1a the overall structure of the solar interior is core, radiative and convective zone. In the core, He nuclei are built from H nuclei in the proton-proton chain as Equation (2.1) refers.



The proton-proton chain reaction in the core liberates approximately 26.7 MeV of energy in the form of high energy  $\gamma$ -rays, and 0.5 MeV of energy in the form of neutrinos. In this zone, standard models estimate a temperature of  $1.6 \times 10^7$  K and density to  $1.6 \times 10^5$  kg/m<sup>3</sup>. Moving outward

through the layers, both the density and temperature decrease significantly, as the energy is slowly transferred outwards by radiative diffusion [4]. This process progressively shifts the wavelength of the radiation from high energy  $\gamma$ -rays to the visible light that eventually escapes. The large temperature combined with the high density, allows the absorptions and remissions of photons that make this zone highly opaque and maintain the central material in a plasma state, functioning like a massive nuclear reactor.



(a) The interior structure of the Sun. The convection zone is responsible for the general movement that characterizes the granulation patterns.

(b) The outer structure of the Sun. The photosphere is the layer of the Sun where the convection cells overshoot from the convection zone.

Figure 2.1: The general structure of the Sun. Images modified from [10].

On the other hand, Figure 2.1b illustrates the overall structure of the solar outer atmosphere consisting of the photosphere, chromosphere and corona. In these layers, the density decreases rapidly with height above the solar surface. However, the temperature decreases to a minimum of approximately 4300 K in the upper photosphere before rising through the chromosphere and transition region to millions of degrees in the corona. From that point, the temperature falls slowly expanding outwards as the solar wind.

Nevertheless, the relevant layers for this project are the photosphere, a thin layer of plasma that emits most of the solar radiation; and the convection zone, in which all the convection process take place. The radiation chain process results on the emission of a continuous spectrum passes

through the overlying photosphere. Then specific wavelengths are absorbed for this layer, resulting in the characteristic Fraunhofer lines superimposed on the emitted spectrum, which allows observing the convection consequences [10].

## 2.2 The solar convection zone

In 1885 Janssen obtained the first clear photograph of photospheric granules (see Figure 2.2) providing the initial evidence and the starting point for numerous studies about granulation [11].

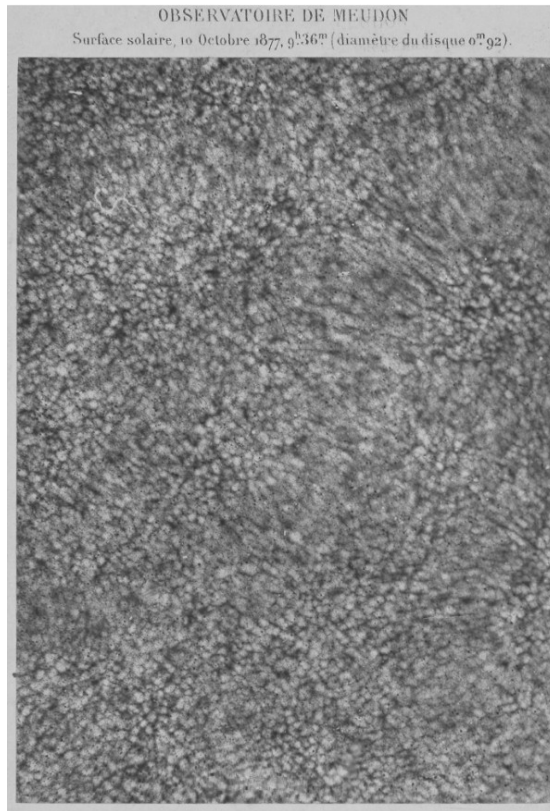


Figure 2.2: The first clear photograph of the photosphere where the granulation pattern is visible taken by Janssen in 1885. Image taken from [11].

Following the history, in 1930, Unsöld theorized that the layers beneath the photosphere should be convective unstable [4]. This hypothesis was later supported by Plaskett when he related the observed granules to the convective cells studied in Bénard's laboratory experiments [12]. In this analogy, a fluid heated from below develops rising elements of hot gas that transport heat to the

surface.

The elements of hot gas rising transporting heat are called *convective cells*, and the pattern generated by several cells on the photosphere is the *granulation* with each individual region referred to as a *granule*. Typical granules span approximately 700 km and have short lifetimes, lasting between five to ten minutes.

In the solar context, convection takes place in a highly compressible and stratified gas located between  $0.86R_\odot$  and the surface, affected by a large temperature gradient. This physical regime leads to determine the conditions required for convection to occur and the resulting dynamics of the granules [4].

### 2.2.1 The Schwarzschild criterion

Consider an elementary parcel of material displaced in local hydrostatic equilibrium with its surroundings, characterized by radial profiles of pressure  $P(r)$ , density  $\rho(r)$ , and temperature  $T(r)$ . If the granule temperature is increased to a value  $T'$ , it will expand adiabatically to maintain pressure equilibrium, thereby decreasing the density relative to its surroundings (see Figure 2.3).

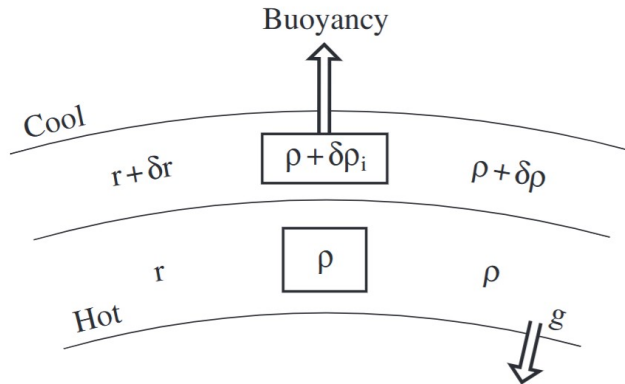


Figure 2.3: Diagram for the parcel of material displaced so slowly that the only force it feels is the pressure in a direction parallel to itself, keeping it in a constant horizontal movement. Image taken from [10].

This convective cell experiences a buoyancy force, causing it to rise. The buoyancy force persists until the granule's density matches that of its new surroundings after traveling a length  $l$ .

Let  $T'_n$  be the temperature of the rising element and  $T_n$  the temperature of its new surroundings. The difference between the adiabatic gradient of the element and the radiative gradient of the surroundings governs the convection, as described by Equation (2.2)

$$T_n = T + \left( \frac{dT}{dr} \right)_R l \quad | \quad T'_n = T' + \left( \frac{dT}{dr} \right)_{ad} l \quad (2.2)$$

Where  $R$  refers for radiative temperature gradient and  $ad$  for the adiabatic temperature gradient. The onset of convection leads to the inequality (2.3), where two conditions can arise: The granulation is established when adiabatic gradient exceeds the radiative gradient; otherwise, the layer is stable and energy is transported by radiation.

$$-\left( \frac{dT}{dr} \right)_R > \left( \frac{dT}{dr} \right)_{ad} \quad (2.3)$$

If the granulation is established, the element continues to expand adiabatically as it rises, driven by buoyancy. Otherwise, if the layer is stable, the element will contract, becomes heavier than its surroundings and begins to move down toward its original position.

This onset of instability, when the vertical temperature gradient is too large, is known as the Schwarzschild criterion for convection. Conveniently this criterion is expressed in terms of the relation between  $T$ ,  $P$  and  $\gamma$  (heat capacity ratio) for an adiabatic change (see Equation (2.4)).

$$-\left( \frac{dT}{dr} \right)_R > \frac{\gamma - 1}{\gamma} \left( \frac{T}{P} \right) \left( -\frac{dP}{dr} \right)_{ad} \quad (2.4)$$

In this form, the condition establishes that convection can occur when opacity rises rapidly, due to increasing the population of  $n = 3$  level of hydrogen and  $\gamma$  lowered by ionization. The material and energy transported by this process ended on the low photosphere, where the granules exhibit different properties that will be examined in subsequent sections.

## 2.3 The solar photosphere

As mentioned in the previous section, the observation of this layer leads to the study of dynamics and reactions within Sun's outermost layer. From surface observations a distinct pattern of granules with dynamic behavior is apparent, where individual cells continuously emerge and disappear (see Figure 2.4).

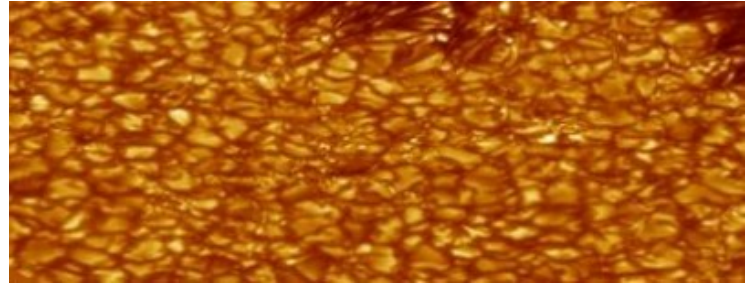


Figure 2.4: A view of granulation on the Sun’s surface. Image taken from [13].

The bright areas of granules correspond to regions where hot gas rises through the solar atmosphere. As this gas releases energy in the form of photons at the photosphere, it cools and subsequently descends, creating the darker regions of intergranular lanes [14]. Furthermore, high-resolution observations reveal that these granules are in continual motion generating asymmetries in absorption line profiles (see Figure 2.5).

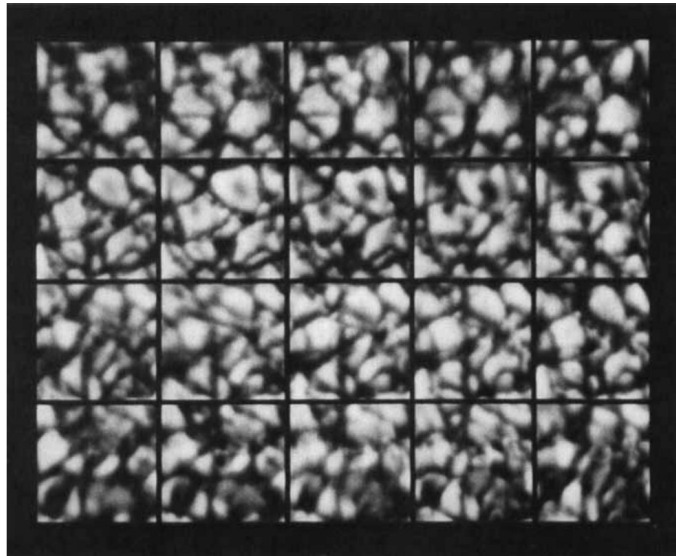


Figure 2.5: A time sequence showing granule evolution where the time intervals are about a minute. Image taken from [4].

### 2.3.1 Static photosphere: Limb darkening phenomenon

Because the temperature decreases outward through the photospheric layers, the observed intensity falls off towards the solar limb. Discovered by Halm in 1907 [3], this effect is known as *limb*

*darkening*. A simple model is presented to explain this phenomenon in detail. To explain in detail this phenomenon a simple model is presented.

Consider the Sun as a spherical blackbody emitting continuous radiation at a specific intensity  $B_\nu$ , surrounded by a shallow, light-absorbing atmosphere with an optical thickness  $\tau_\nu$ . Assume that the radiation source function  $S(\tau)$  varies continuously with depth (see Figure 2.6).

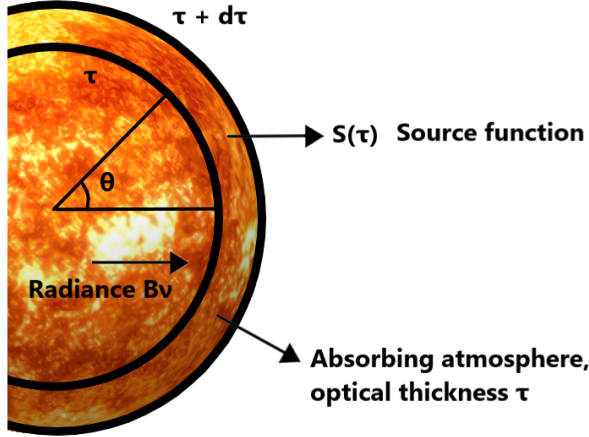


Figure 2.6: Simple model illustration for a spherical blackbody emitting continuous radiation  $B_\nu$ , assuming that the radiation source function  $S(\tau)$  varies continuously with depth.

As illustrated in Figure 2.6, the radiance from an elemental shell of optical thickness  $d\tau$  in the direction  $\theta$  is  $d\tau$  is  $S(\tau) \sec(\theta)d\tau$ . By the time the radiation from this shell reaches the photosphere, it has been reduced by an exponential factor. Taking this reduction into account, the specific intensity is described by Equation (2.5).

$$I(\theta) = \sec(\theta) \int_0^\infty S(\tau) e^{-\tau \sec(\theta)} d\tau \quad (2.5)$$

This Equation (2.5) describes limb darkening as a function of how the source function varies with optical depth [15]. At the disk center, we can see deeper into the photosphere. But near to the limb, we see less deeply so the light is weaker and redder. The resulting effect causes the disk intensity profile to appear more squared at increasing wavelength (see Figure 2.7).

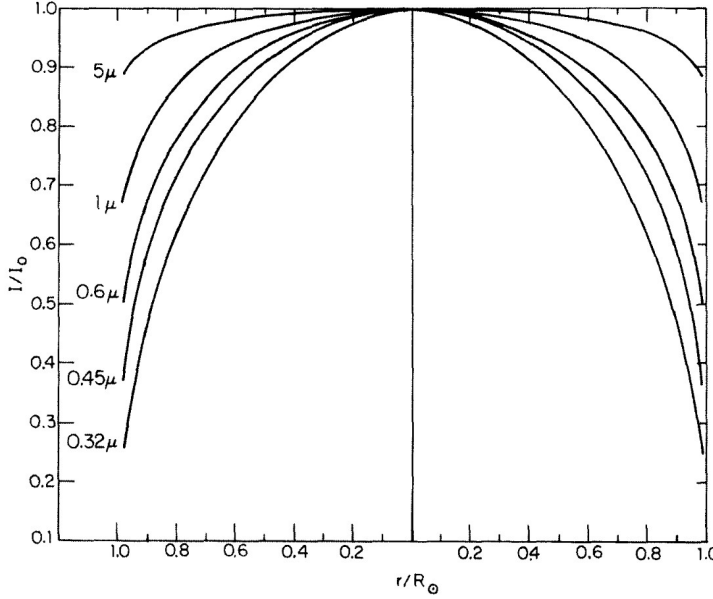


Figure 2.7: Squared profile for the disk intensity at increasing wavelengths, where  $5\mu m$  refers to the infrared range and  $0.32\mu m$  the violet range. Image taken from [4].

For typical weaker lines, the convective blueshift diminishes toward the limb, with a net velocity change approximately of 400 m/s. As explained by Ellwarth et al. observations closer to the limb pass through the atmosphere from a shallower angle, resulting in longer optical paths through high atmospheric layers which allows the study of the layers where convective blueshift is less pronounced [9]. Because of this phenomenon and following the objective of studying the line depth-dependence of convective blueshift, the center disk flux spectrum was taken as reference for analysis, where the limb darkening effect is negligible.

### 2.3.2 Dynamic photosphere: The C-curved profile bisector.

Analysis of changes, contrast and velocity field in the granulation structure have been inferred indirectly from observations of Fraunhofer line profile shapes [4]. The observations on absorption lines reveal that velocity of a rising granule decays less rapidly than its excess brightness, resulting in a characteristic C-shaped line profile bisector (see Figure 2.8).

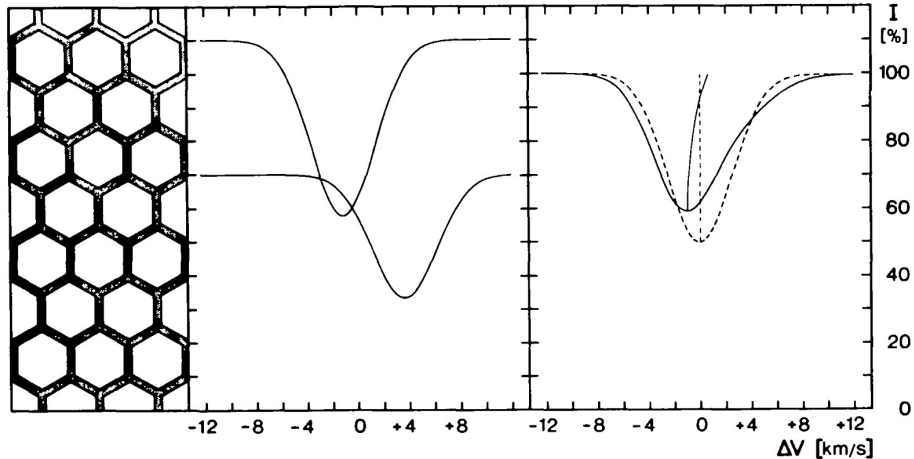


Figure 2.8: The C-curved line profile bisector with the corresponding diagram of wavelength displacement due to convective blueshift. Imagen taken from [3].

The formation of the C-curved line profile bisector occurs in three stages, corresponding to different heights in the photosphere.

First, the deepest part of the line profile is formed higher up, in a region of decelerated upflow, producing a smaller blueshift. Then, the mid-depth portion is formed in the brightest upflowing material, resulting in a blueshift. Finally, the line profile wings where the opacity is lowest, tend to be formed deepest in the cool material, producing a redshift.

This dynamic process induces characteristic asymmetries on the line profile bisector, which becomes an important instrument to measure convection process in the solar atmosphere.

## 2.4 The three signatures of convection

The three signatures of convection in stars are described by David Gray in his research as the principal characteristics to identify the convective motion through the spectrum (see [1, 16, 5] and references therein).

### 2.4.1 First signature of convection: Line broadening

To explain the line broadening is necessary establish the process that creates a spectral line. An individual atom making a transition between energy levels emits a photon with certain frequency. This transition can be represented as a graph of radiance or intensity per unit wavelength against wavelength, what is called *line profile* [14]. The radiated intensity can be modeled passing through a hot cloud of gas in thermal equilibrium as Equation (2.6).

$$I_\nu(\tau_\nu) = I_0 e^{-\tau_\nu} + B_\nu (1 - e^{-\tau_\nu}) \quad (2.6)$$

Where  $\tau_\nu$  refers to the line depth and  $B_\nu$  the absorption coefficient for the gas. The dynamical and atomic processes on the photosphere causes the thermal, convection, rotation, pressure, Stark, Zeeman and natural broadening effects. Because we measure the broadening of the line cores, which is affected mostly by Doppler effects, whereas pressure and natural broadening affect the wings, and Zeeman is negligible except in sunspots; only the thermal, rotation and convection broadening effects were studied.

Atoms in a gas have random motions with temperature dependence, which mean speed is obtained by the relation between kinetic and thermal energy for gasses [17]. The fraction of atoms in a speed interval between  $v$  and  $v + \Delta v$  is then given by the Maxwell-Boltzmann distribution in Equation (2.7).

$$f(v_{\text{rad}}) = \exp\left(\frac{-mv_{\text{rad}}^2}{2k_B T}\right) \quad (2.7)$$

Comparing with a typical Gaussian distribution centered on the origin, we can relate the width ( $\sigma^2$ ) to the variance of the radial velocity (see Equation (2.8)).

$$f(x) = \exp\left(\frac{-x^2}{2\sigma^2}\right) \rightarrow \langle v_{\text{rad}}^2 \rangle = \sigma^2 = \frac{k_B T}{m} \quad (2.8)$$

Using the relation of Doppler effect for the radial velocity and relation (2.8) the line profile with only Doppler broadening effect is described by Equation (2.9).

$$f(\Delta\lambda) = L_D \exp\left(\frac{-mc^2}{2\lambda^2 k_B T} \Delta\lambda^2\right) \quad (2.9)$$

Where  $L_D$  refers to the line depth,  $k_B$  to the Boltzmann constant; and  $c\Delta\lambda/\lambda$  to the radial velocity of the observed atom. The Equation (2.10) describes the line core curvature can be quantified

by the second derivative of the line's intensity profile with respect to wavelength, evaluated at observed wavelength.

$$\lambda_{obs}^2 \left( \frac{d^2 f(\lambda_{obs})}{d \lambda_{obs}^2} \right) \quad (2.10)$$

On a plot of  $|f''(0)|\lambda^2 / L_D$  against line depth, a theoretical slope can be derived from Equation (2.9) using the definition of line core curvature as shows the Relation (2.11).

$$|f''(0)| = L_D \left( \frac{mc^2}{2\lambda^2 k_B T} \right) \rightarrow \frac{|f''(0)|\lambda^2}{L_D} = \frac{mc^2}{2k_B T} \quad (2.11)$$

Where  $\Delta\lambda = 0$  due to the origin-centered Gaussian profile. Equation (2.11) represents the line core curvature slope for lines which are only affected by the thermal broadening effect. Directly, assuming the three target effects as independent<sup>1</sup> the variance of the total radial velocity is the sum of the variances of the thermal, rotational and convective effects. This leads to the Equation (2.12) of a theoretical slope including the three broadening effects.

$$\frac{|f''(0)|\lambda^2}{L_D} = \frac{c^2}{\langle v_r^2 \rangle + \langle v_T^2 \rangle + \langle v_{conv}^2 \rangle} \quad (2.12)$$

Where  $\langle v_r^2 \rangle$  refers to the variance of the rotation velocity;  $\langle v_T^2 \rangle$  is the variance of the thermal velocity; and  $\langle v_{conv}^2 \rangle$  refers to the variance of the convection velocity. Furthermore, the value for Fe atom mass 55.85 g/mol; the solar effective temperature 5770 K leads to the values of thermal velocity variance of 0.86 (km/s)<sup>2</sup>.

The variance of rotation velocity is 0.90 (km/s)<sup>2</sup>, this result was derived by professor Benjamin using a spherical and solid model of the Sun. In the IAG spatially resolved quiet Sun atlas the value of  $\langle v_r^2 \rangle$  is negligible. With these values, an approximation of convection variance of velocity is expected to be calculated for each atlas.

#### 2.4.2 Second signature of convection: Line profile asymmetry

According to Kirchhoff's laws, absorption line formation requires lower temperature conditions, which are found precisely in the Sun's outermost atmospheric layers [14]. These regions not

---

<sup>1</sup>This is not completely true, for it is known that greater temperatures lead to more negative convective velocities, implying a correlation between thermal and convective speeds. For simplicity, the approximation was taken on the project.

only provide the appropriate temperatures for absorption but also exhibit comparatively higher opacity. Those spectral lines from Fe I are particularly valuable for solar granulation studies due to their high abundance, minimal thermal broadening, limited isotopic variation and availability of accurate laboratory measurements of natural wavelengths [18]. Due to the useful characteristic of this line dataset, asymmetries imprinted can be quantified by analyzing their bisectors.

A convenient method for this measures involves using the third derivative of the line profile, which provides the slope of the lowest end of the bisector (see Equation (2.13)).

$$-\frac{c}{\lambda_{obs}} \left( \frac{1}{3 \left( \frac{d^2 f(\lambda_{obs})}{d \lambda_{obs}^2} \right)^2} \right) \left( \frac{d^3 f(\lambda_{obs})}{d \lambda_{obs}^3} \right) \quad (2.13)$$

The slope of the line profile is defined as zero when the line profile bisector is vertical and the line core is symmetric. The relation (2.13) is derived in appendixB.

As mentioned before, line profile asymmetries are an important instrument to measure convection processes from the solar atmosphere. Since most of stellar observations are made with lower-resolution spectrographs and often lower signal-to-noise ratios.

### 2.4.3 Third signature of convection: Line depth-dependent wavelength shifts

Many studies across the years have detected and observed the phenomenon of wavelength shifts against the line depth, or as it is called, convective blueshift.

### 2.4.4 The third signature plot

The third signature plot relates relative velocity against line depth, as shown Figure 2.9.

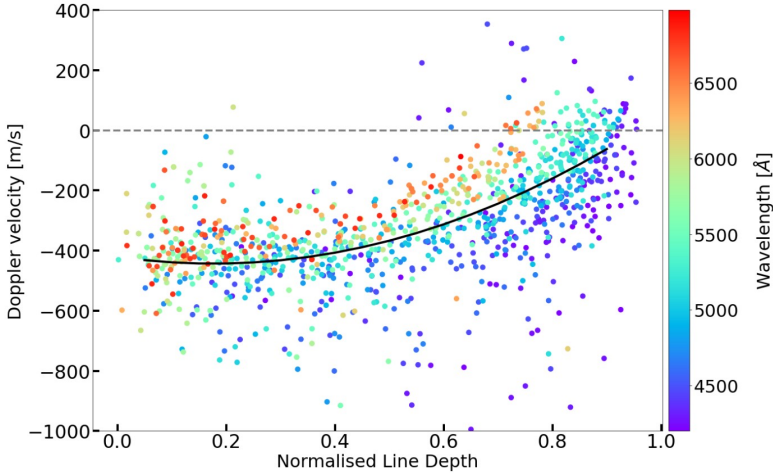


Figure 2.9: The third signature plot for the IAG spatially resolved quiet Sun atlas, shows a strong trend blueshift in the shallow lines. Image taken from [9].

Notice in Figure 2.9 the wavelength-dependence on convective blueshift, which has been extensively documented for several datasets. The significance of the third signature plot lies in its universality for solar-type stars; their plots closely resemble the Sun's, differing primarily by a scaling factor [5]. Consequently, a detailed analysis contributes to the understanding and radiation of photospheric hydrodynamic models [3, 1]. However, a precise measurement of this pattern requires a understanding of the convective blueshift phenomenon.

#### 2.4.5 Convective Blueshift

The measured negative redshift resulting from convective motions is known as *convective blueshifts*, which is measured using the Doppler effect (see Equation (2.14)).

$$v_r \approx c \left( \frac{\lambda_{obs} - \lambda_{em}}{\lambda_{em}} \right) - 633 \text{ m/s} \quad (2.14)$$

Where the value of 633 m/s is the correction of gravitational redshift for the Sun; and the  $\lambda_{em}$  represents the emitted wavelength.

When the Sun pushes material up through its outer layer, the spectrum exhibits a blueshift. As this material subsequently cools and falls back through the atmosphere, it produces a redshift, but emits less light, making the blueshift dominant. Since the strength of the convective distortions

and shifts of spectral lines vary across the H-R diagram, we expect systematic errors in radial velocities [1].

## 2.4.6 Chromodependence characterization

Recent emphasis on measuring the third signature plot has led to new interpretations of line depth-dependent wavelength shifts.

Gray and others authors have qualitatively explained the line-depth dependence of convective blueshift. Shallow lines come preferably from deep photospheric layers where convection is strong, so the convective blueshift is great. Whereas deep lines come preferably from superficial layers, where gravity and the demise of buoyancy has slowed the convection and the blueshift is small. However, an explanation of why this diagonal trend depends on color, or chromodependence of the line depth, has not been found.

In 2018, Gray and Oostra established a standard curve determined by a third order polynomial fit to the solar granulation pattern (see Figure 2.10).

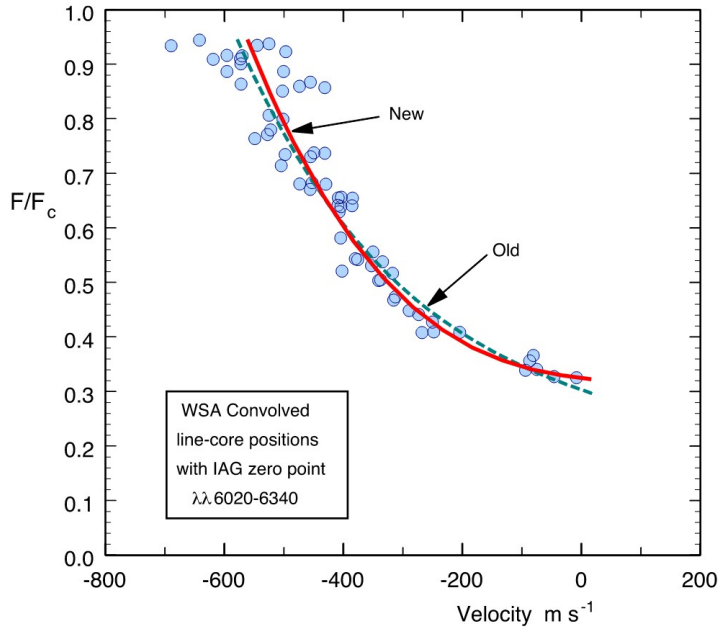


Figure 2.10: Standard curve proposed by Gray and Oostra on the spectral range of 6020 Å to 6340 Å. Image taken from [16].

Nevertheless, the authors limited the spectral range of 6020 Å to 6340 Å, avoiding the chromodependence which becomes evident in a wider spectral range. This limitation motivates the present work to develop a characterization taking into account all wavelength ranges; and give the methodology for dealing with this phenomenon.

A separate theoretical perspective, offered by Hamilton and Lester, attributes aspects of photospheric dynamics to rotation. The pronounced differential rotation with latitude observed seems to be the result of convective flows driven radially by the buoyancy force and deflected horizontally by the Coriolis force [4].

## 2.5 Anomalous chromodependence

In previous research many authors pointed out the phenomenon that we call chromodependence or wavelength dependence of the signatures, emphasizing on the third granulation plot. Because this definition can be ambiguous a clarification is presented below.

In the photosphere model the temperature is higher in the deepest layers than the surface. For the formation of an absorption line, the temperature provides the atom with the energy necessary to be prepared in the lowest energy level. This is defined as the excitation potential ( $\chi$ ). While lines with higher values of ( $\chi$ ) are formed in the deepest layers, lines with smaller values of ( $\chi$ ) are formed near the surface.

However, we recall the fact mentioned about the opaqueness of the photosphere, the lines formed on the surface are stronger than those produced in deeper layers. This results in absorption lines in the violet range, produced when the atom absorbs a high value of energy, formed near the surface implying a lower excitation potential and a small temperature. This is a chromodependence, but is not unexpected in the granulation patterns.

In this scheme, atomic and photospheric structure combine to make blue lines stronger and red lines weaker. This might be called *Normal chromodependence* and should be characterized by a unique granulation curve, because weaker lines experience also a stronger convection. What this project tried to characterize is the anomalous chromodependence, the observational fact of granulation patterns showing a different granulation curve for every wavelength range.

## 3. Methodology

### The blend-free list of Fe I lines

Given the complexity introduced by convective motions on the spectrum, this project takes a computational approach. The analysis was conducted using the Python programming language. All data and code have been uploaded in a [GitHub repository](#), allowing anyone interested to reproduce and verify the authenticity of the results presented.

This project follows the methodology established in previous studies (see [3] and references therein), utilizing a selected list of Fe I lines from Nave [7]. As previously discussed, these lines are ideal for the calibration process due to their high abundance, minimal thermal broadening, limited isotopic variation and availability of accurate laboratory measurements of natural wavelengths.

#### 3.1 Computational approach

The computational approach focuses on identifying the solar granulation patterns by calculating relative velocities from Fe I lines.

First, Fe I lines in the IAG solar flux atlas and the IAG spatially resolved quiet Sun atlas using the Nave blend-free list of Fe I lines were identified [7]. For each identified line were selected bins of  $0.1 \text{ \AA}$  around the closest minimal point to the rest wavelength from the Nave Fe I list. Beware, these points are not the observed wavelengths, just a reference to generate an observation window. Then, a fourth-order polynomial fit was adjusted to the wavelength window; a second-order fit is

clearly insufficient because profiles are known to be asymmetric and a third order fit is still inadequate. We follow Allende and Prieto [19] approach for quantifying asymmetry via the bisector slope using a fourth-order polynomial fit, and the minimum of this polynomial as the observed wavelength. For an optimal fit a z-score standardization was applied to each line core, which is explained in appendix A.

The observed wavelength from the polynomial fit was used to calculate the relative velocity. Finally, the second derivative of the polynomial for the line core curvature (see Equation (2.10)) and the third derivative for the line core bisector slope (see Equation (2.13)) were found.

To maintain consistency when comparing results with other authors, the visible and near infrared range given by Reiners et al. was modified. The visible range is now considered from 4000 Å to 7500 Å; and the near infrared from 7500 Å to 23 000 Å.

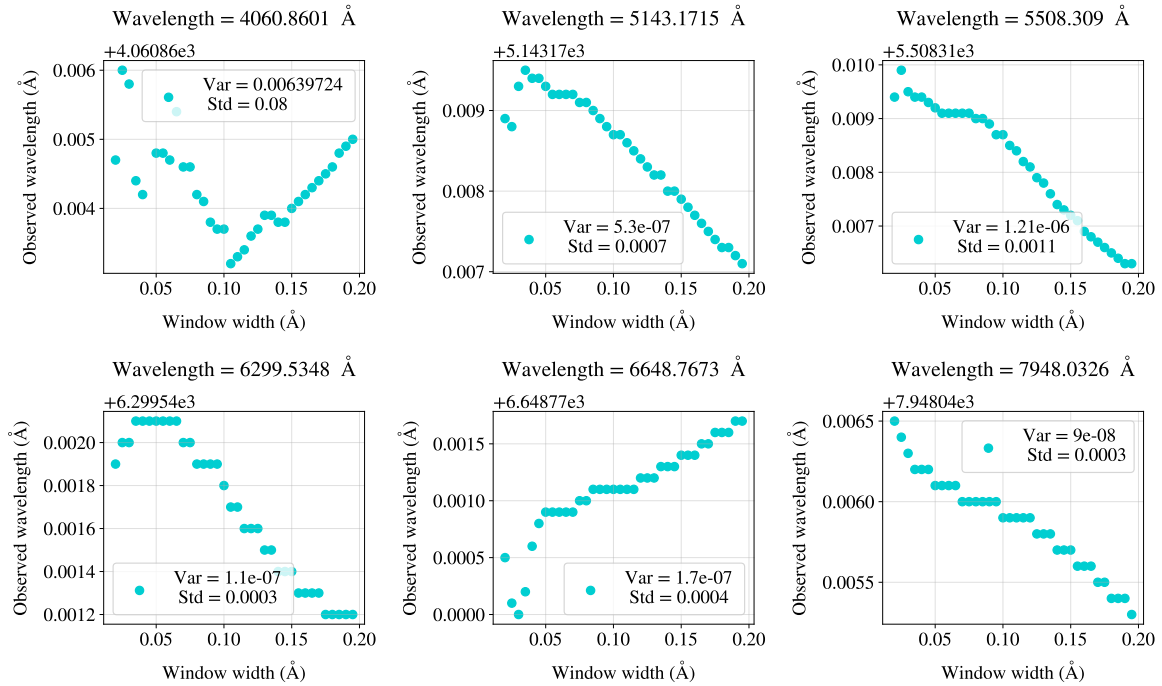
### 3.1.1 Statistical analysis

The selection for the width of the window around the line core for analysis was not statistically justified in previous research. This project presents several results for the statistical methodology accuracy.

The variations of the observed wavelength was analyzed by altering the width of the window used for the fourth-order polynomial fit around the line core. Figure 3.1 shows that a window of 0.1 Å performs well in the visible spectrum. However, its performance degrades in the infrared, where the number of data points defining the line core is reduced compared to a typical line in the visible range. The values for the variance and the standard deviation in each wavelength give a level of accuracy in the obtained results.

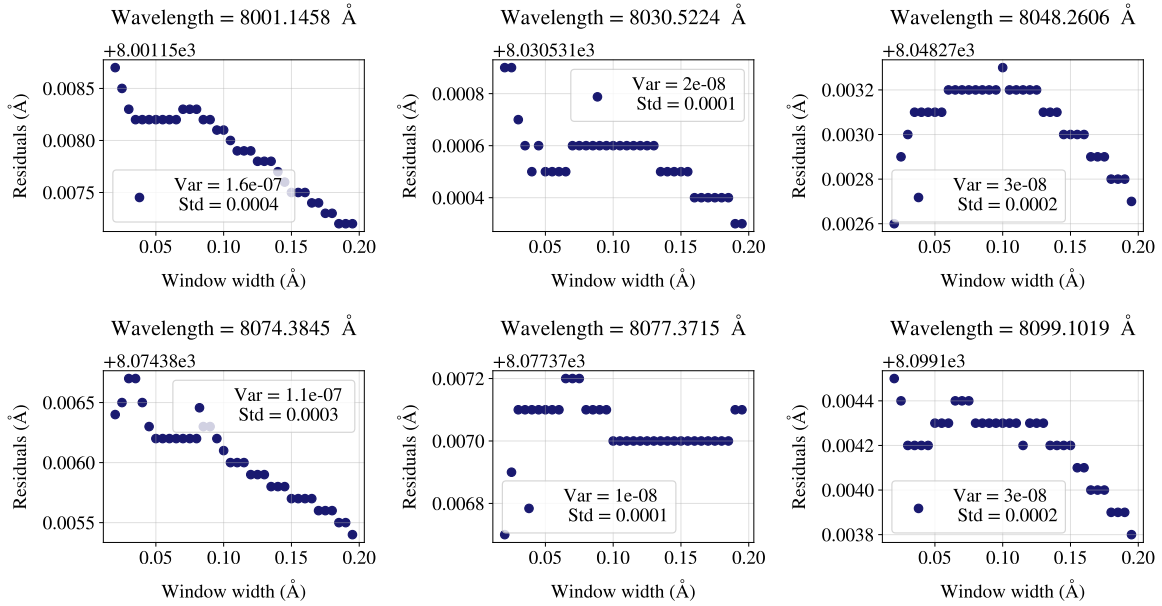
To focus on the line core, limits were established based on a minimum distance from the core of and half of the bisector calculation window width. Specifically, the lower limit was defined as the observed wavelength  $\pm 10$  mÅ; and the upper limit, as the observed wavelength  $\pm 0.1$  Å. To discard velocity values inconsistent with the Sun's physical characteristics, a range of  $-700$  m/s to  $700$  m/s range was applied.

Variance and standard deviation for observed wavelength in the visible range - IAG solar flux atlas



(a) Visible range for the IAG solar flux atlas.

Variance and standard deviation for observed wavelength in the near infrared range - IAG solar flux atlas



(b) Near infrared range for the IAG solar flux atlas.

Figure 3.1: Variance and standard deviation for several observed wavelength altering the width of the window on the fourth-order polynomial fit.

Subsequently, a linear fit was adjusted on the plot of observed against emitted wavelength for each window width, and the residuals were plotted to determine the standard deviation (see Figure 3.2 and Figure 3.3). The goal was not find the closest value to the emitted wavelength, as this would neglect the Doppler effect. The methodology for determining this optimal width was to select the value that minimized the variance of the residuals from a linear regression of observed against emitted wavelength. This approach ensures the consistency of the observed wavelength across the entire spectrum.

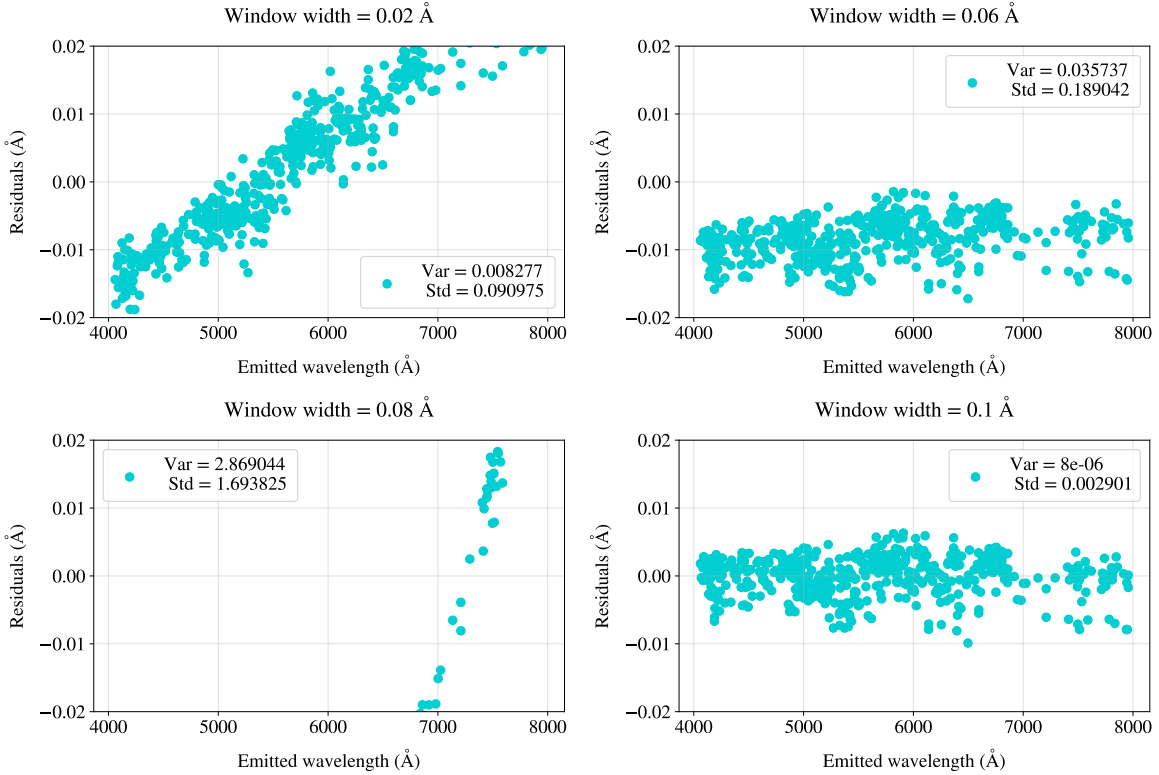
Figure 3.2a shows the residuals of the linear fit across the emitted wavelength for the visible range in the IAG solar flux atlas. With some smaller window widths, a displacement along the wavelength is observed, indicating an inconsistency in the calculated observed wavelength. However, the window width of 0.1 Å shows consistent residuals across the wavelength range and consequently, a minimal variance.

This is confirmed in Figure 3.2b, where the optimal window width is 0.1 Å, ensuring a minimal variance of 0.003.

On the other hand, Figure 3.3a shows the plot of the linear fit residuals across emitted wavelength for the near infrared range in the IAG solar flux atlas. In contrast to the visible range, there is no pronounced displacement along the emitted wavelength, which means there is no strong preference for any specific window width. Figure 3.3b confirms that there are various optimal widths with minimal variance to select. For consistency with the analysis of the visible range, we used the same window width of 0.1 Å. Even though this is not the absolute minimum, it ensures a consistent methodology with low variance of 0.002.

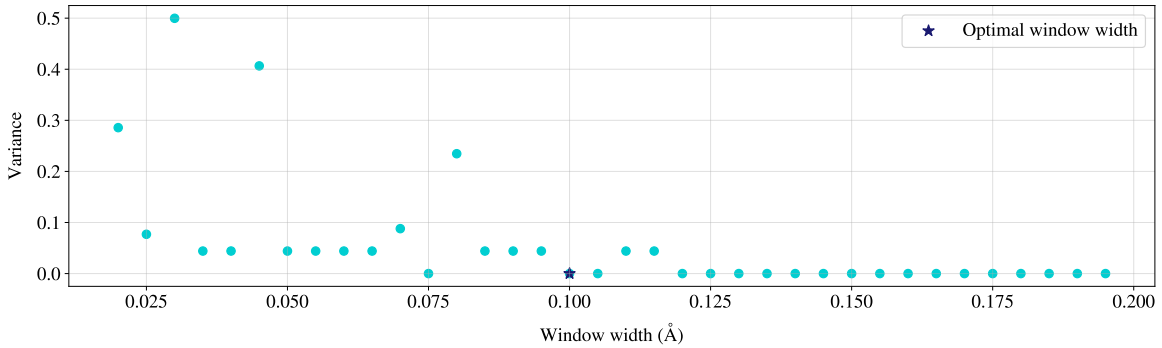
This analysis validates the window width used by Allende and Garcia [19], confirming their hypothesis of 0.1 Å as the optimal window width for the Fe I lines in the solar spectrum. For future work, this process could be formalized into an algorithm that dynamically determines the optimal width based on the specific noise characteristics and spectral features of the dataset.

Observed wavelength across emitted wavelength for each window width in the visible range - IAG solar flux atlas



(a) Plot of the linear fit residuals against emitted wavelength, in smaller widths can be seen a displacement along wavelength.

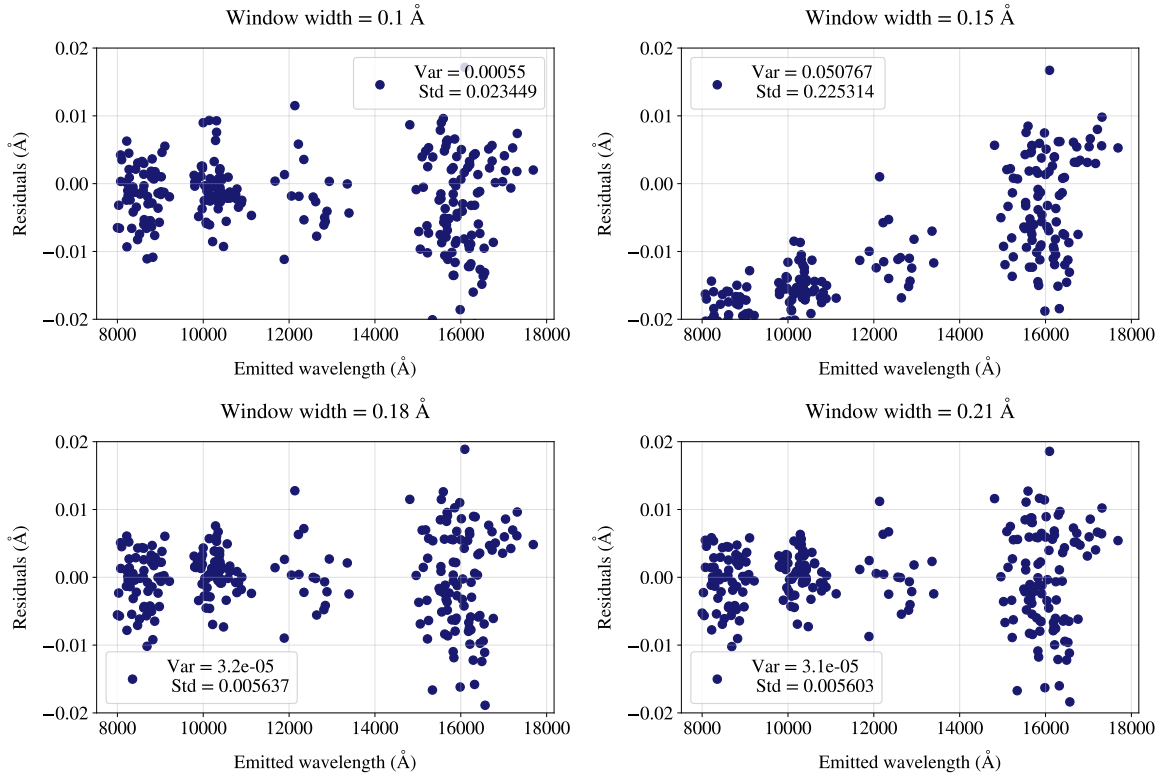
Relation between observed and emitted wavelength for each window width in the visible range - IAG solar flux atlas



(b) Variance of the residuals for each window width, the minimum window width of 0.1 Å ensures consistency along wavelength.

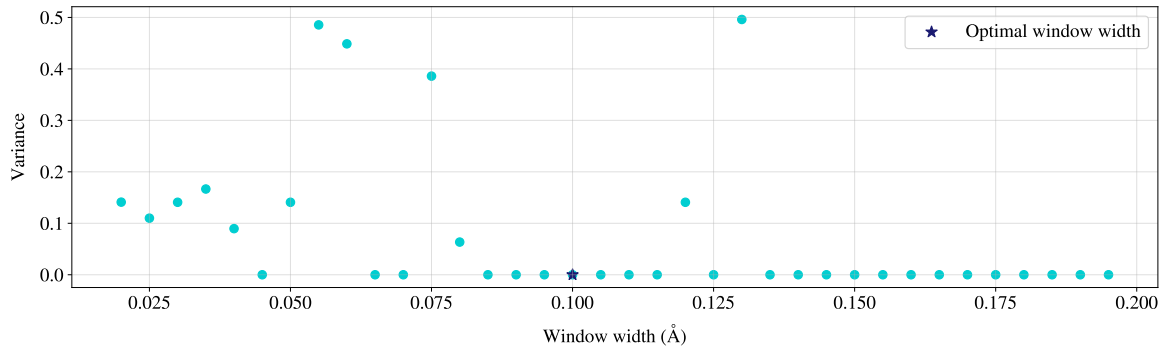
Figure 3.2: Plots of optimal width in the visible range for the IAG solar flux atlas.

Observed wavelength across emitted wavelength for each window width in the near infrared range - IAG solar flux atlas



- (a) Plot of the linear fit residuals against emitted wavelength, there is no pronounced displacement along the emitted wavelength.

Relation between observed and emitted wavelength for each window width in the near infrared range - IAG solar flux atlas



- (b) Variance of each window width, the minimum point that ensures consistency along wavelength is the 0.1 Å even if is not the absolute minimum point.

Figure 3.3: Plots of optimal width in the near infrared range for the IAG solar flux atlas.

## 3.2 Blend-free Fe I line Nave list

The mentioned method implements the Nave list of laboratory-measured Fe I lines [7], which presents laboratory measurements for wavelength and values for excitation potential. This list classifies lines with a quality grading ( $A, B, C, D$ ), based on four wavenumber uncertainties ( $\Delta\sigma$ ) and the corresponding wavelength uncertainties ( $\Delta\lambda$ ). Where  $A$  denotes lines with error in wavenumbers less than  $0.005 \text{ cm}^{-1}$ ; grade  $B$  less than  $0.01 \text{ cm}^{-1}$ ; grade  $C$  less than  $0.02 \text{ cm}^{-1}$ ; and grade  $D$  greater than  $0.02 \text{ cm}^{-1}$ . All known blended lines and all lines measured only in grating spectra have been assigned the grade  $D$  [7].

However, not all the cataloged lines with grade  $A$  are clearly present in the solar spectrum, and in the blue and the near infrared range, many lines are severely blended. In collaboration with Professor Benjamin and Manuel Fuentes, we refined this initial list using different approaches to select the most reliable lines.

### 3.2.1 Selection process for blend-free Fe I lines

The line selection process employed two approaches: Computational and manual. Initially, only quality A lines for the Nave list were selected. This group were subjected to four computational filters based on the properties of having a fourth-order polynomial fit for the line core.

The first filter takes into account the form of the C-curved line profile bisector. Lines whose core bisector profile exhibited excessive scatter, indicating a profile dominated by noise rather than a convective signature, were rejected.

The second filter selected lines whose curvature sign was consistent with an absorption line; this implies the coefficient of the fourth-order term needs to be positive.

The third filter ensures the selected lines represents an absorption curve by discarding closest points that more closely resemble slopes or continuum noise. The condition was keep lines which difference between extreme points of the fit were less than half of the line depth. This describe an absorption curve, and not a slope or noise.

The final filter required a comparision with the obtained third signature plot. Larger discrepancies suggest misidentification or severe blending, rendering the calculated relative velocity unreliable.

This threshold is empirically supported by observations throughout the selection process and the statement for the mean velocity of the sun varies from  $-200$  m/s to  $800$  m/s.

The final part of the selection process was a manual inspection to discard lines that were blended or absent from the solar spectrum. A custom visualizer (detailed in appendix C) was instrumental for this process, allowing the simultaneous display of graphics related to dynamics aspects. This was particularly useful for selecting lines in the near infrared range. The visual requirement focused on the geometry of the spectral line profile, its behavior on the three signatures plots.

The concluding part of the method were performed the plots which represents the three signatures of convection.

First of all, the third signature plot, line core curvatures and line profile bisector slopes against line depth were plotted for all ranges in both atlases in order to observe the three signatures of convection.

## 4. Results and discussion

### The three signatures of convection

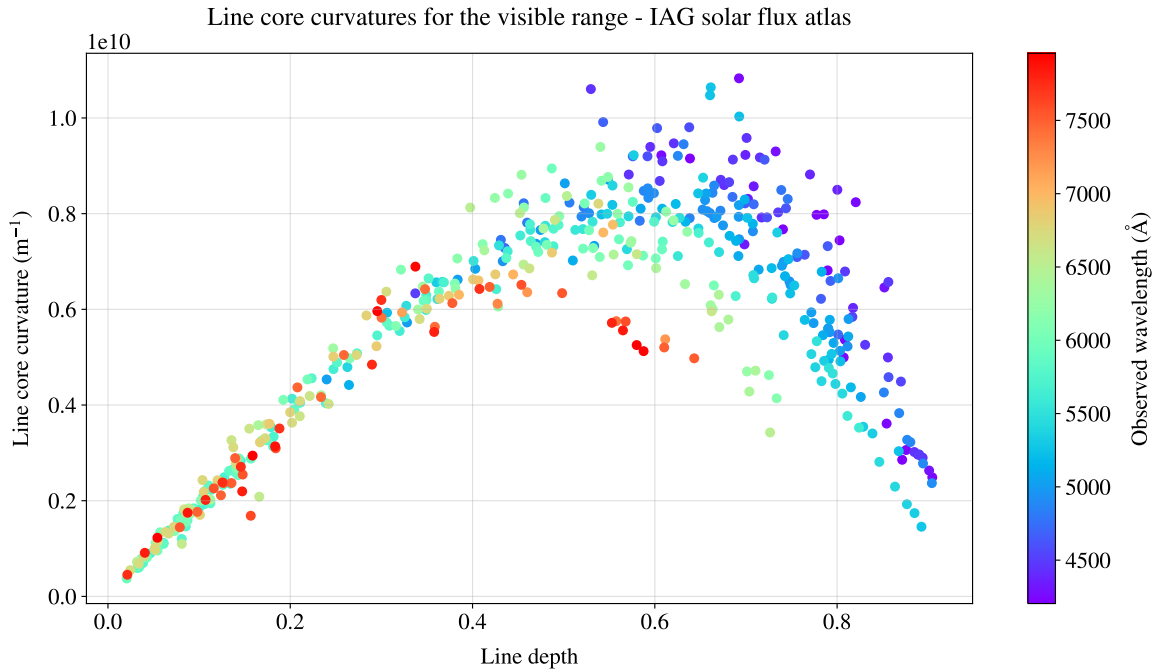
Our results were separated into sections following the signatures of convection. The principal objective for all of was characterize the anomalous chromodependence present on each signature.

#### 4.1 The first signature: Line broadening

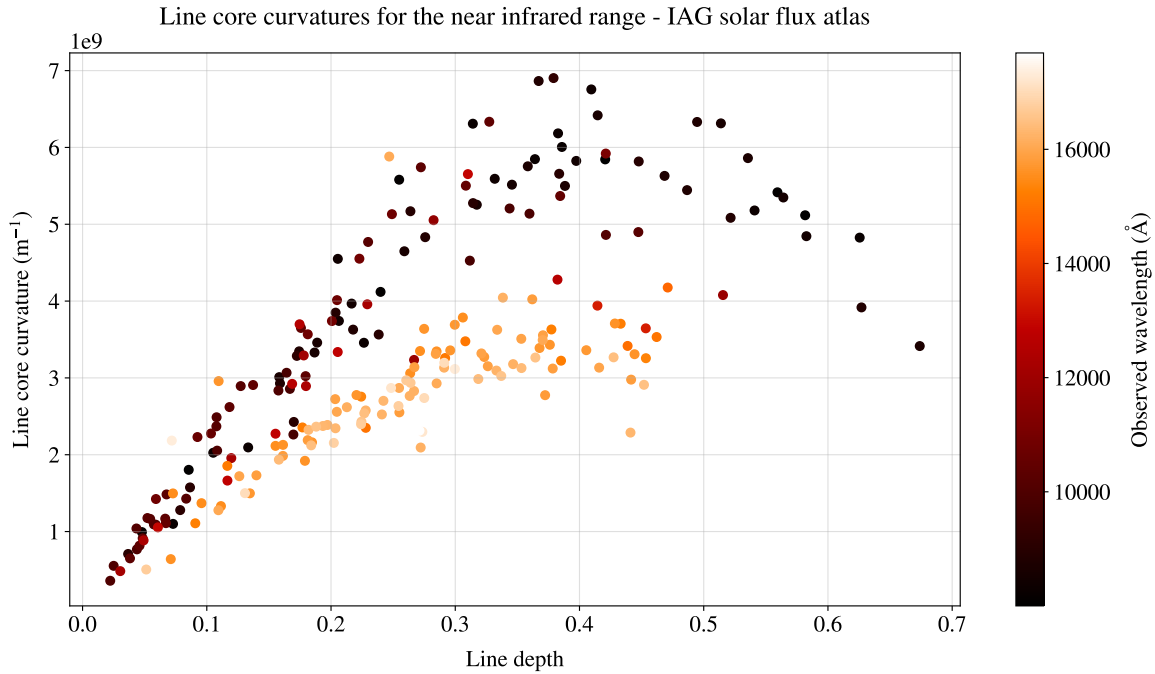
##### 4.1.1 Line depth-dependence of line core curvature

The line core curvatures were calculated following Equation (2.10), and plotted against line depth as shown in Figure 4.1. In general, the behavior described in previous research was observed. For shallow lines, the line core curvature is proportional to depth as expected for all wavelengths, according to Equation (2.12). Furthermore, for deep lines the line core curvature is reduced by saturation with a strong wavelength-dependence.

Figure 4.1a shows that deeper lines deviate from the initial straight line, and here appears a clear anomalous chromodependence.



(a) Line core curvatures for the visible range. While shallow lines curvature is proportional to depth, deep lines curvature is reduced by saturation with is a strong wavelength-dependence.



(b) Line core curvatures for the near infrared range. The plot shows a conspicuous partition around  $14\,000 \text{\AA}$

Figure 4.1: Line core curvatures for the IAG solar flux atlas separated in wavelength ranges.

As shown in Figure 4.1b the near infrared range exhibits a natural division at approximately  $14\,000\text{ \AA}$ , a region dominated by telluric absorption lines from Earth's atmosphere. The division separates the J band, which refers to an atmospheric transmission window of  $3000\text{ \AA}$  centered on  $12\,500\text{ \AA}$ ; and the H band, which refers to an window of  $3500\text{ \AA}$  centered on  $16\,500\text{ \AA}$  [20]. Plotting the entire spectral range of the IAG solar flux atlas, a clear line depth-dependence of the line core curvature as a function of wavelength is observed. Evidently the H-band lines have systematically lower core curvatures than the rest of the sample. This is another instance of anomalous chromodependence.

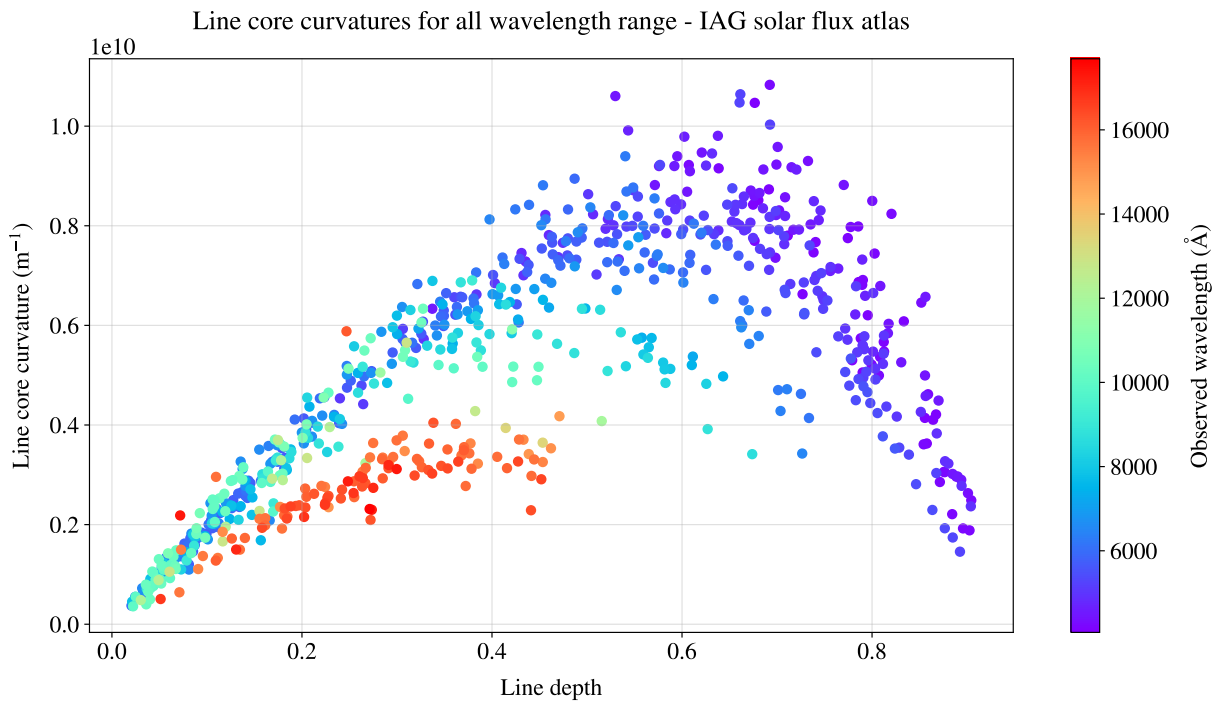


Figure 4.2: Line core curvatures in the IAG solar flux atlas. For shallow lines (depth less than 0.3), while the J band for the near infrared range adjust to the general trend, the H band follows a totally different trend.

For shallow lines (depth less than 0.3), while the J band for the near infrared range adjust to the general trend in Figure 4.2, the H band exhibit substantially smaller curvatures.

Furthermore, the visible range of the IAG solar flux atlas exhibits a clear linear trend for shallow lines (see Figure 4.2). Therefore, the analysis was limited for shallow line depth dependences on

line core curvature in the visible range. Consequently, a linear fit was applied to the visible range for the IAG solar flux atlas in the range  $0.0 - 0.1$  of line depth.

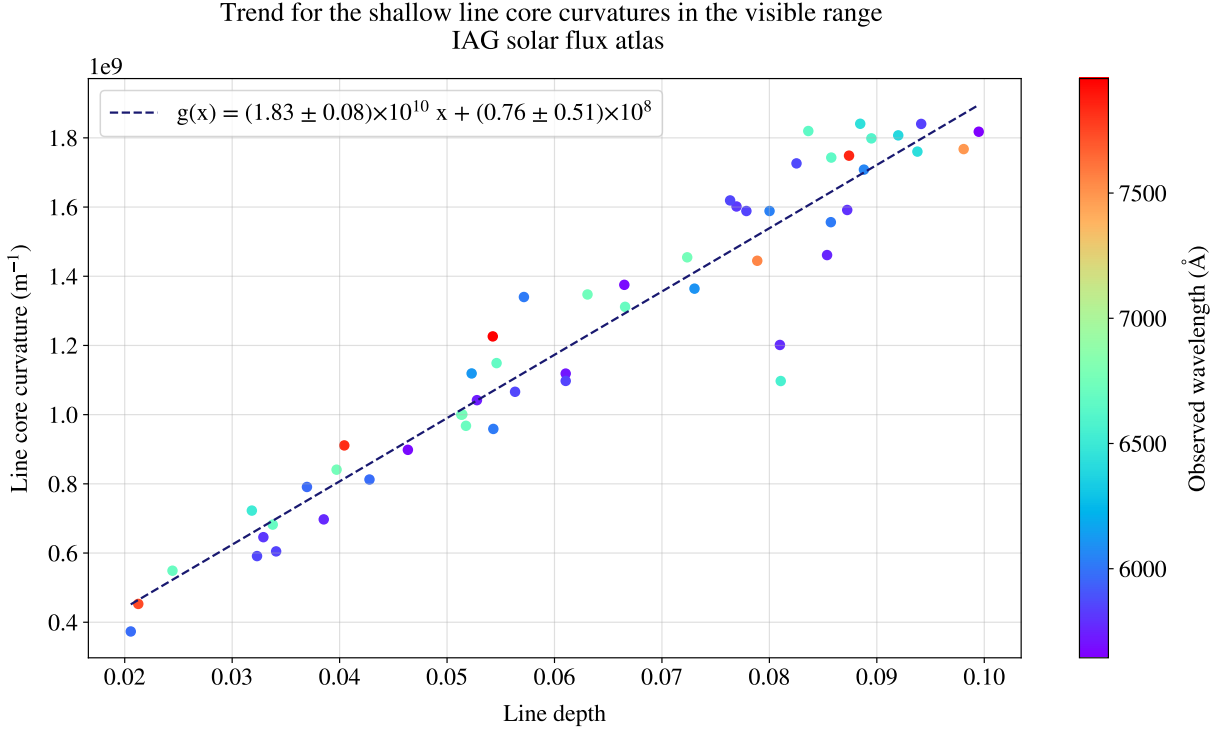


Figure 4.3: Linear fit applied to the range  $(0.0 - 0.1)$  of line depth in the visible range of the IAG solar flux atlas.

As shown in Figure 4.3, the slope of the relationship has a value of  $(1.83 \pm 0.08) \times 10^{10} \text{ m}^{-1}$ . The absence of wavelength-dependence in this spectral range indicates that line core curvatures have a net dependence on velocities (thermal, convective and rotational), with negligible influence from atomic effects. To confirm this statement, the line core curvature was also plotted for the visible range using the IAG spatially resolved quiet sun atlas at the solar disk center,  $\mu = 1$  as shown Figure 4.4. In other words, this analysis uses light from the center of the solar disk, which is not affected by rotational Doppler broadening, thereby isolating the local effects.

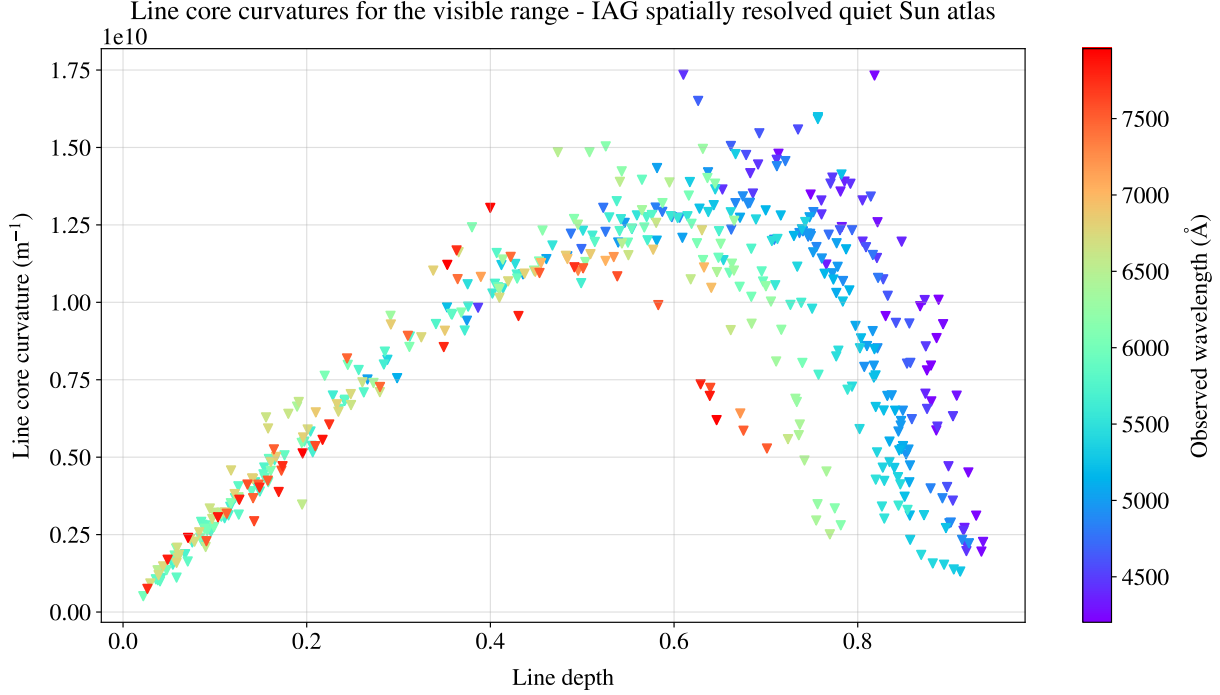


Figure 4.4: Line core curvatures for the visible range of the disk center data from the IAG spatially resolved quiet Sun atlas.

A linear fit was applied taking the same range  $0.0 - 0.1$  of line depth, the Figure 4.5 shows a value of  $(2.94 \pm 0.16) \times 10^{10} \text{ m}^{-1}$  for the slope.

The result of finding a greater slope in the center-disk confirms that rotation is an important cause for line broadening. In the IAG spatially resolved quiet Sun atlas the curvatures are greater, meaning that the broadening is smaller. This allows deduce the variance of convection speed, knowing the thermal velocity.

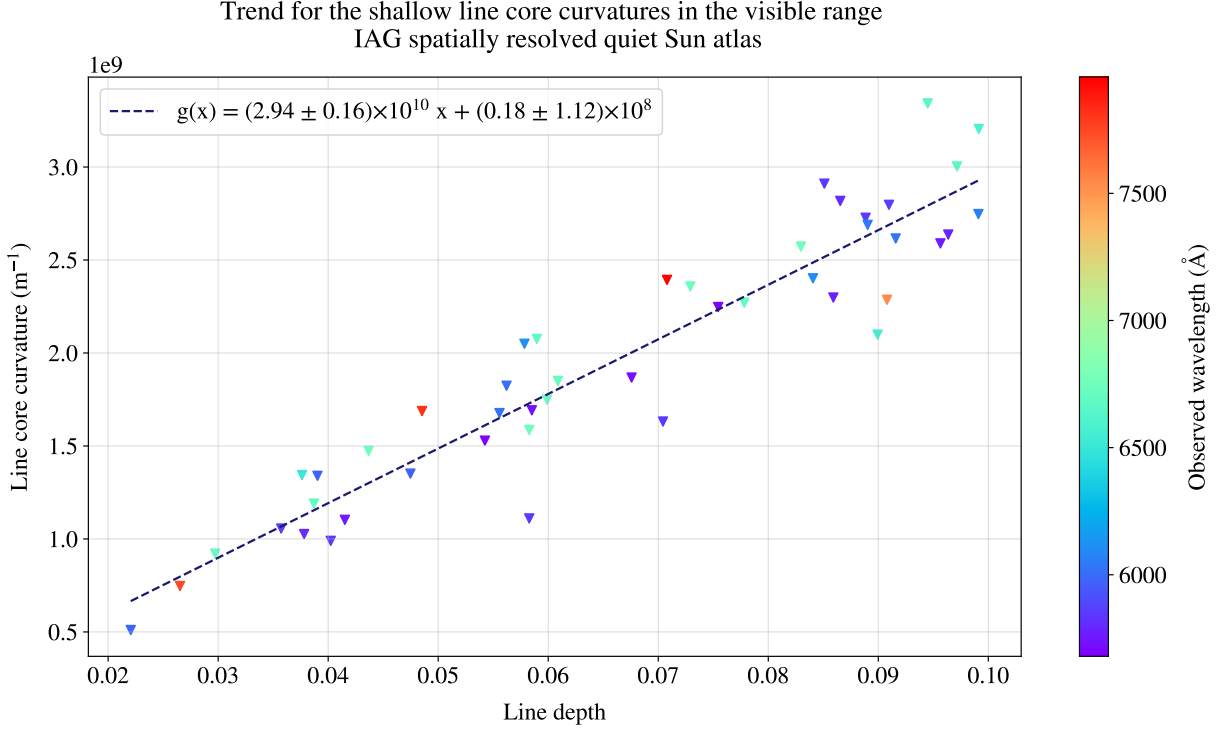


Figure 4.5: Linear fit applied to the range (0.0 – 0.1) of line depth in the visible range of the IAG spatially resolved quiet Sun atlas.

As mention before, we can induce from here the  $\langle v_{\text{conv}}^2 \rangle$  as we the other parameters described in Equation (2.12) and confirm that rotation is an important cause. Using the theoretical values reported and the value from the linear fit applied on shallow lines for both atlases, we found values for  $\langle v_{\text{conv}}^2 \rangle$  of 3.15 (km/s)<sup>2</sup> for the disk-integrated flux spectrum and 2.20 (km/s)<sup>2</sup> for the disk-center spectrum. This is not according to the theoretical behavior, cause in the center-disk spectrum the rotation is negligible and the convection can be seen in his totality.

This behavior can be attributed to saturation in the deepest lines or the growing influence of other atomic broadening effects. For example, damping coefficients which are related to the Fe I atoms and intrinsically wavelength-dependent due to atomic structure, become a relevant factor to investigate.

## 4.2 The second signature: Line profile asymmetry

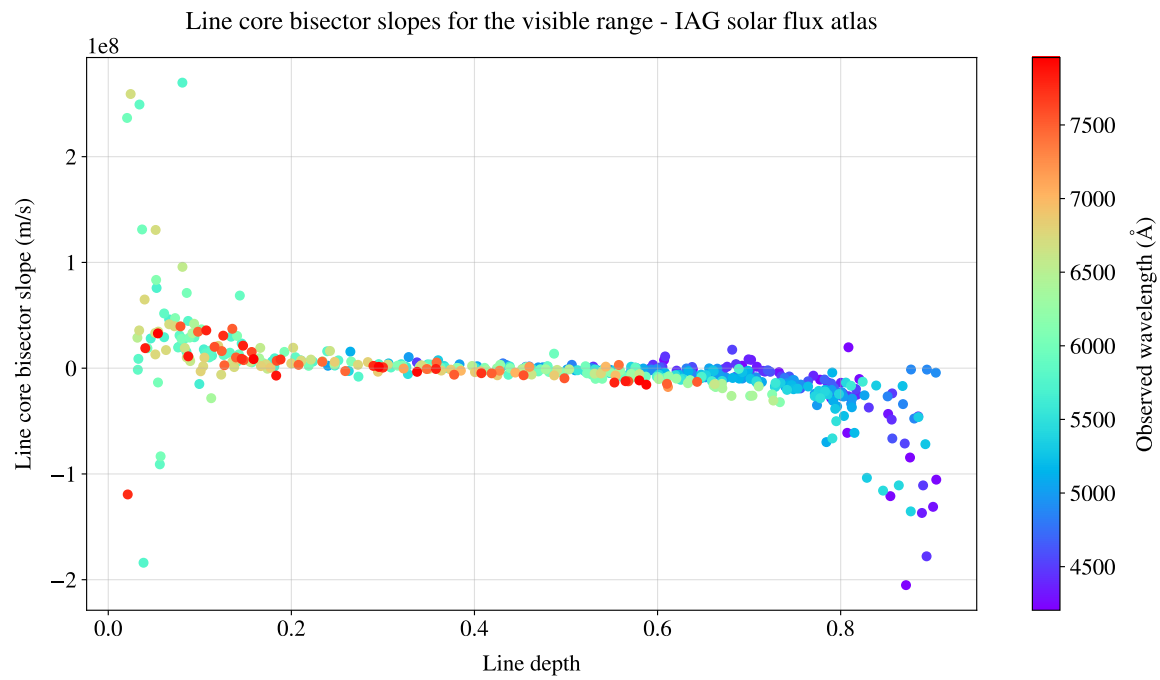
### 4.2.1 The line core bisector slope

As mention before, convection is the only mechanism that creates asymmetric line profiles. Consequently, the slope of the line core is an indirect line profile asymmetry measure, expressed as a velocity.

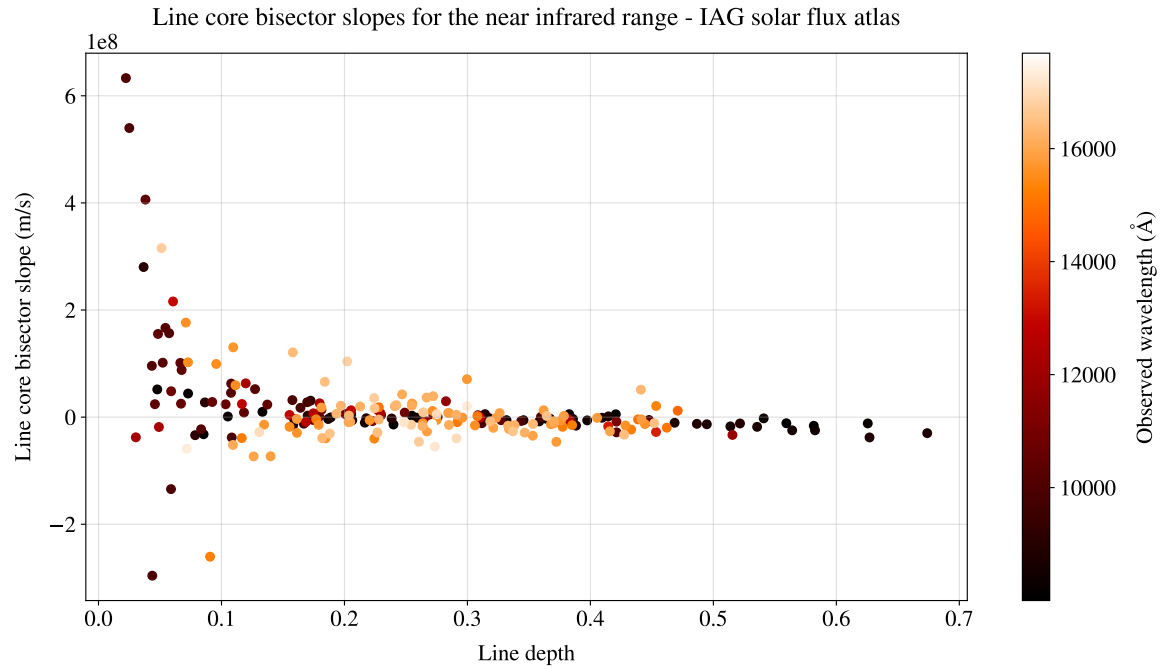
The line core bisector slope was calculated following the equation (2.13) and plotted against line depth, as shown Figure 4.6.

The shallow lines, due to their small depth, do not exhibit a fully developed C-shaped bisector. Instead, their bisectors shows as a positive slope. In contrast, deep lines experiences the convective blueshift in its totality, exhibit a negative bisector slope. Finally, the line depths in the middle range represent lines profiles which are not greatly affected by convection.

With the goal of describing the middle range values for line depth which shows a non pronounced convection effect, we conducted a separate analysis on this subset. Then, a linear fit was applied to the line core bisector slope data in the line depth range of (0.3 – 0.6) to quantify this transition, as shown in Figure 4.7.

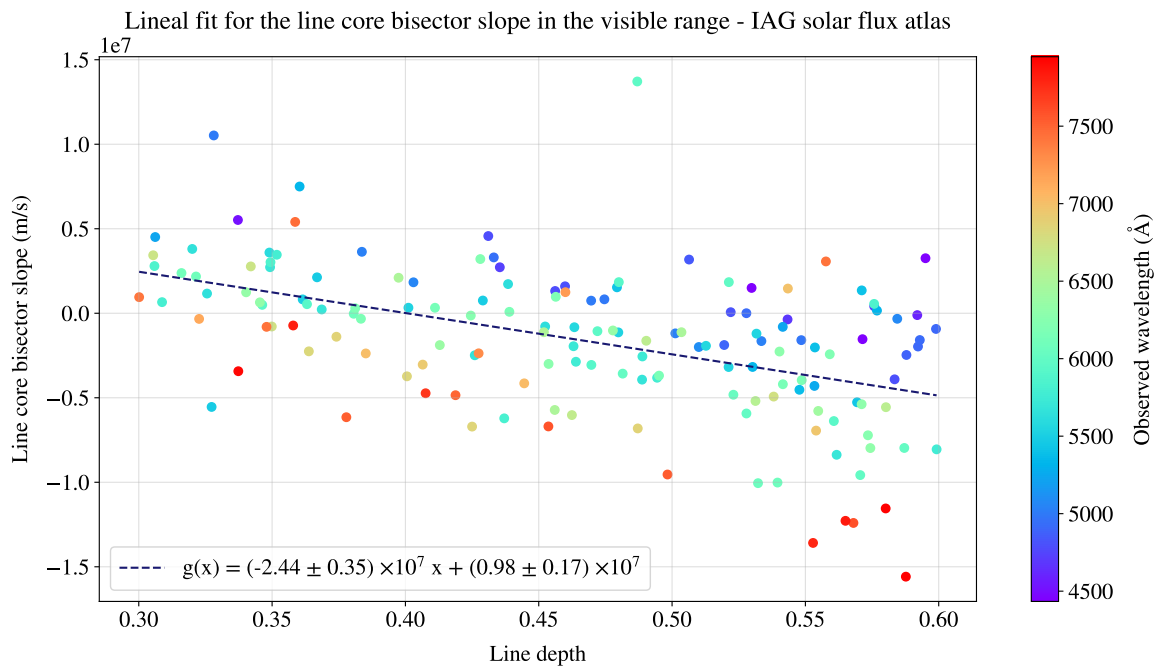


(a) Line core bisector slopes for the visible range.

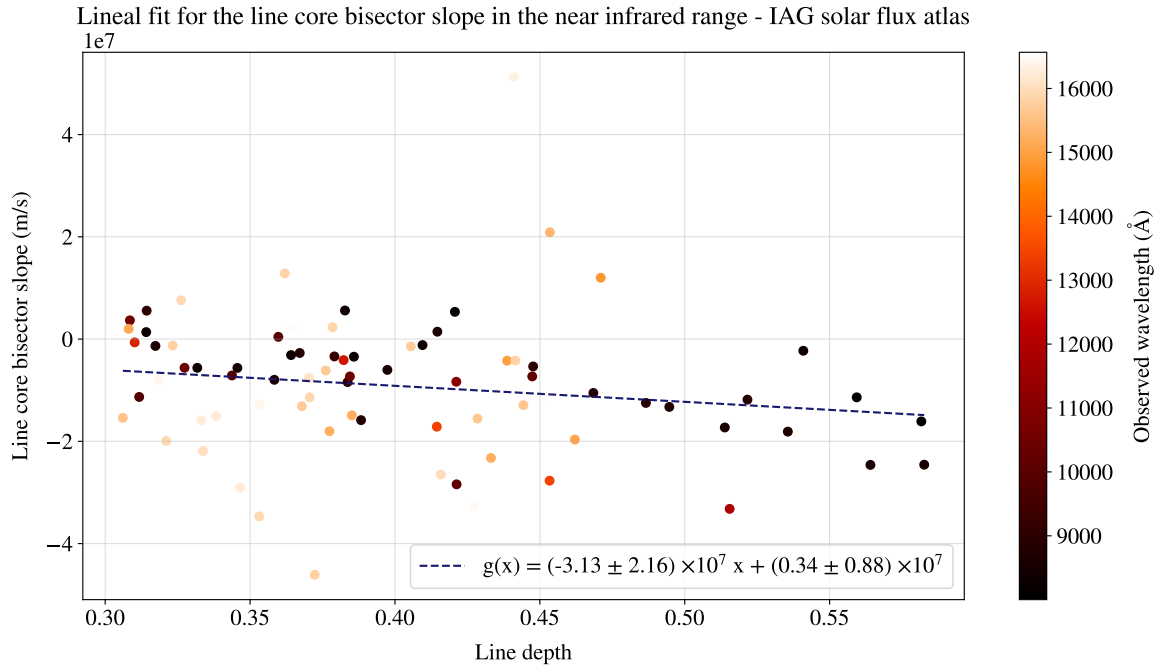


(b) Line core bisector slopes for the near infrared range.

Figure 4.6: Line core bisector slopes for the IAG solar flux atlas separated in wavelength ranges. The behavior of both plots is according to the C-curved shape of the line profile bisector affected by convection movement.



(a) Linear fit adjusted to the visible range.



(b) Linear fit adjusted to the near infrared range.

Figure 4.7: Linear fit adjusted to the range (0.3 – 0.6) of line core bisector slopes in the IAG solar flux atlas, where an anomalous wavelength-dependence becomes evident.

Figure 4.7a, for the visible range, shows an evident wavelength-dependence along the line core bisector slopes. In contrast, Figure 4.7b, for the near infrared range, illustrates a poor wavelength dependence, along with a greater amount of scatter in the dataset. Due to this difference, we focused our analysis of the anomalous chromodependence presented through line asymmetry, only to the visible range. For comparision, the same behavior on the the disk center spectrum was searched (see figure 4.8).

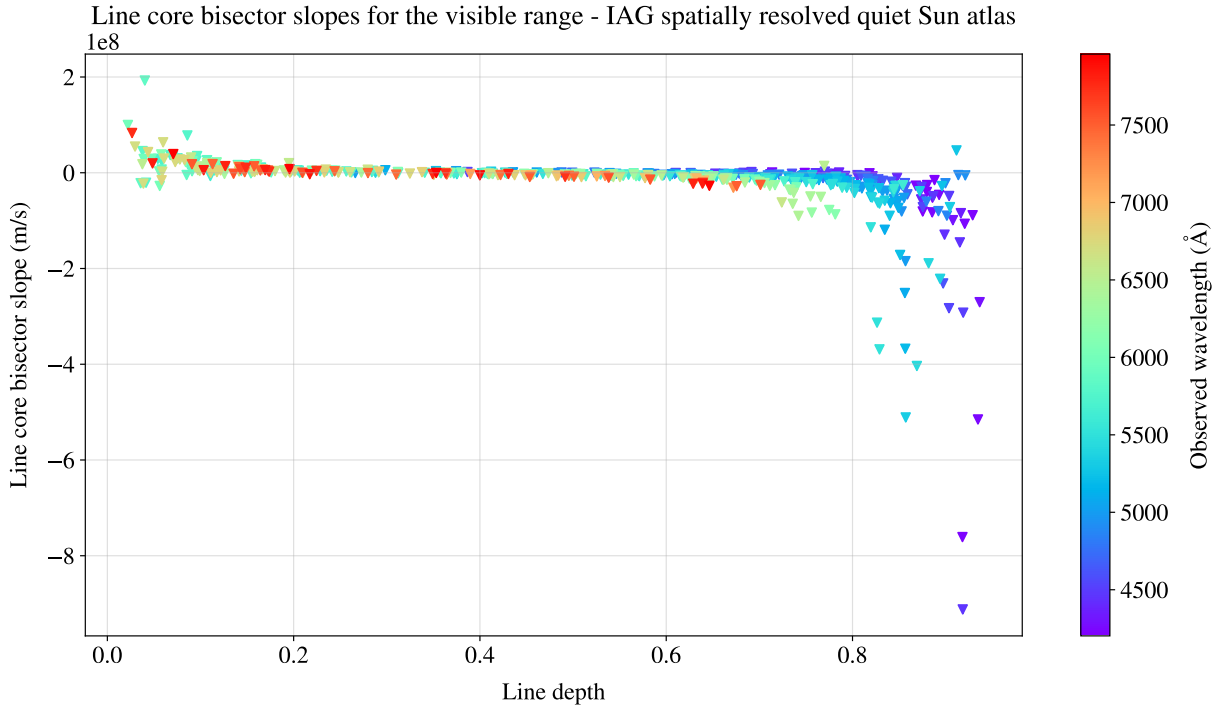


Figure 4.8: Line profile bisector slopes for the visible range in the IAG spatially resolved quiet Sun atlas for  $\mu = 1$ .

Figure 4.9 Shows that the bisector slope derived from the disk center is smaller in magnitude compared to the integrated flux, despite both exhibiting the same characteristic trend. This behavior is clearer on the disk-center spectrum than the disk-integrated flux spectra, where the line profile bisectors slopes are organised by decreasing wavelength. To characterize this wavelength dependence, the line was deparated into bins of 0.1, and the line profile bisector slope was plotted against wavelength. This allowed shifts in the bisector slope to became apparent, as shown in Figure 4.10.

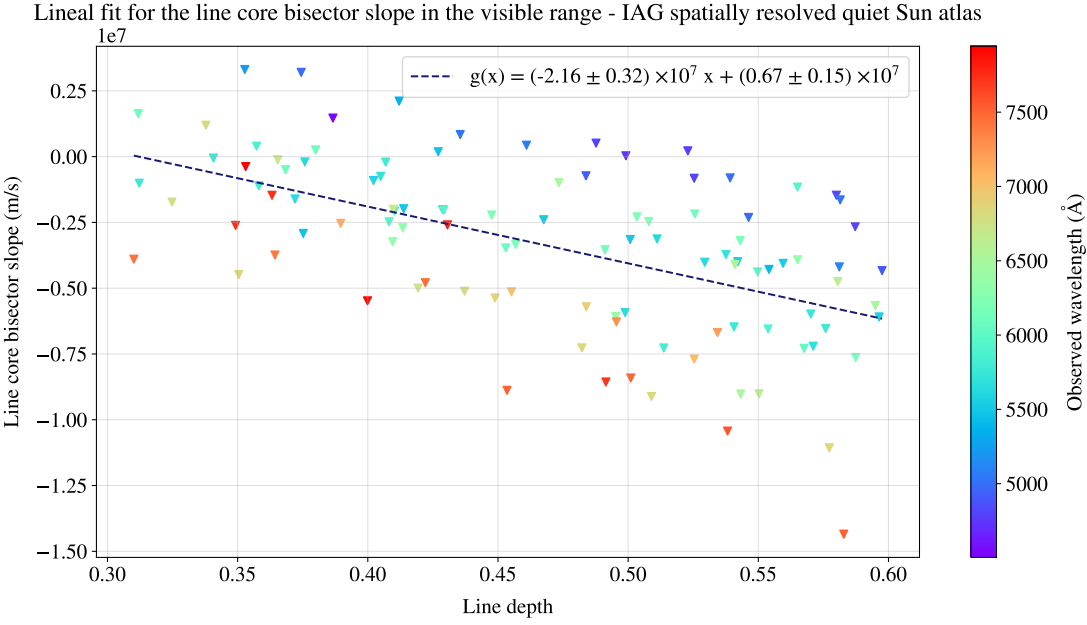


Figure 4.9: Linear fit adjusted to the range (0.3–0.6) of line core bisector slopes in the disk-center spectrum, where also the anomalous wavelength-dependence is evident.

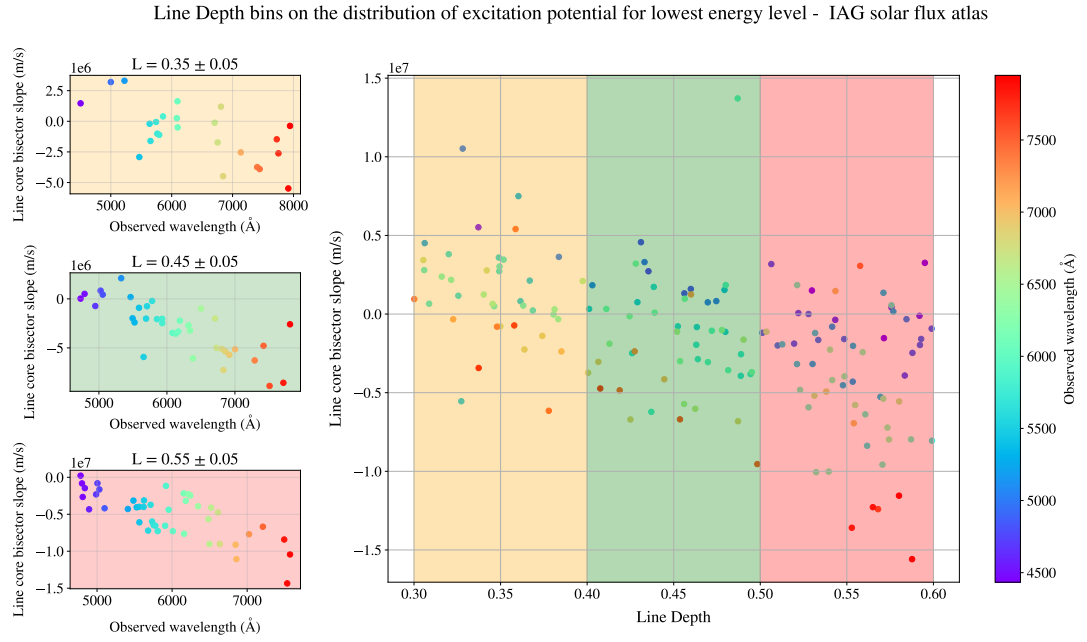


Figure 4.10: Line depth bins of 0.1 for the visible range of the IAG solar flux atlas, where wavelength-dependence of the slopes becomes apparent. The same analysis was performed on the disk-center spectrum.

For each bin in both atlases, a linear fit was applied to characterize the wavelength dependence. For the integrated flux spectrum, was found that for a line depth fixed window, the slopes decrease with wavelength (see Figure 4.11).

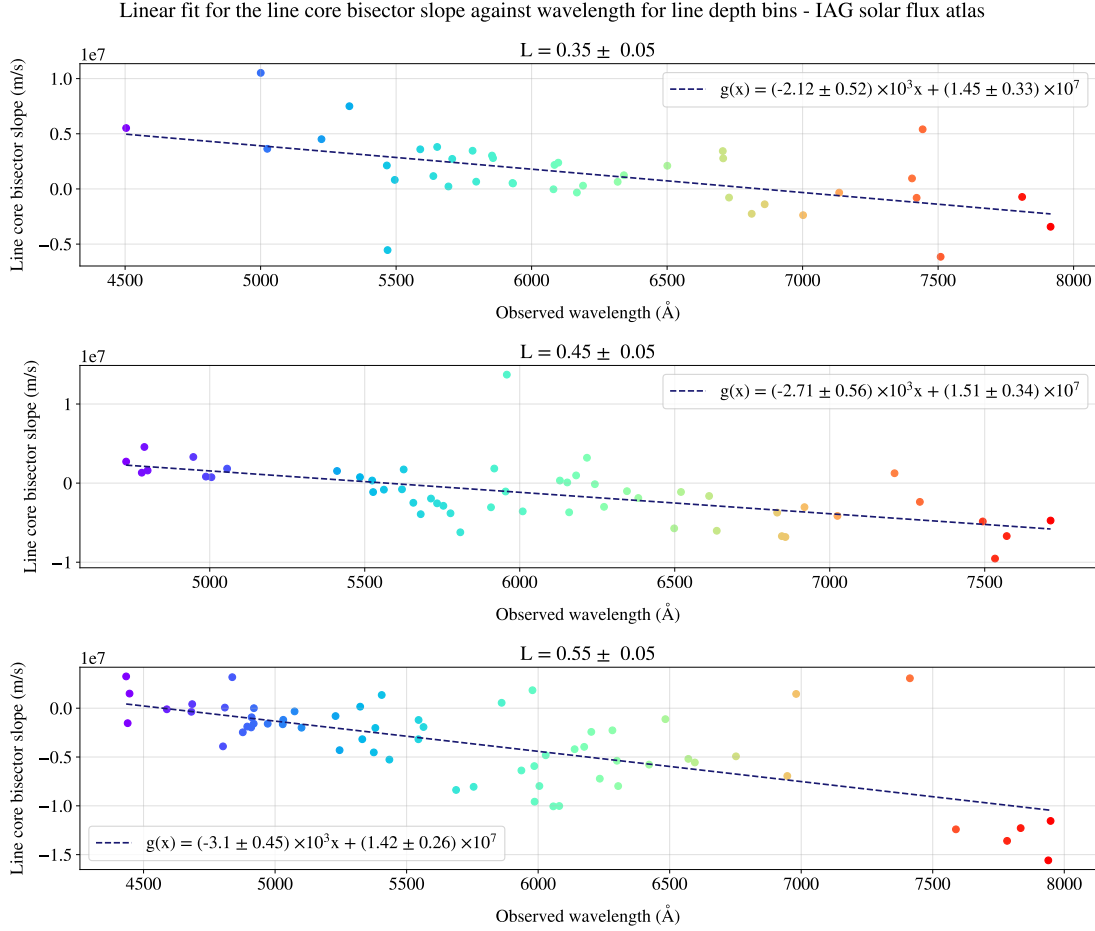


Figure 4.11: Individual plots of line core bisector slope against wavelength representing each bin of line depth for the visible range of the IAG solar flux atlas.

The same analysis was performed on the disk-center flux, revealing the same general behavior (see Figure 4.12). However, a quantitative difference was found: The displacement in the line core bisector slope values is smaller across all line depths in the disk-center data. Despite this overall difference, the values for the middle depth range of  $0.45 \pm 0.05$  are relative closer. This indicates that the same physical behavior predominantly affects the line profiles within this specific range.

Linear fit for the line core bisector slope against wavelength for line depth bins - IAG spatially resolved quiet Sun atlas

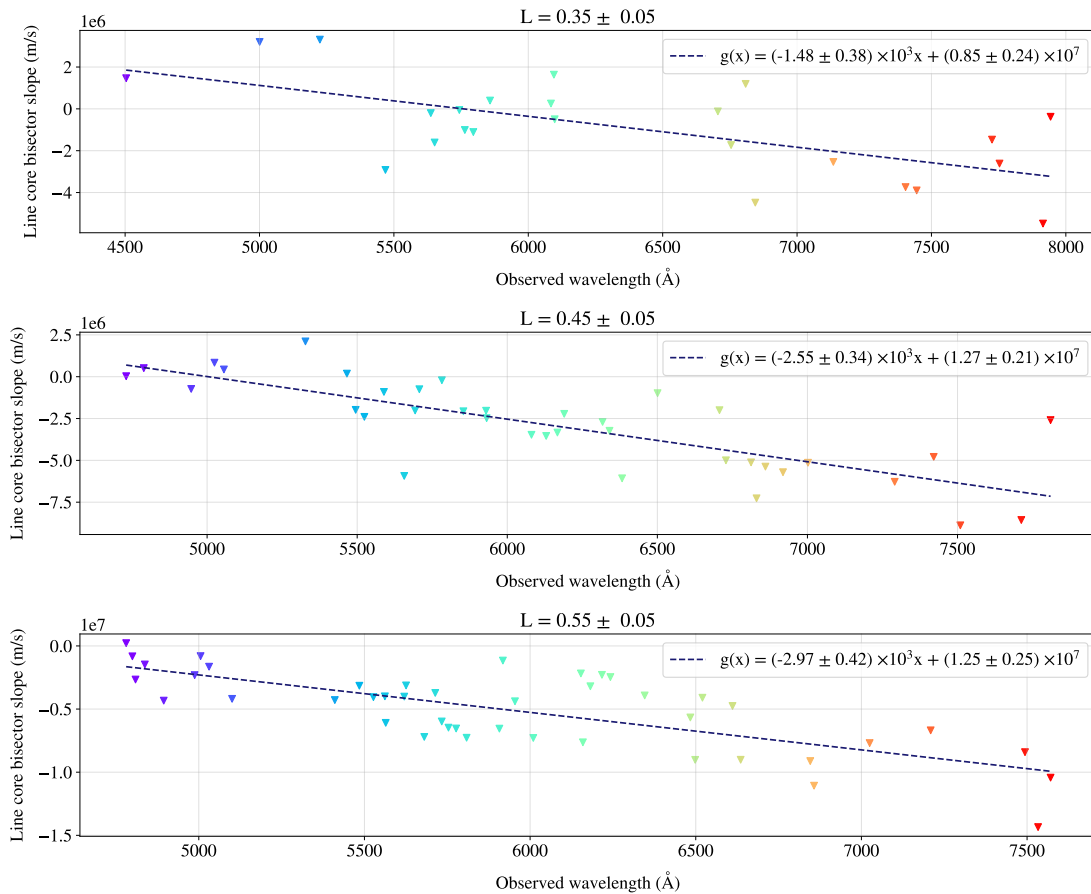


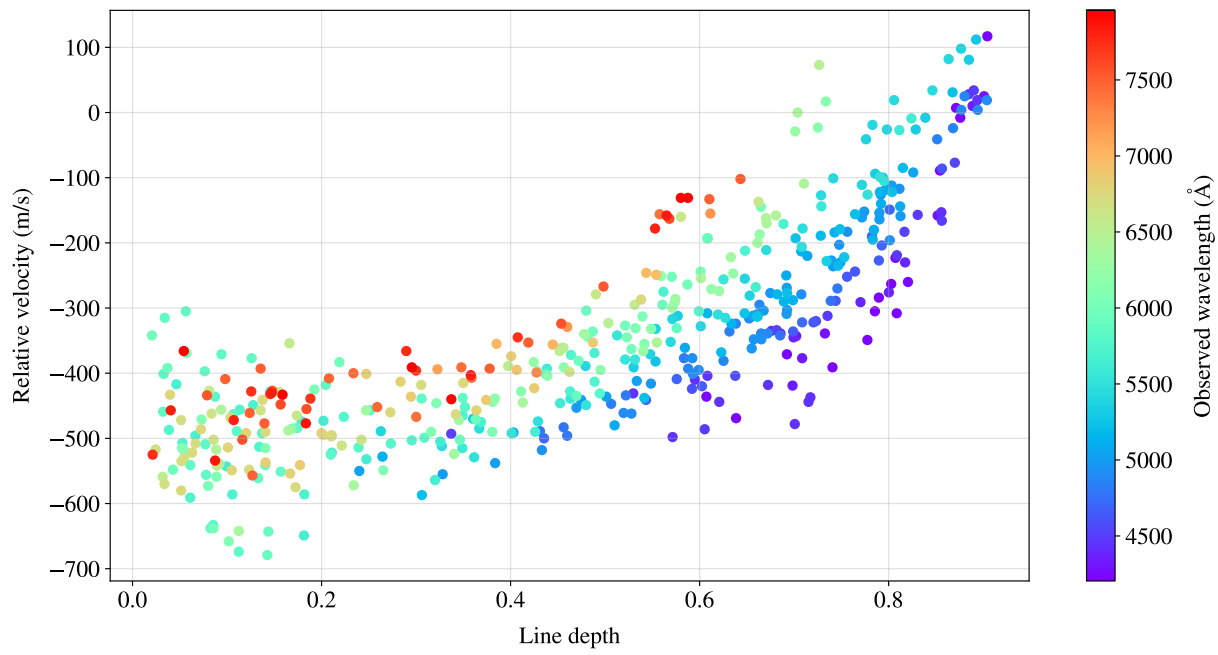
Figure 4.12: Individual plots of line bisector slope against wavelength representing each bin of line depth for the Spatially Resolved Quiet Sun Atlas.

## 4.3 The third signature: Line depth-dependence of wavelength shifts

### 4.3.1 Line depth-dependence of wavelength shifts

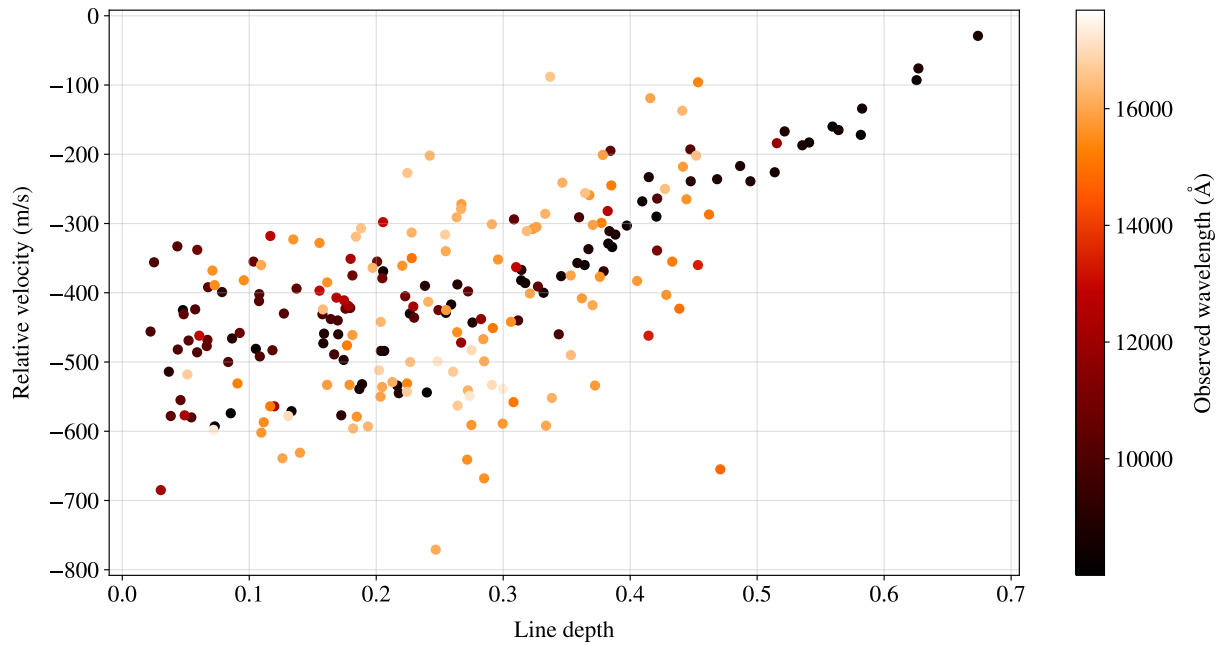
The third signature plot is represented by a graph of relative velocity against line depth for the IAG solar flux atlas.

Third signature plot for the visible range - IAG solar flux atlas



(a) Third signature plot for the visible range.

Third signature plot for the near infrared range - IAG solar flux atlas



(b) Third signature plot for the near infrared range.

Figure 4.13: Third signature plots obtained for both wavelength ranges in the IAG solar flux atlas, in both plots the relative velocity is wavelength-dependent.

As shown in Figure 4.13, the convective velocity depends on line depth, as described in literature. Moreover, the anomalous chromodependence makes its presence known in the fact that this *granulation curve* is not unique or universal, but depends on the wavelength range. To further characterize this trend, we performed an analysis of line depth versus wavelength at fixed velocities.

To measure these wavelength shifts, the analysis was restricted to the spectral range from 4300 Å to 5600 Å. The need for this restricted range is illustrated in one of the panels of Figure 4.14, showing that longer wavelengths exhibits more complex structures which make a linear fit unsuitable. The wavelengths within this range were then sorted into velocity bins of 50 m/s.

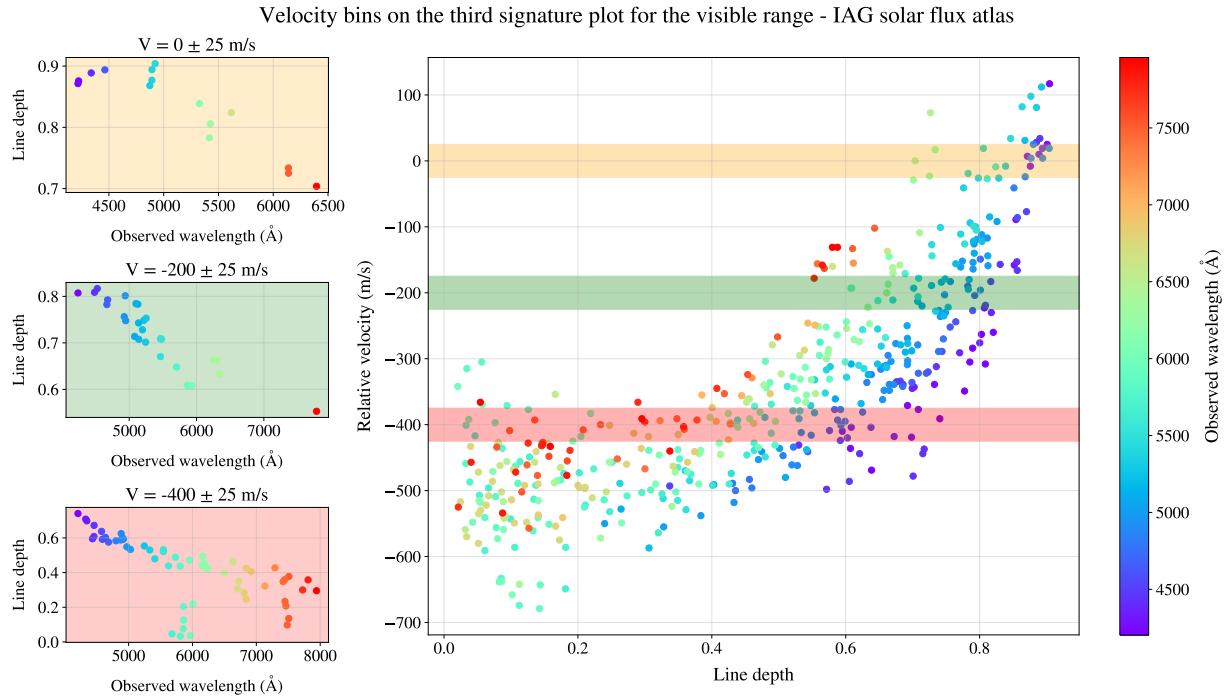


Figure 4.14: Velocity bins for the relation between wavelength and line depth for the visible range in the IAG solar flux atlas.

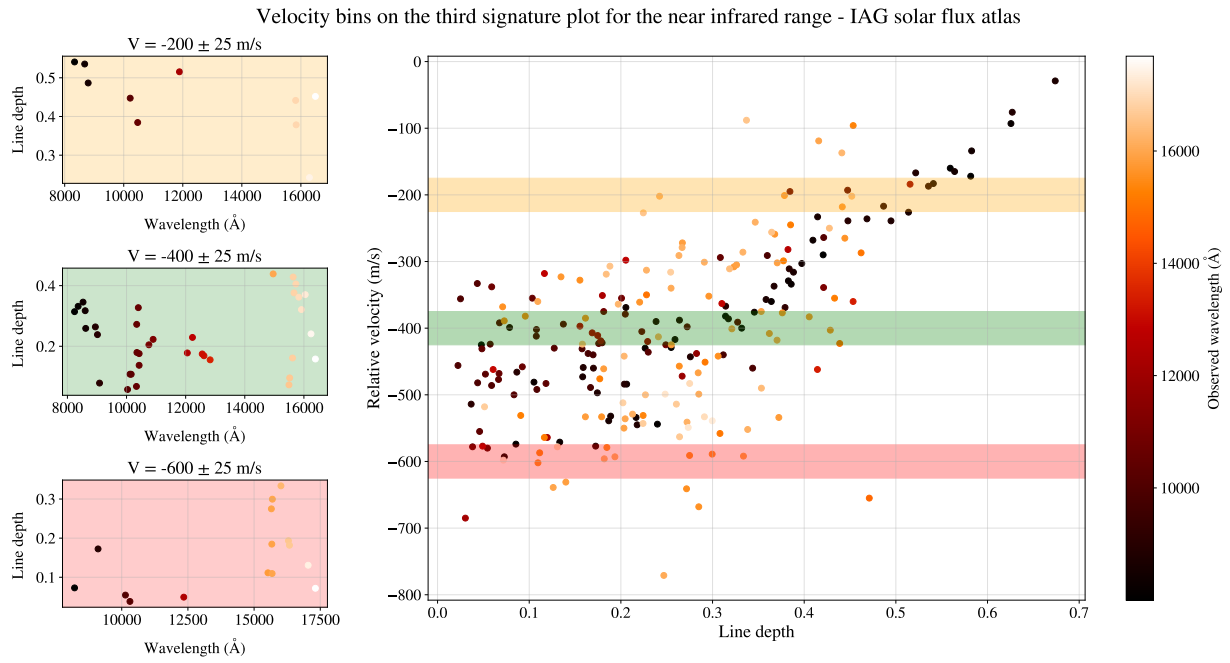
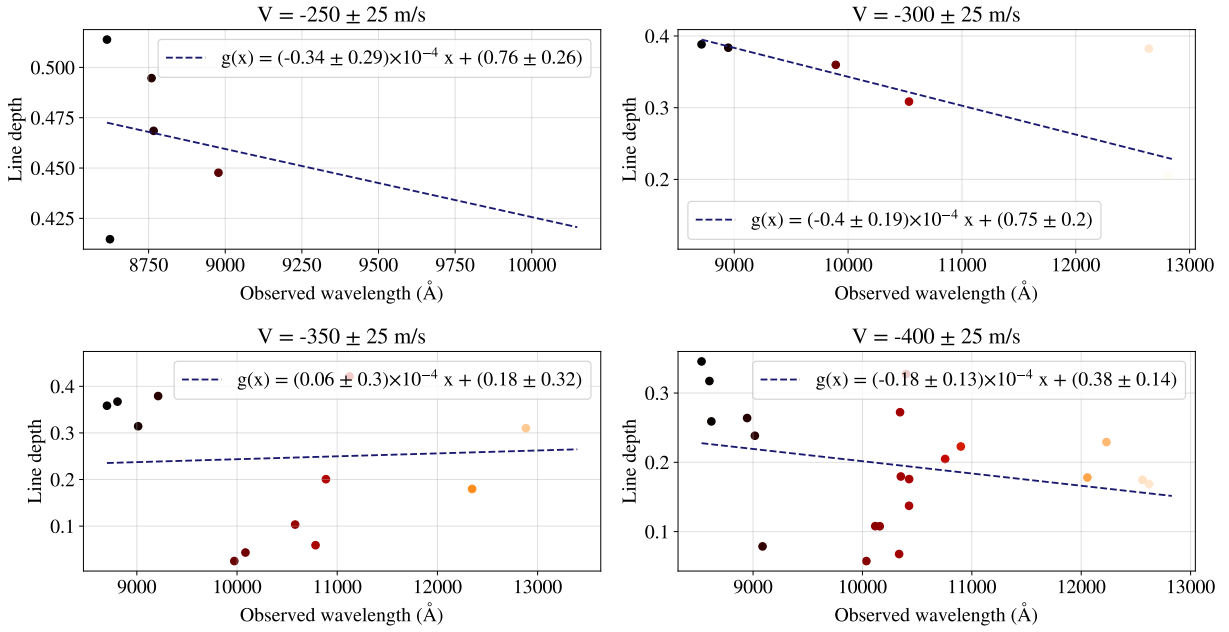


Figure 4.15: Velocity bins for the relation between wavelength and line depth for the near infrared range in the IAG solar flux atlas.

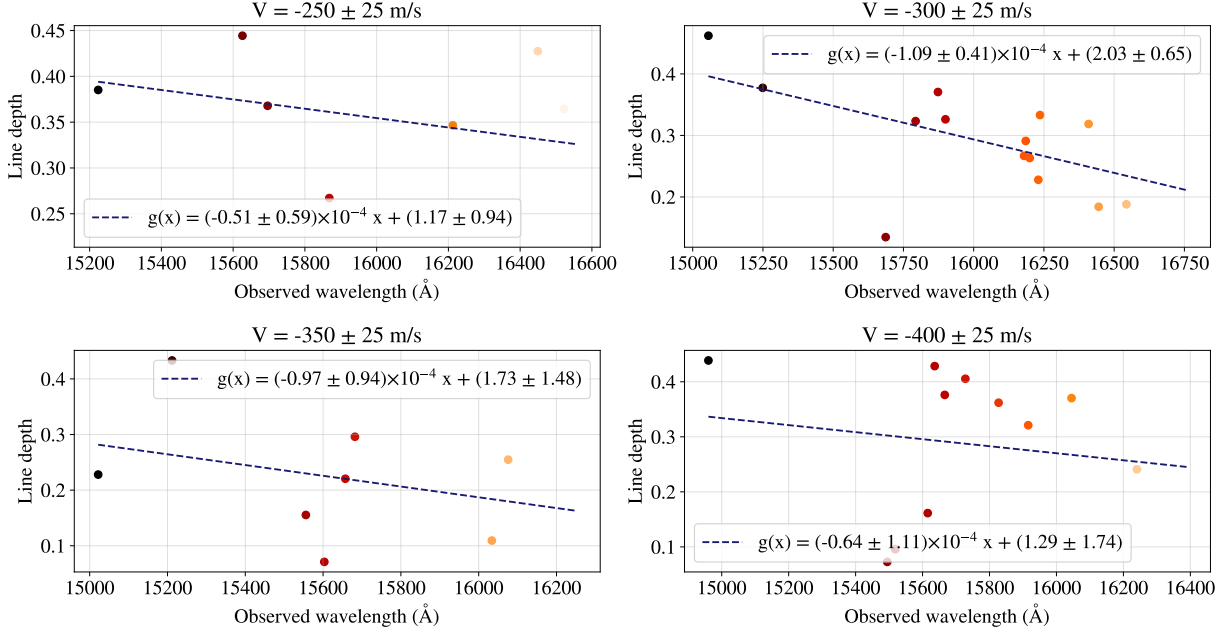
Figure 4.15 illustrates the separation of the near-infrared granulation pattern into its natural bands. To analyze this behavior, the wavelength shifts were treated separately within these bands and then plotted against wavelength to fit a linear regression, as shown in Figure 4.16. The same analysis was performed for each velocity bin in the visible range, showing the results in Figure 4.17.

Linear fit for wavelength-dependence of line depth for velocity bins - J band near infrared



(a) J natural band.

Linear fit for wavelength-dependence of line depth for velocity bins - H band near infrared



(b) H natural band.

Figure 4.16: Individual plots of line depth against wavelength representing each bin of velocity separated in natural bands J and H for the near infrared range of IAG solar flux atlas.

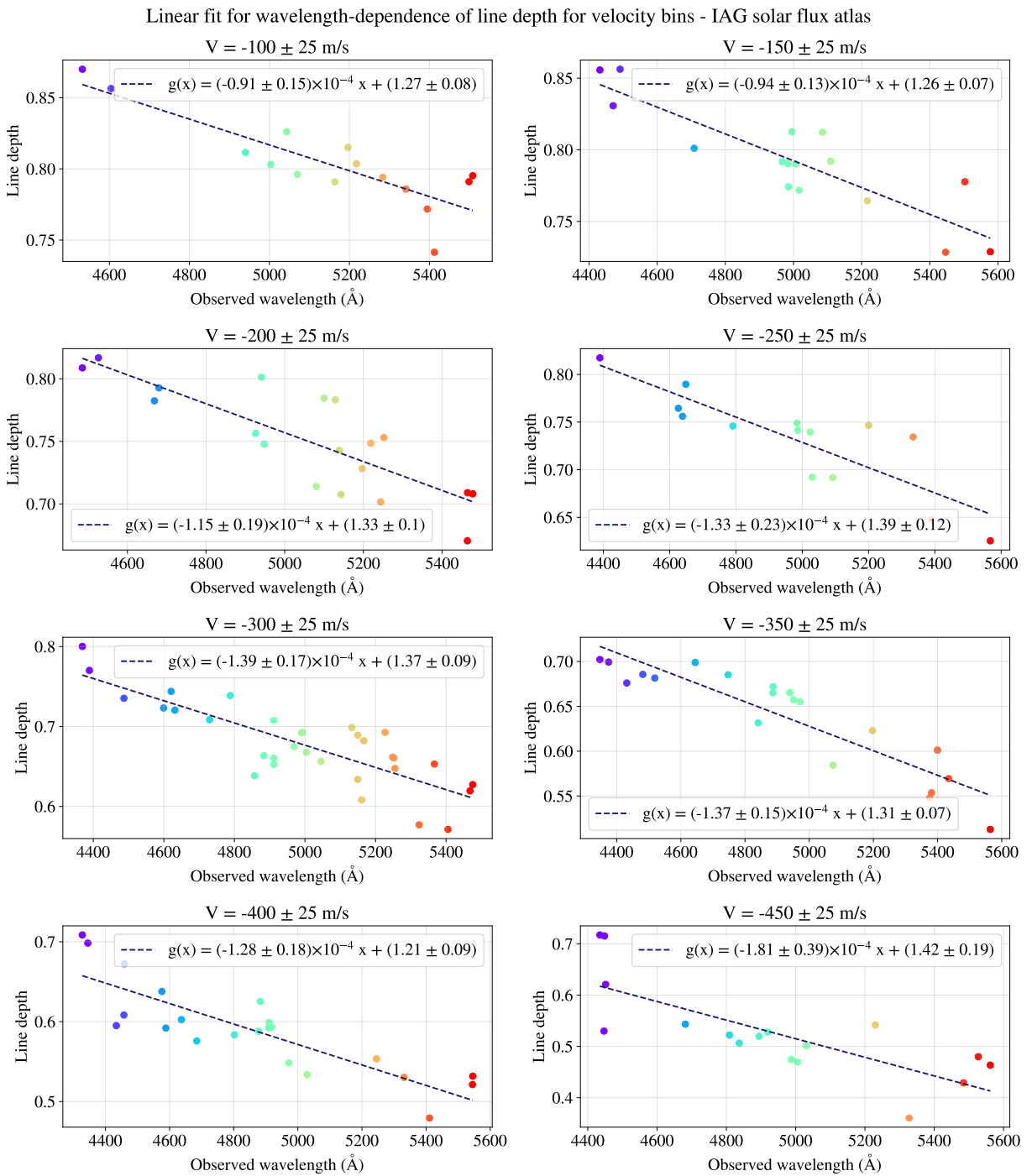


Figure 4.17: Individual plots of line depth against wavelength representing each bin of velocity in the visible range for the IAG solar flux atlas.

The third signature plot for the disk-center spectrum shows the same behavior, with a clear wave-

length dependence (see Figure 4.18). However, a visual inspection reveals that the trend between colors is more flattened than in the IAG solar flux atlas. This finding leads us to characterize the disk-center spectrum using the same methodology applied to the IAG solar flux atlas, searching for common physical characteristics.

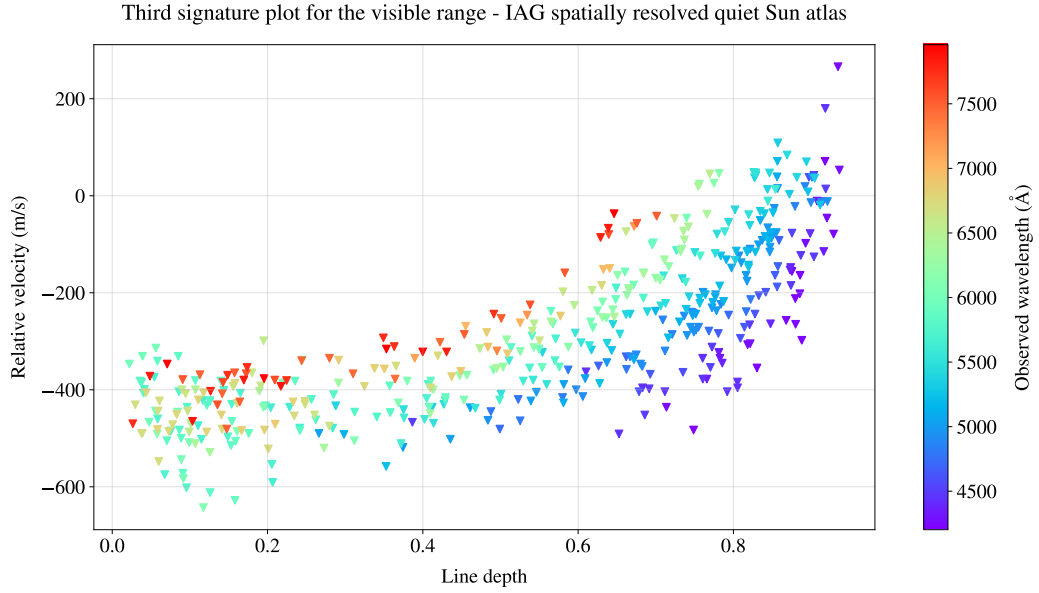


Figure 4.18: Third signature plot obtained for the visible range in the IAG spatially resolved quiet sun atlas.

Then, Figure 4.19 shows the results for each linear fit adjusted for the wavelength-dependence along line depth in the IAG spatially resolved quiet sun atlas at  $\mu = 1$ .

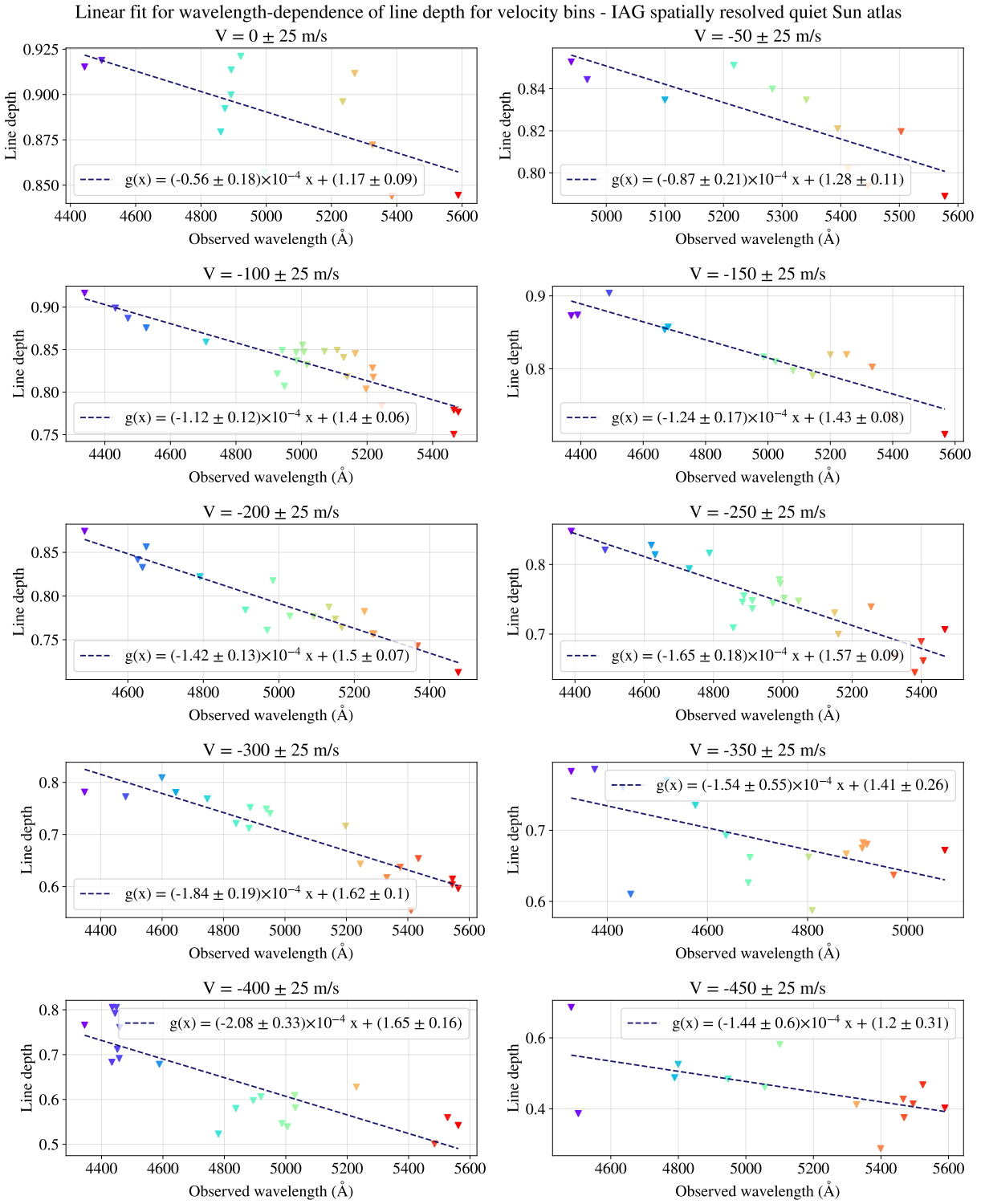


Figure 4.19: Individual plots of line depth against wavelength representing each bin of velocity in the visible range for the IAG spatially resolved quiet Sun atlas.

The coefficients from each linear fit applied to the velocity bins were plotted against velocity to identify patterns between the atlases. However, as there is no disk-center spectrum for the near-infrared range available for comparison, the coefficients are presented in Figure 4.20 but are not analyzed comparatively.

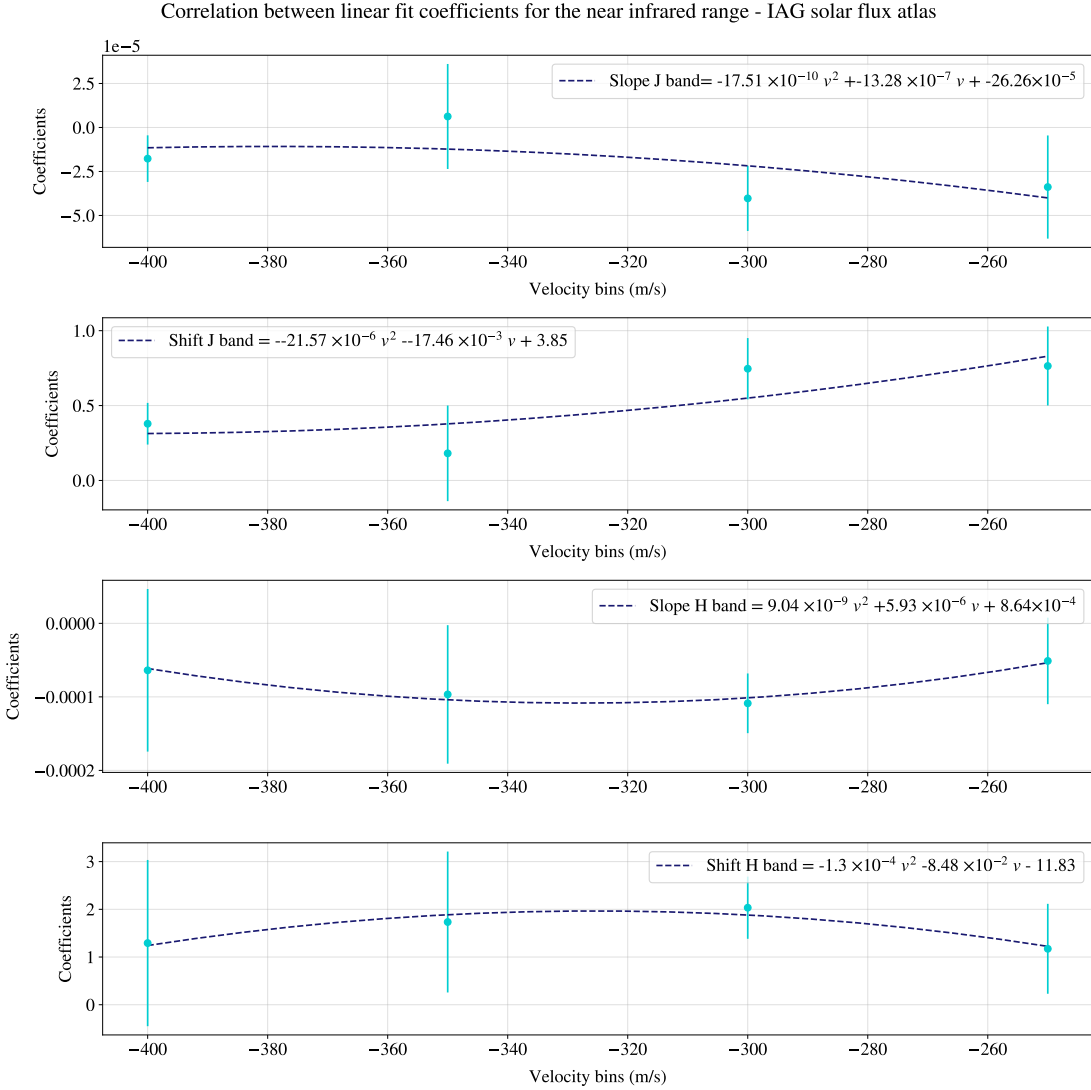
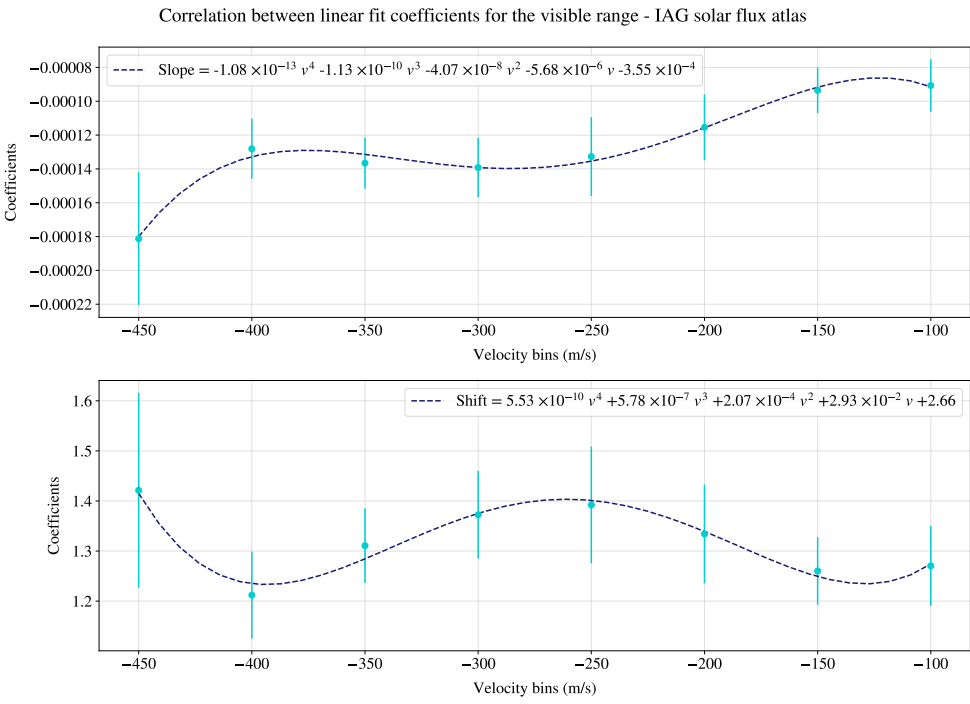
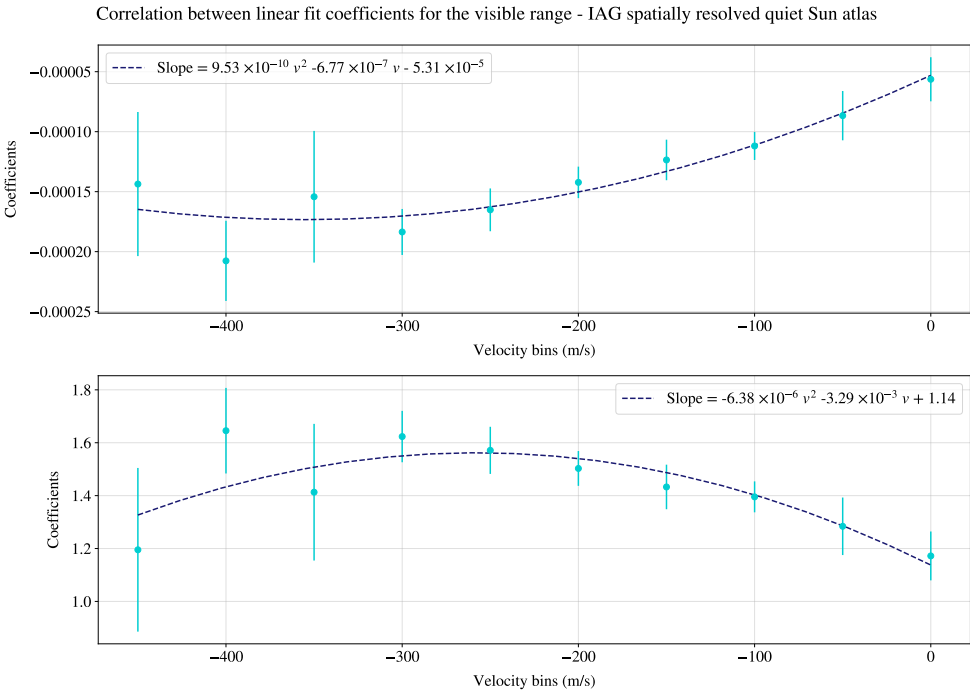


Figure 4.20: Coefficients of each lineal fit plotted against velocity bins separated by natural bands for the near infrared range in the IAG solar flux atlas.



(a) IAG solar flux atlas.



(b) IAG spatially resolved quiet Sun atlas.

Figure 4.21: Coefficients of each linear fit plotted against velocity bins for the visible range in both atlases.

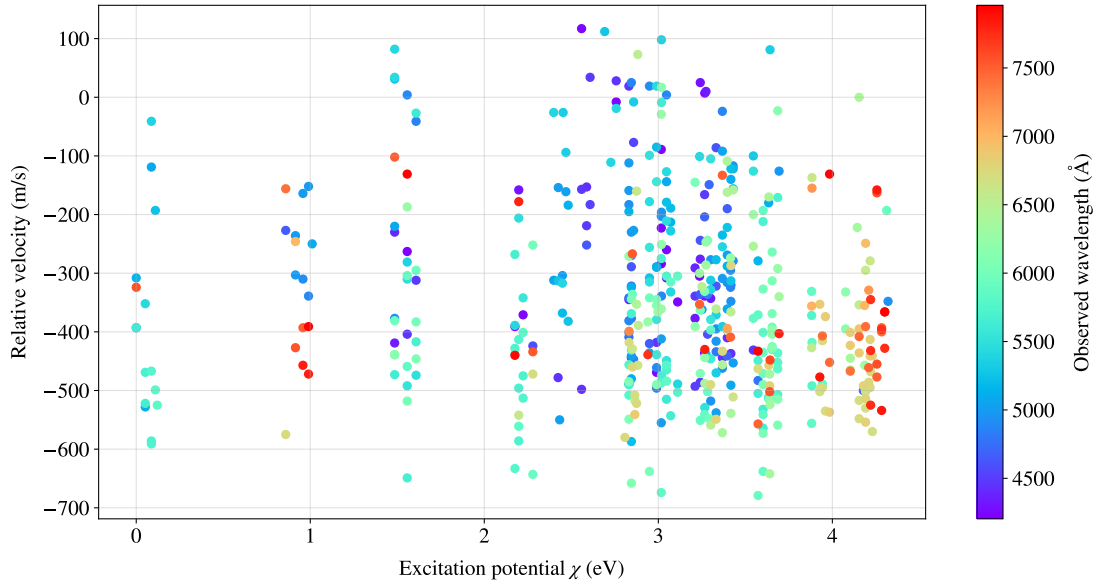
A comparison between the atlases for the visible range reveals a non-uniform trend in the IAG solar flux atlas. Furthermore, Figure 4.21 shows that the disk-integrated spectrum exhibits a more linear trend than the disk-center spectrum in the visible range. Therefore, the wavelength shift is uniform in the disk-center spectrum; and the wavelenght shift in the disk-flux spectrum shows the same behavior as the granulation curves. A detailed explanation of these final characteristics is provided in the sections that follow.

Although there is no theoretical explanation for the change in velocity displacement along the third signature plot, a key conclusion can be drawn: A phenomenon exists that generates the anomalous chromodependence, and it is not negligible in the disk-integrated spectrum. The initial hypothesis was that solar rotation would be the cause, but only if a velocity shift was present in the disk-integrated spectrum and absent at the disk-center. However, the velocity shift was observed in both spectral datasets, with the magnitude of the shift from the disk-center spectrum being greater than in the IAG solar flux atlas. This was unexpected, as rotational Doppler broadening is negligible at the disk center, thereby discarding rotation as the cause.

### 4.3.2 Line depth-dependence on excitation potential

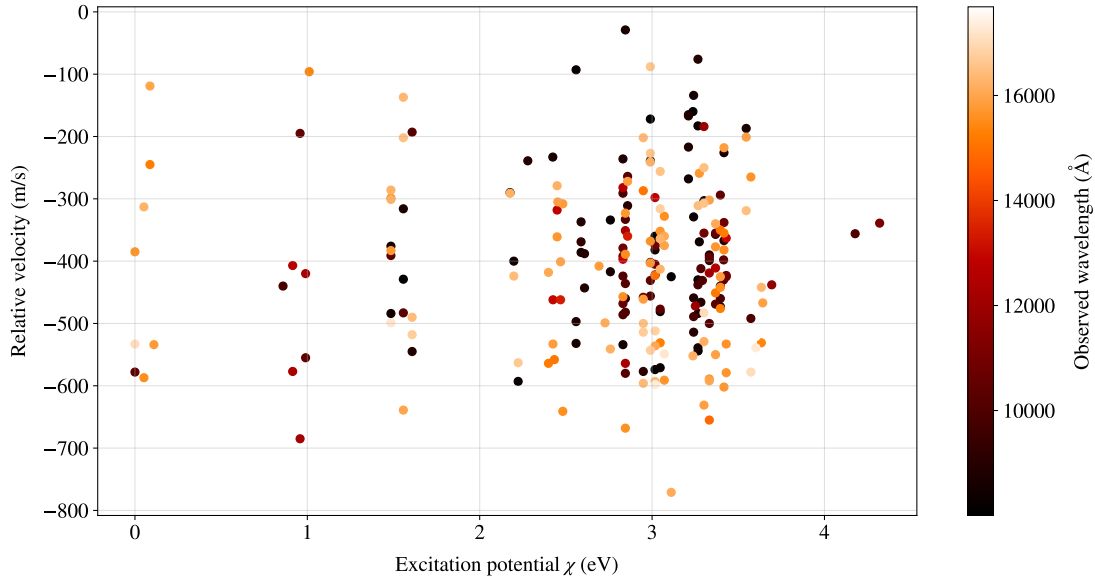
As shown Figure 4.22 the relative velocity was plotted against excitation potential ( $\chi$ ). The distribution of wavelength along excitation potential is according to literature, showing that lower wavelength have less excitation potential on the lowest energy level than high wavelength. However, if relative velocity is separated into bins of 100 m/s and plot the excitation potential against line depth, shifts in the excitation potential become apparent as shown Figure 4.23.

Distribution for excitation potential  $\chi$  on the relative velocity for the visible range  
IAG solar flux atlas



(a) Visible range.

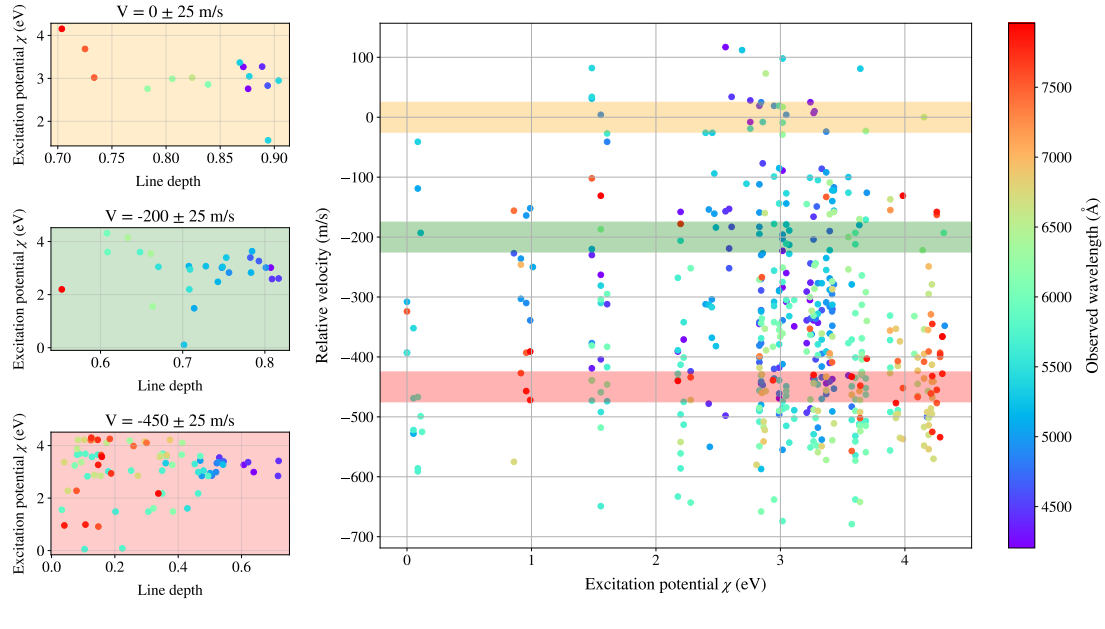
Distribution for excitation potential  $\chi$  on the relative velocity for the near infrared range  
IAG solar flux atlas



(b) Near infrared range.

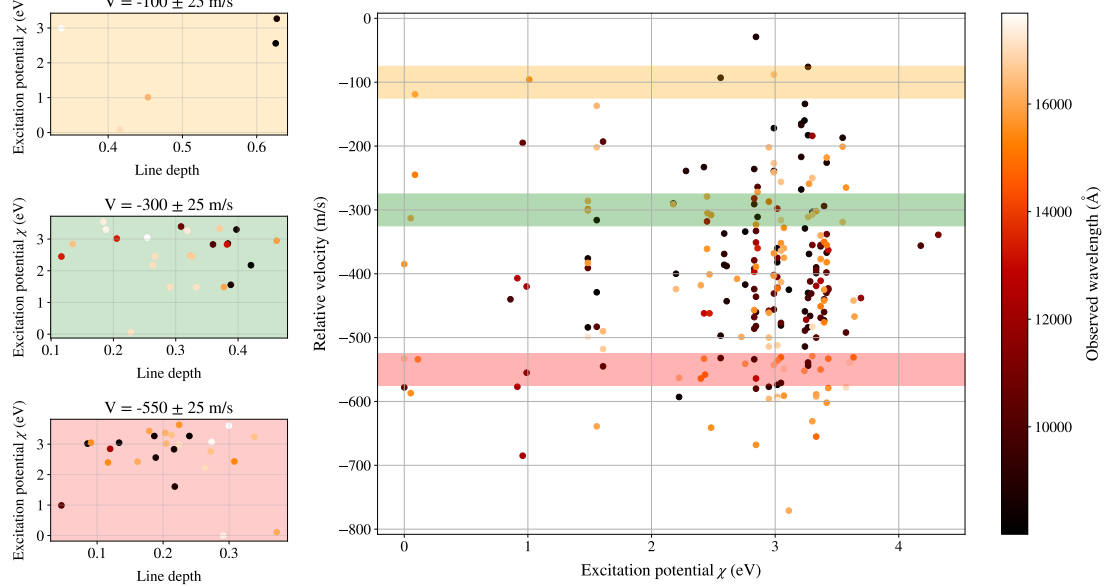
Figure 4.22: Relative velocity against excitation potential ( $\chi$ ) of the IAG solar flux atlas.

Velocity bins on the distribution of excitation potential  $\chi$  for the visible range - IAG solar flux atlas



(a) Visible range.

Velocity bins on the distribution of excitation potential  $\chi$  for the near infrared range - IAG solar flux atlas



(b) Near infrared range.

Figure 4.23: Velocity bins of 100 m/s across Figure 4.22, with this separation is visible the excitation potential shift across line depth.

Figure 4.23 explicitly shows the dependence on the highest values (2.5 to 5.0) eV for the exci-

tation potential of lower energy levels across line depth, which can be modeled with a lineal fit. Specifically, Figure 4.25 and Figure 4.24 shows the lineal fit for each velocity bins with a range of (2.5 – 5.0) eV for excitation potential. However, the near infrared range don't shows a uniform behavior across excitation potential. Then, we limit the line depth-dependence on excitation potential analysis to the visible range.

Figure 4.23 explicitly shows the dependence on excitation potential for the highest values (2.5 to 5.0) eV across line depth, which can be modeled with a linear fit. Specifically, Figure 4.25 and Figure 4.24 show the linear fit for each velocity bin within this excitation potential range (2.5 – 5.0) eV.

However, the near-infrared range does not exhibit a uniform behavior with excitation potential. Therefore, we limited the analysis of the line depth's dependence on excitation potential to the visible range.

Linear fit for the excitation potential-dependence across line depth for velocity bins for the near infrared range - IAG solar flux atlas

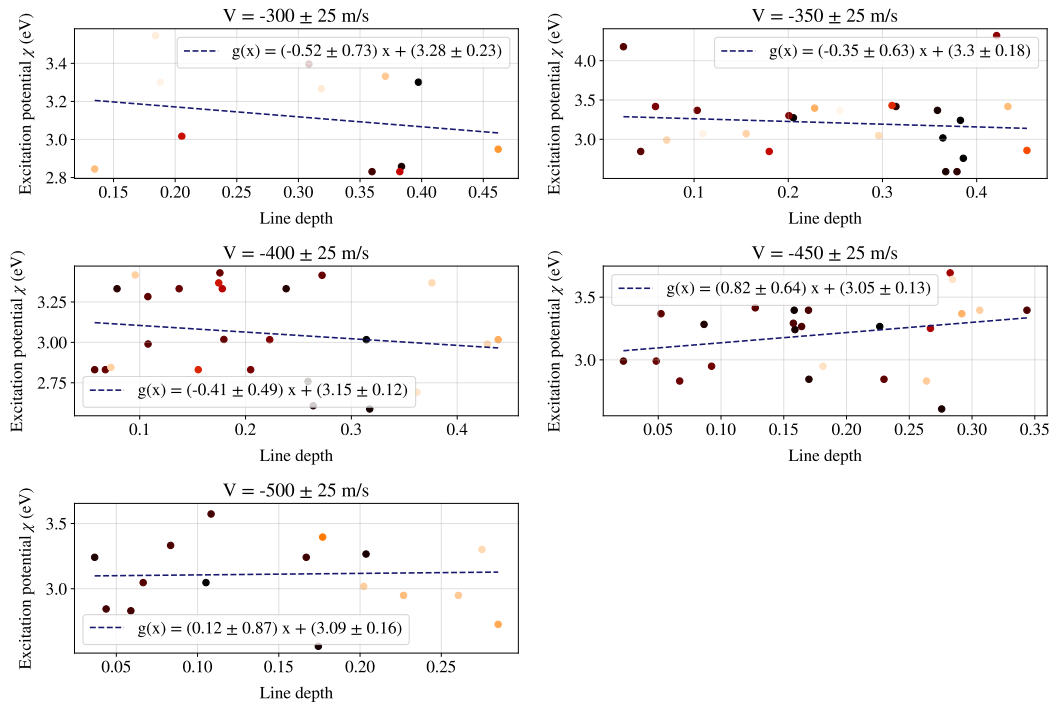


Figure 4.24: Individual plots for the range (2.5 to 5.0) eV of excitation potential across line depth, representing each bin of velocity for the near infrared range of IAG solar flux atlas.

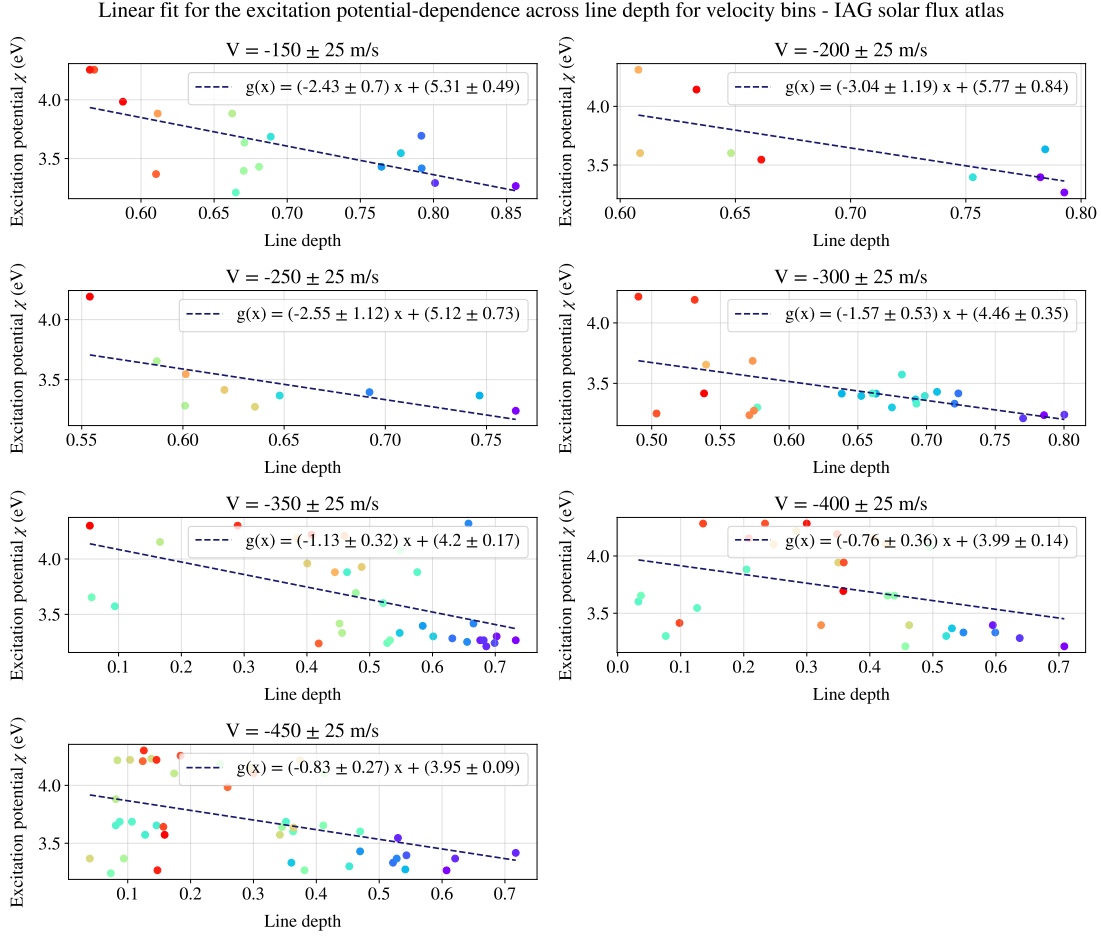


Figure 4.25: Individual plots for the range (2.5 to 5.0) eV of excitation potential across line depth, representing each bin of velocity for the visible range of IAG solar flux atlas.

To corroborate the only dependence on excitation potential ( $\chi$ ), the same analysis was performed on the IAG spatially resolved quiet Sun atlas at  $\mu = 1$ . Figure 4.26 shows the relative velocity against excitation potential ( $\chi$ ) for disk-center data.

Distribution for excitation potential  $\chi$  on the relative velocity for the visible range  
 IAG spatially resolved quiet Sun atlas

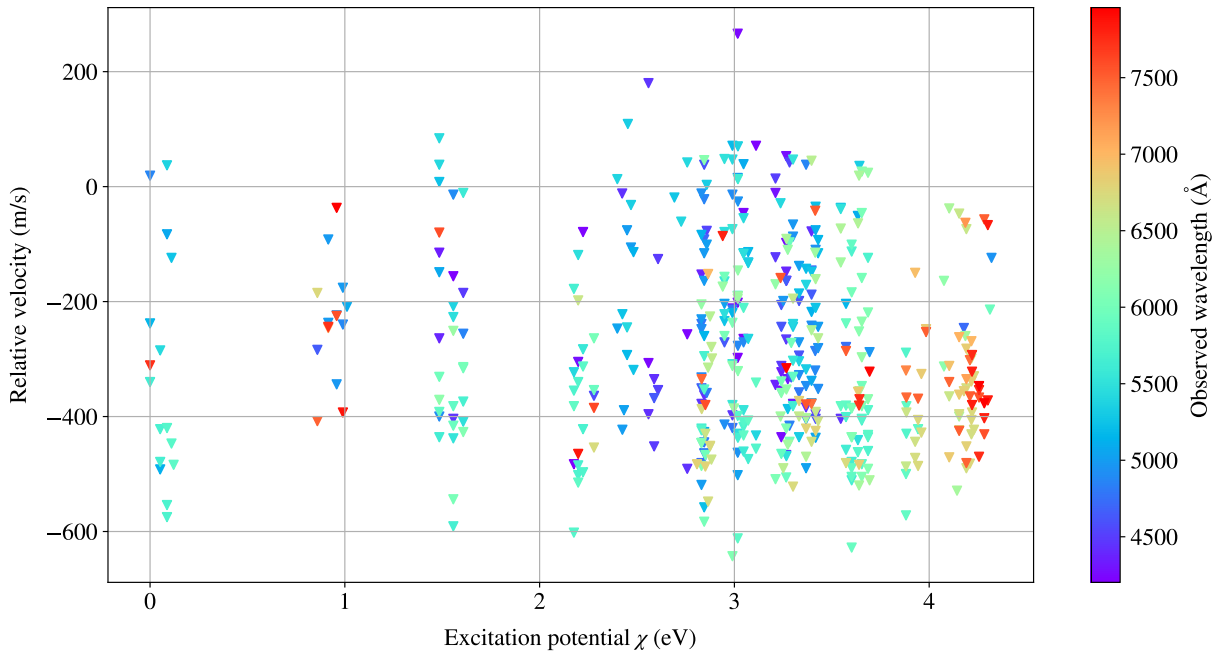


Figure 4.26: Relative velocity against excitation potential of lowest energy level in the visible range for the IAG spatially resolved quiet sun atlas.

Separating the relative velocity into bins of 100 m/s and taking the range (2.5 to 5.0) eV of excitation potential, the disk-center flux exhibits the same qualitative behavior as the IAG solar flux atlas (see Figure 4.27).

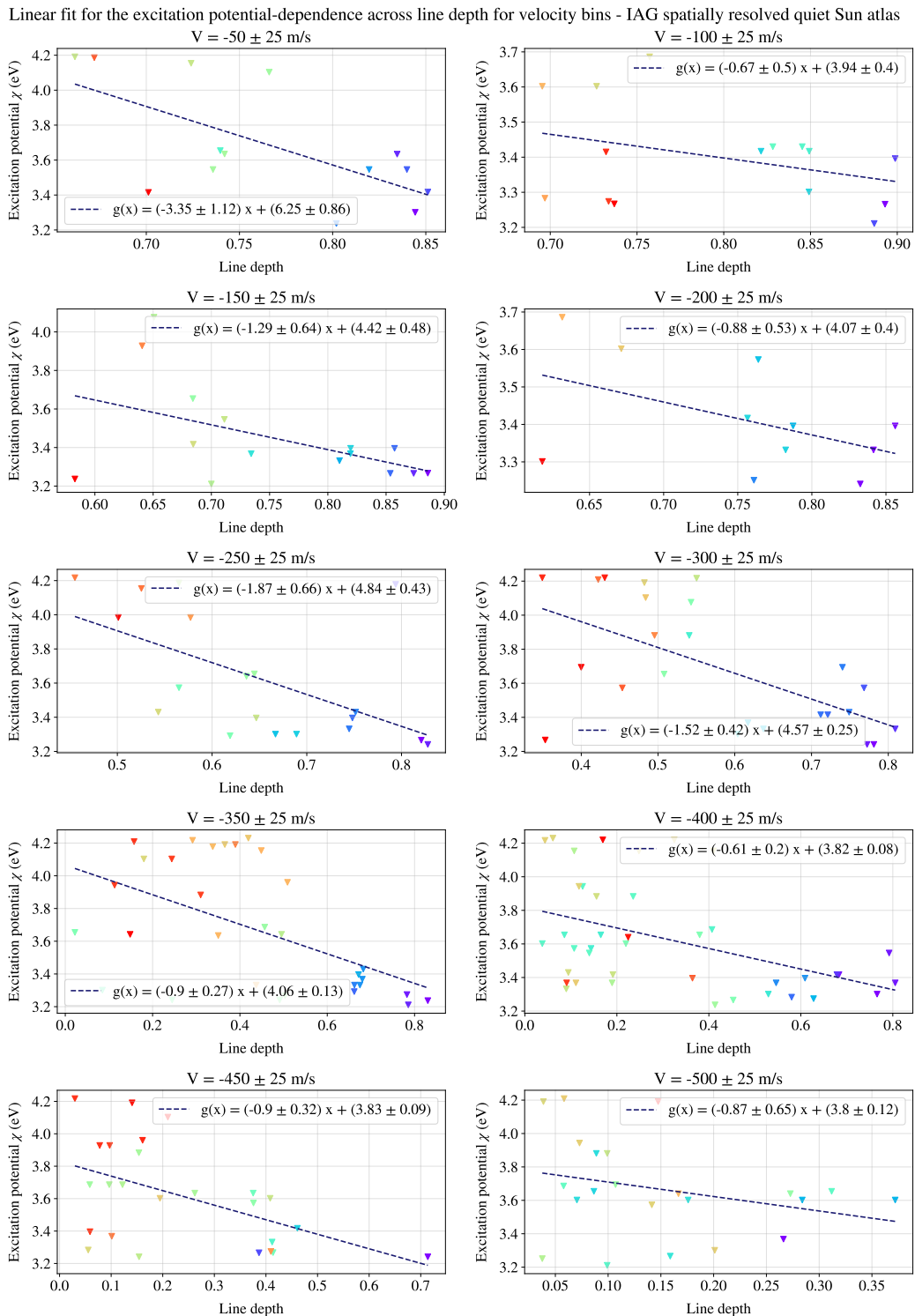
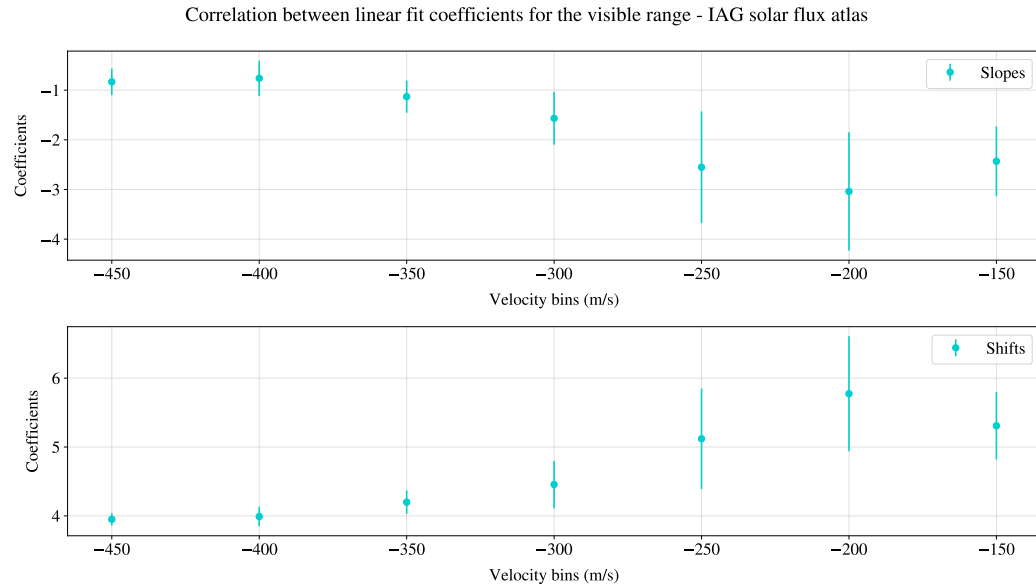
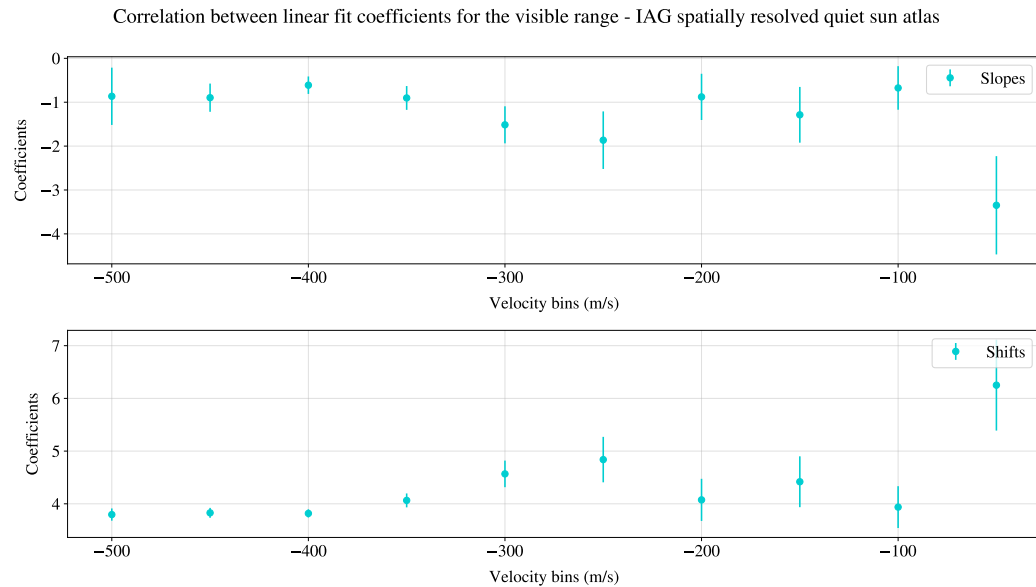


Figure 4.27: Individual plots for the range (2.5 to 5.0) eV of excitation potential of lowest energy level across line depth, representing each bin of velocity for the IAG spatially resolved quiet sun atlas.

To compare lineal fits between atlas we plotted the coefficients across velocity bins as shown Figure 4.28.



(a) IAG solar flux atlas.



(b) IAG spatially resolved quiet sun atlas.

Figure 4.28: Lineal fit coefficients for both atlases across velocity bins, the values show an increment with the velocity. In both atlas one plot mirrors the other, this is a consequence of the great uncertainty of these measurements.

Both graphs show a fluctuating behavior with increasing velocity. A quantitative difference exists, however, as the linear fit coefficients are higher than those reported for the disk-integrated atlas. For the velocity range of  $-175$  m/s to  $-525$ , the calculated slopes are similar, indicating a consistent relationship between energy shifts and velocity across this interval.

In the IAG solar flux atlas, the maximum displacement of excitation potential with line depth occurs at  $-200$  m/s. In contrast, the maximum occurs at  $0$  m/s in the IAG spatially resolved quiet Sun atlas.

Despite this difference, the overall shape of the plots is similar, with one appearing as a mirror of the other. This mirroring effect is likely a consequence of the significant uncertainty in these measurements more than a physical phenomenon.

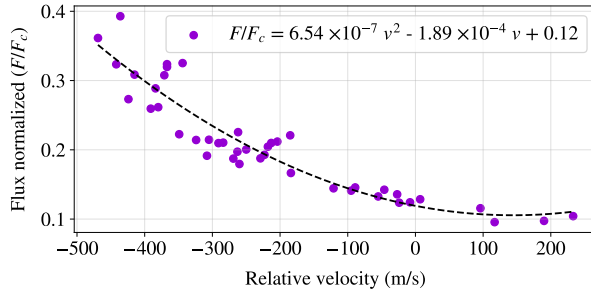
#### 4.3.3 Characterization of chromodependence on granulation pattern

As mentioned, the Figure 2.10 show the standard granulation curve proposed for Gray and Oostra [16], established on the range  $6020 \text{ \AA} - 6340 \text{ \AA}$  of wavelength. Since the standard granulation curve does not account for the full wavelength range, a different approach was adopted to describe all the ranges. The spectrum was separated into distinct color ranges, and a second-order polynomial was adjusted to each segment as shown Figure 4.29.

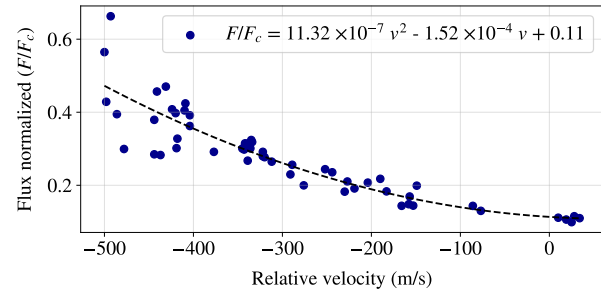
These color curves represent the granulation curves caused by the anomaly chromodependence, where the trend is more pronounced in the violet and red ranges. This can be interpreted as a shift and flattening of the standard granulation curve from Gray and Oostra towards shorter wavelengths.

Second order polynomial fits separated on colors range bins for the visible range - IAG solar flux atlas

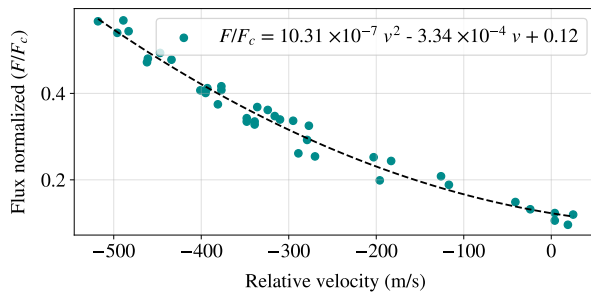
Wavelength range: 3800 Å - 4270 Å



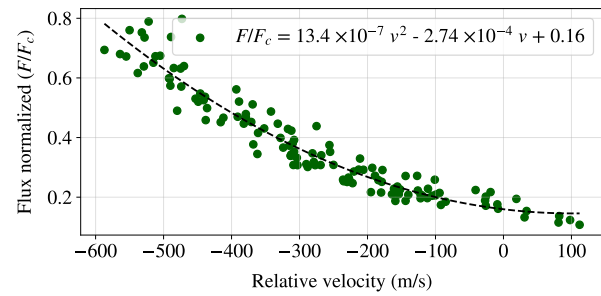
Wavelength range: 4270 Å - 4760 Å



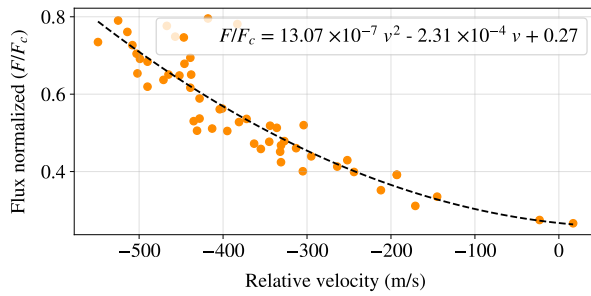
Wavelength range: 4760 Å - 4970 Å



Wavelength range: 4970 Å - 5700 Å



Wavelength range: 5700 Å - 6180 Å



Wavelength range: 6180 Å - 7500 Å

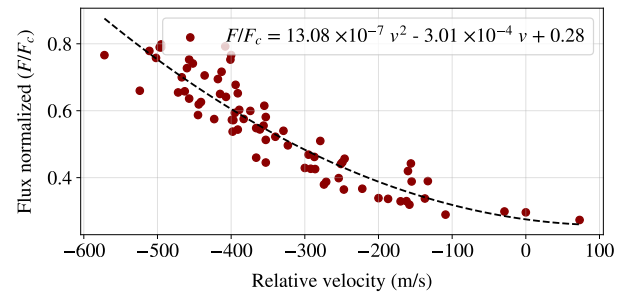


Figure 4.29: Different color curves adjusted to a specific range of the third signature plot for the visible range in the IAG solar flux atlas. The inclination on the curves is more pronounced in the violet than the red range.

On the other hand, chromodependence was also identified in the near infrared range, although it is less pronounced than in the visible spectrum. There were defined specific wavelength ranges by excluding regions dominated by telluric absorption lines, and linear relationships for each range were found (see Figure 4.30). However, unlike the visible range these relationships do not exhibit a unified correlation.

Lineal fits separated on colors range bins for the near infrared range - IAG solar flux atlas

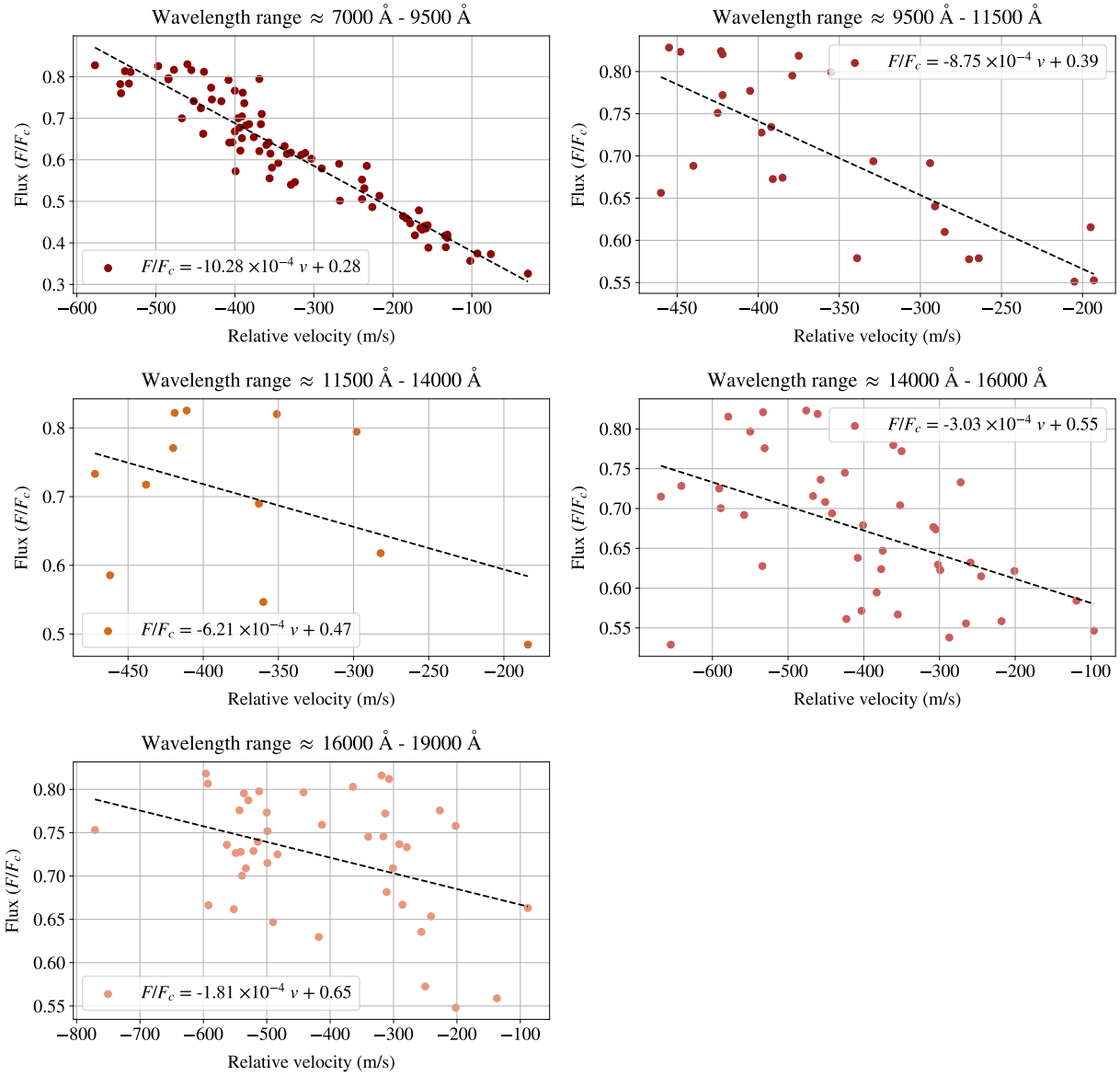


Figure 4.30: Different color granulation lines fitted to specific ranges on the third signature plot for the near infrared range in the Solar Flux Atlas.

To establish the characterization for all the wavelengths, plots of the fit coefficients were applied as shown Figure 4.31 and Figure 4.32.

Correlation between second order polynomial fit coefficients across wavelength for the visible range - IAG solar flux atlas

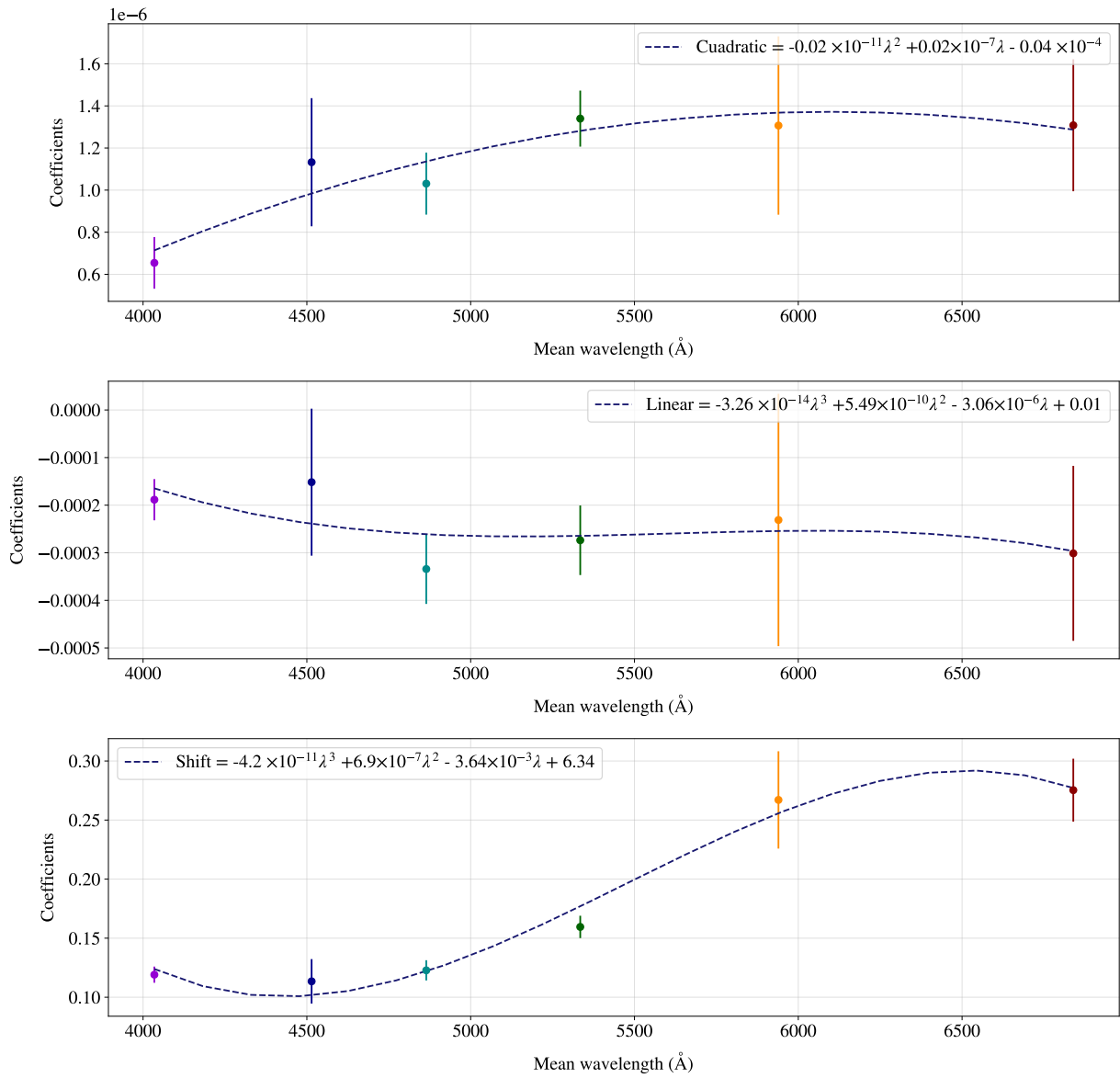


Figure 4.31: Second order coefficients for the visible range in the Solar Flux Atlas.

Correlation between linear fit coefficients across wavelength for the near infrared range - IAG solar flux atlas

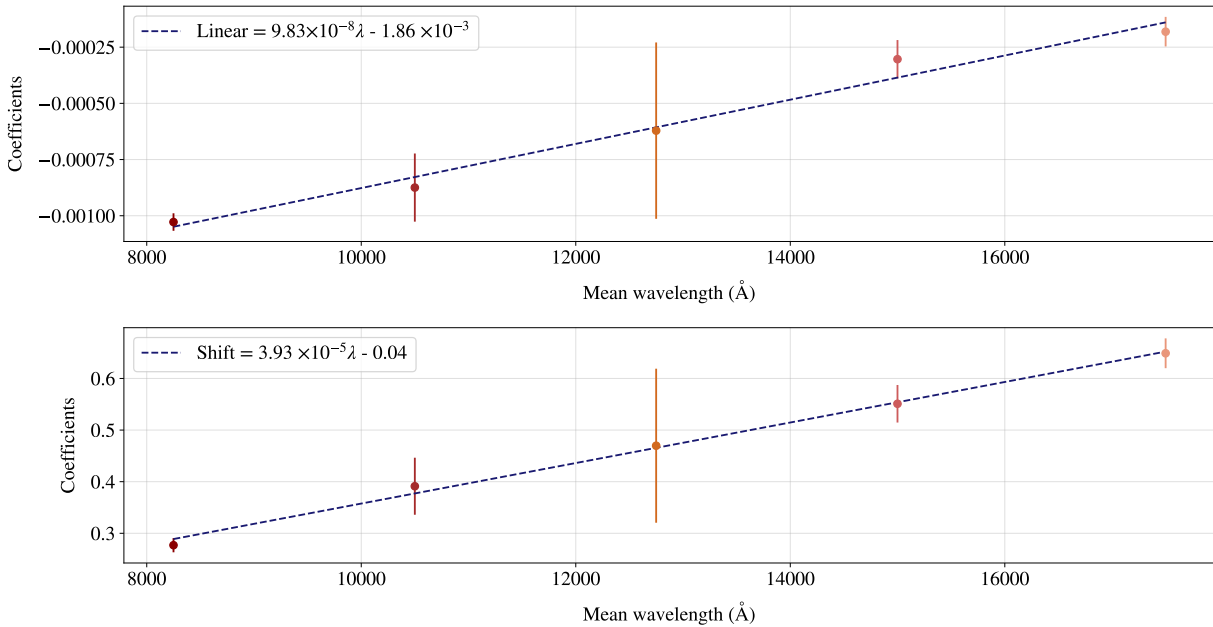


Figure 4.32: Lineal coefficient relation for the near infrared range in the Solar Flux Atlas.

Notice that the near infrared range had a lineal relation between coefficients, which leads us to report a standard granulation line as describe Equation (4.1).

$$\frac{F}{F_c}(\lambda, v) = (9.83 \times 10^{-8}\lambda - 1.86 \times 10^{-3})v + 3.93 \times 10^{-5}\lambda - 0.04 \quad (4.1)$$

In the case of the visible range, the coefficients for the individuals granulation curve shown in Equation (4.2) are listed in Table 4.1.

$$\frac{F}{F_c}(\lambda, v) = \alpha(\lambda)v^2 + \beta(\lambda)v + \gamma(\lambda) \quad (4.2)$$

Wavelength range ( $\text{\AA}$ )	$\alpha(\lambda) (\times 10^{-6})$	$\beta(\lambda)$	$\gamma(\lambda)$	$\sigma_\alpha (\times 10^{-7})$	$\sigma_\beta$	$\sigma_\gamma$
3800-4270	0.654	-0.0001	0.119	1.226	0.0004	0.0068
4270-4760	1.132	-0.0001	0.113	3.043	0.0001	0.0188
4760-4970	1.030	-0.0003	0.122	1.472	0.0001	0.0085
4970-5700	1.339	-0.0002	0.159	1.331	0.0001	0.0094
5700-6180	1.306	-0.0002	0.267	4.235	0.0002	0.0412
6180-7800	1.307	-0.0003	0.275	3.133	0.0001	0.0266

Table 4.1: Coefficients for the standard granulation curve dependent on wavelength of the visible range in the IAG solar flux atlas.

Equation (4.1) and Equation (4.2) describes the standard granulation curves for all the wavelength range in the IAG solar flux atlas. Therefore, gives a description about the anomalous chromodependence.

## 5. Conclusions

### Wavelength and line depth dependences

This project has characterized the convective blueshift in solar absorption lines and the anomalous chromodependence present across the three signatures of solar granulation: Line broadening, line asymmetry, and the line-depth dependence of convective blueshift following David Gray fundamental research (see [1] and references therein). A foundational outcome of this work is the production of a refined, blend-free list of Fe I lines, from which solar granulation patterns were derived with minimal scatter. This list, complete with measured parameters such as convective blueshift, line core curvature, line profile bisector slope, excitation potential, probability of transition, damping coefficient and line depth for each line, should be published to serve as an astronomy community resource. Furthermore, our analysis statistically justified a window of 0.1 Å around the line core as the optimal width for analysis. Our statistical analysis also demonstrates the precision of the spectral line selection and the optimal width parameter established by Allende and Garcia [19], whose methodology we followed.

A key contribution of this work is the detailed description of how granulation patterns vary with wavelength, leading to the establishment of color-dependent standard granulation curves for the entire spectrum. We confirmed the expected trend where deeper lines are generally located at shorter wavelengths. More significantly, we identified and characterized several anomalous signals of chromodependence: For a given line depth, short-wavelength lines exhibit greater convective blueshifts, higher (more positive or less negative) core bisector slopes, and narrower line profiles. Another relevant finding is that solar rotation is not the cause of this anomalous chromod-

ependence observed in the third signature, as the velocity shift was present and even greater in the disk-center spectrum where rotational broadening is negligible. For the near infrared range, the chromodependence closely follows a general trend line, with the line bisector slope shifting linearly with depth. In the more complex visible range, we identified individual granulation curves and described their governing coefficients.

Focusing now on the specific signatures, we find the analysis of the line core curvature for shallow lines revealed a clear linear trend in the visible range. The slope of this relationship was found to be  $(1.83 \pm 0.08) \times 10^{10} \text{ m}^{-1}$  for the disk-integrated flux and a significantly higher  $(2.94 \pm 0.16) \times 10^{10} \text{ m}^{-1}$  for the disk-center spectrum. The absence of wavelength dependence in this relationship indicates that line core curvatures are primarily governed by velocities (thermal, convective, and rotational), with negligible influence from atomic effects. The steeper slope at the disk-center confirms that rotation is a major contributor to line broadening in the integrated spectrum. By applying the theoretical model, we derived values for  $\langle v_{\text{conv}}^2 \rangle$  of  $3.15 (\text{km/s})^2$  for the disk-integrated flux and  $2.20 (\text{km/s})^2$  for the disk-center spectrum. The fact that the convective velocity appears lower at the disk center, where it should be most fully observable, points to an unresolved effect that needs further investigation.

Regarding line asymmetry, we focused on the middle range of line depths (0.3 – 0.6), where the convection effect is less pronounced. A clear wavelength dependence was observed in the line core bisector slopes for the visible range, in contrast to the poor dependence and significant scatter found in the near infrared. For a fixed line depth, the bisector slopes in the integrated flux spectrum decrease with wavelength. While the same general behavior was found in the disk-center spectrum, the magnitude of the displacement in bisector slope values was consistently smaller. This difference highlights the effect of limb darkening in producing non-uniform shifts in the integrated spectrum. The analysis of wavelength shifts at fixed velocities revealed that for the disk-integrated spectrum, the shift is not uniform but fluctuates, while the disk-center spectrum exhibits a uniform, quadratically increasing behavior.

Finally, the study into the line depth-dependence on excitation potential revealed that the phenomenon is most pronounced for high-excitation potentials (2.5 to 5.0 eV) and is best modeled in the visible range due to non-uniform behavior in the near infrared. The resulting coefficients

depend strongly on wavelength and weakly on excitation potential. A notable finding is the difference in the velocity of maximum displacement cause it occurs at  $-200$  m/s for the disk-integrated flux but shifts to 0 m/s for the spatially resolved quiet Sun atlas.

For future work, it is imperative to study atomic broadening effects and develop more sophisticated models of convection to investigate the roles of temperature and density fluctuations in driving the anomalous chromodependencies uncovered in this study. The standard granulation curves and the comprehensive line list provided here offer a robust foundation for such endeavors. Finally, the statistical analysis performed suggests that an algorithm could be developed to select customized window widths based on specific spectral line conditions.

## A. Appendix

### Z-score Standardization

The function `np.polyfit()`, during the process of calculating the fourth-order polynomial fit, presents an over estimation of the coefficients due to the large difference of magnitude order between axes. To deal with this difference, a z-score standardization was applied on the selected bins of wavelengths around the minimum reference point. This process helps to avoid the dominance of certain features over others due to differences in their scales [21].

For the standardization Equation (A.1) was applied on the selected bins for wavelength around the minimum reference point.

$$\lambda_{\text{scaled}} = \frac{\lambda_{\text{original}} - \mu(\lambda_{\text{original}})}{\sigma(\lambda_{\text{original}})} \quad (\text{A.1})$$

Where  $\mu(\lambda_{\text{original}})$  refers to the mean and  $\sigma(\lambda_{\text{original}})$  to the standard deviation of the wavelength range. In terms of calculating derivatives for the first and second signature of convection, the standardization on the variable required a re-scaled factor of conversion for obtain the original values. Based on the definition for the standardization, the derivatives of the expression (A.1) have to follow Equation (A.2).

$$\frac{d}{d\lambda_{\text{original}}} = \frac{1}{\sigma(\lambda_{\text{original}})} \frac{d}{d\lambda_{\text{scaled}}} \quad (\text{A.2})$$

Therefore, the original values for derivatives evaluated in the observed wavelength are expressed in Equation (A.3)

$$\frac{d^2}{d\lambda_{\text{original}}^2} = \frac{1}{\sigma(\lambda_{\text{original}})^2} \frac{d^2}{d\lambda_{\text{scaled}}^2} \quad \frac{d^3}{d\lambda_{\text{original}}^3} = \frac{1}{\sigma(\lambda_{\text{original}})^3} \frac{d^3}{d\lambda_{\text{scaled}}^3} \quad (\text{A.3})$$

The treatment proposed solves the problem for the large difference of magnitude order between axes.

## B. Appendix

### The third derivative relation

The third derivative relation or called the line core bisector slope was deduced by Professor Benjamin as shown below.

Define the slope for the minimum point of an asymmetric curve as Equation (B.1), where the points  $b, c, h$  are illustrated in Figure (B.1).

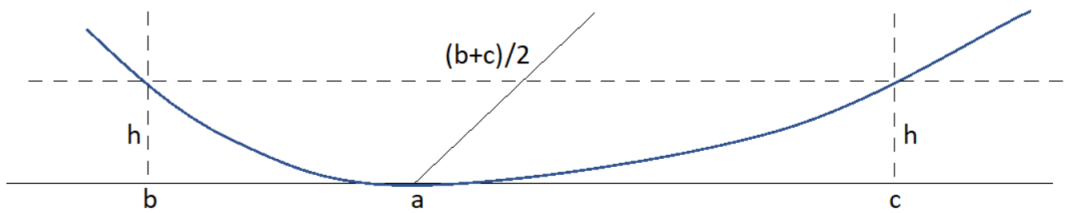


Figure B.1: Illustration for the points  $a, b, c$  and the height which defines the line Core Bisector Slope CBS (see Equation (B.1)).

$$CBS = \lim_{h \rightarrow 0} \frac{\frac{b+c}{2} - a}{h} \quad (B.1)$$

Due to an asymmetric line profile shape the curve should be expanded around the point  $a$  (line core) by Taylor series.

$$f(c) = f(a) + (c - a)f'(a) + \frac{1}{2}(c - a)^2 f''(a) + \frac{1}{6}(c - a)^3 f'''(a) \dots \quad (B.2)$$

The point  $a$  is chosen at the minimum, so  $f'(a) = 0$  and  $f(c) - f(a) = h$ , given Equation (B.3).

$$2h = (c - a)^2 f''(a) + \frac{1}{3}(c - a)^3 f'''(a) \quad (\text{B.3})$$

The minimal points were abbreviated as  $c - a = x > 0$  and likewise  $b - a = y < 0$  obtaining Equation (B.4).

$$2h = x^2 f''(a) + \frac{1}{3}x^3 f'''(a) \quad 2h = y^2 f''(a) + \frac{1}{3}y^3 f'''(a) \quad (\text{B.4})$$

As both variables has identical equations,  $x$  and  $y$  are two of the equations roots which leads to define the CBS like Equation (B.5).

$$CBS = \lim_{h \rightarrow 0} \frac{x + y}{2h} \quad (\text{B.5})$$

Of the three possible roots of a cubic equation, the two that we need are those that tend to Equation (B.6)

$$\lim_{h \rightarrow 0} \frac{x}{y} = -1 \quad (\text{B.6})$$

If the polynomial third-order equation is written in the standard form, the coefficients becomes relation (B.7).

$$ax^3 + bx^2 + cx + d = 0 \quad \rightarrow \quad a = \frac{f'''(a)}{3} \quad b = f''(a) \quad c = 0 \quad d = -2h \quad (\text{B.7})$$

A standard procedure is to change the variable  $x$  to produced a reduced equation as follows.

$$x = t - \frac{b}{3a} = t - \frac{f''(a)}{f'''(a)} \quad (\text{B.8})$$

Moreover, the variable change allows to express the Taylor series as a third-order polynomial fit, as shown in Equation (B.9).

$$t^3 + pt + q = 0 \quad \rightarrow \quad p = -3 \left( \frac{f''(a)}{f'''(a)} \right)^2 \quad q = 2 \frac{(f''(a))^3 - 3h(f'''(a))^2}{(f'''(a))^3} \quad (\text{B.9})$$

The Equation (B.9) have three solutions given Equation (B.13).

$$t_i = 2 \left( \frac{f''(a)}{f'''(a)} \right) \cos \left( \frac{1}{3} \arccos \left( \frac{3h(f'''(a))^2}{(f''(a))^3} - 1 \right) - \frac{2\pi i}{3} \right) \quad i = 0, 1, 2 \quad (\text{B.10})$$

When  $h$  vanishes, there are two equal solutions  $\cos(\theta) = 1/2$  and one differing  $\cos(\theta) = -1$ .

Taking a parameter  $\epsilon$ , when  $h$  vanishes  $\epsilon \ll 1$ , we abbreviated the expression to Equation (B.11).

$$\epsilon = \frac{h(f''')^2}{(f'')^3} \ll 1 \quad t_i = 2 \left( \frac{f''(a)}{f'''(a)} \right) \cos \left( \frac{1}{3} \arccos(3\epsilon - 1) - \frac{2\pi i}{3} \right) \quad (\text{B.11})$$

In the limit  $h \rightarrow 0$ ,  $\delta = \sqrt{6\epsilon}$  and the trigonometric expression were restricted as Equation (B.12).

$$\arccos(3\epsilon - 1) = \pi - \delta \quad \delta \ll 1 \quad \rightarrow \quad 3\epsilon - 1 = \cos(\pi - \delta) = -\cos(\delta) \approx \frac{\delta^2}{2} - 1 \quad (\text{B.12})$$

Therefore, the solutions for the Taylor expansion are expressed by Equation (B.13).

$$t_{\pm} = 2 \frac{f''(a)}{f'''(a)} \left( \frac{1}{2} \cos \left( \frac{\sqrt{6\epsilon}}{3} \right) \mp \frac{\sqrt{3}}{2} \sin \left( \frac{\sqrt{6\epsilon}}{3} \right) \right) \quad (\text{B.13})$$

For the line core bisector slope appears the condition (B.14).

$$x + y = t_+ + t_- - 2 \left( \frac{f''(a)}{f'''(a)} \right) = -\frac{2}{3} \left( \frac{f''(a)}{f'''(a)} \right) \left( \frac{h(f''')^2}{(f'')^3} \right) = -2h \frac{f'''(a)}{3(f'')^2} \quad (\text{B.14})$$

Whence, finally, the core bisector slope is defined by Equation (B.15)

$$CBS = -\frac{f'''(a)}{3(f'')^2} \quad (\text{B.15})$$

This result is a wavelength interval, so multiplying by the relation  $(c/\lambda)$  gives it a more universal meaning.

## C. Appendix

### Visualizer for outliers

For the process of Fe I line selection was created a visualizer, using the Tkinter python library, to aid in identifying blend lines or those outside the spectrum. In order to make this process less stressing a little tools bar was created to facilitate the label and deleting process is presented in Figure C.1.

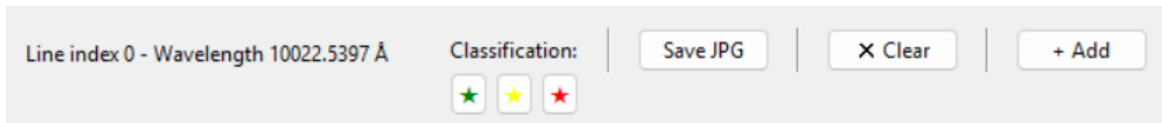
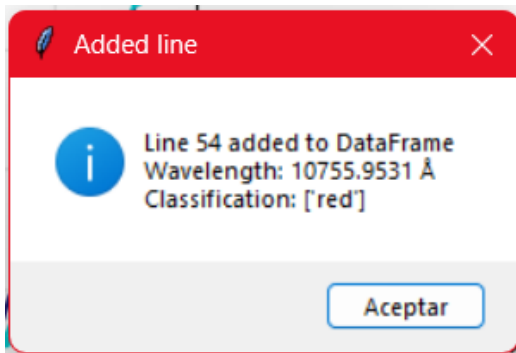


Figure C.1: Tools bar for the visualizer, containing a classification system of labels, the option to save images, and add to a Dataframe for dropping.

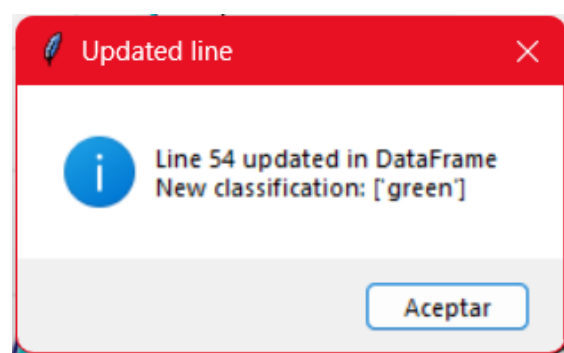
It features a custom classification system, shown as color stars. We present the guide using in the project: Red is for a discarded line, yellow indicates that the line needs further check, and green is for a line approved. If it is necessary to change the label, use the button "X Clear" first and then give another label to the line. These buttons don't make changes on the Dataframe more than just a label for the user orientation. Even if the lines have or not the label for good ones, the code just delete the lines which are added to the Dataframe of filtered lines.

To make a list of lines which are going to be deleted or filtered use the button "+ Add", which includes the line core information with the label given. If this process was successful, the message shown in Figure C.2a should appear. On the other hand, if the label of a line was changed when it was already saved as a discarded line, it can be updated. Give the other label and use the button

"+ Add", should appear the message from Figure C.2b.



(a) Message for an added line to the Dataframe.



(b) Message for an updated line to the Dataframe.

Figure C.2: The messages shows the index, wavelength and classification for the line added or updated.

When the visualizer is close, the code returns a Dataframe with the dropped lines (lines added) and filtered lines (rest of the lines). The option for "Save JPG" of the graph is available, for saving the image in JPG format and showing the confirmation message with the index and wavelength of the line (see Figure C.3).

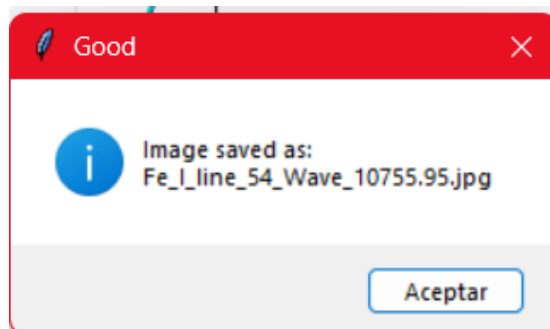


Figure C.3: Confirmation message for save the image in format JPG of the graph with the information of the line.

Furthermore, was created a navigation bar which help to locate a specific line or exploring the different graphs.

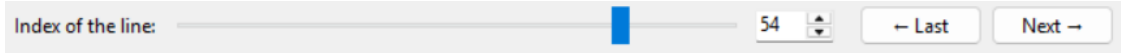


Figure C.4: Navigation bar for the visualizer, helps to locate a specific line or exploring the different graphs using a slider, writing box, and buttons for moves.

This bar counts with a slider and a box to locate the line by using the index it appears in the original list (see Figure C.4). Also, counts with the buttons " $\leftarrow$  Last" and " $\rightarrow$  Next" to move between graphs.

Two versions of the visualizer were developed, each one applying different filters. The first filter displays the geometry of the line core and line profile as shown Figure C.5.

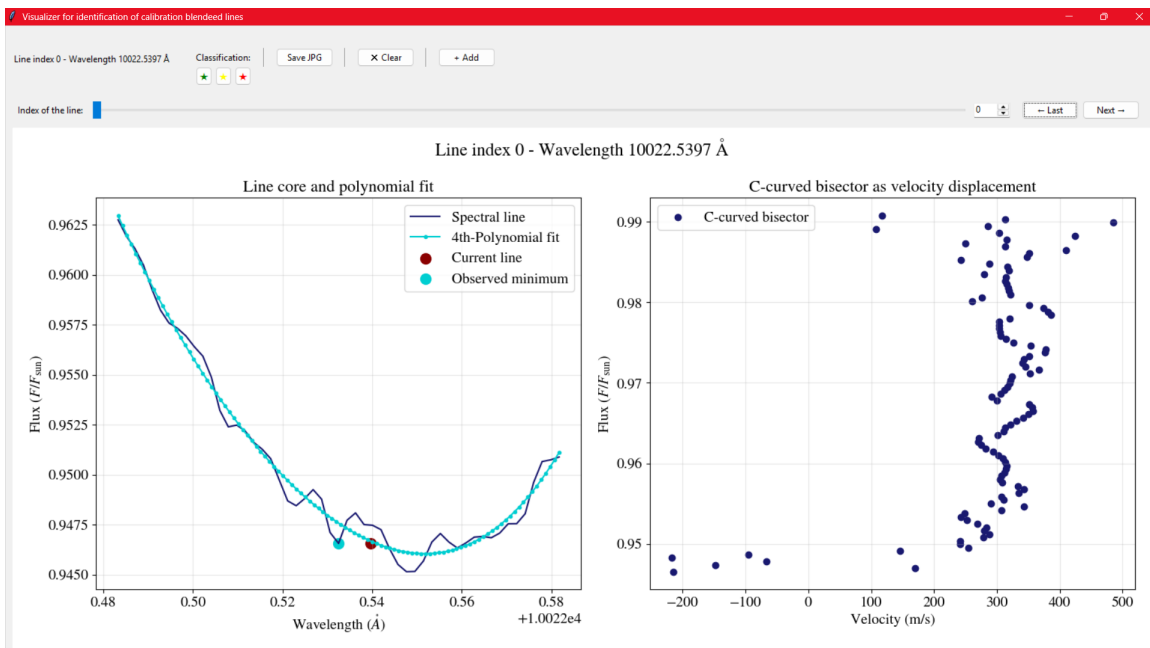


Figure C.5: General view for the results of the first filter. It shows the line core and the fourth-order polynomial fit with the line profile bisector.

This version shows the line core and the fourth-order polynomial fit, in parallel with the line profile bisector of each one in terms of velocity. The objective of the first filter is to reduce the number of lines for analyzing the three signatures of convection.

The second filter, which is build on the selected lines from the first filter, shows the three signatures of convection and the behavior of the selected line core in each one (see Figure C.6).

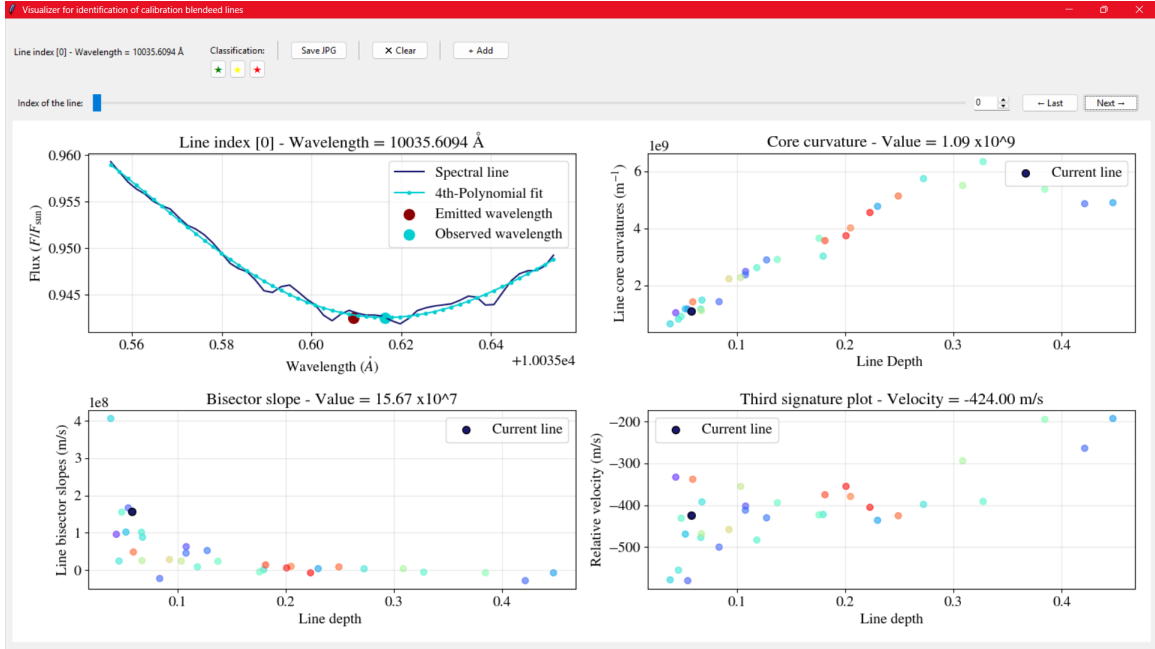


Figure C.6: General view for the results of the second filter. It shows the three signatures of convection with the line profile.

This version exhibits all the three signatures graphics including the line core with the fourth-order polynomial fit. In each graphic of derivatives the corresponding Fe I is resalted, this with the finally to select lines depending on his behavior.

The visualizer and the filters significantly reduced the time spent reviewing lines. For this reason, the code for this tool can be seen on [GitHub Repository](#), along with a test example provided below.

## C.1 Test example

The main code for this project is contained in the Jupyter notebook file `Visualizer.ipynb`, and a test example dataset is provided in the excel file `Test_example`. On the first part of the code two DataFrames were created: One for the spectrum with columns Wave and Flux, representing wavelength in armstrongs and normalized flux, respectively; and another for the list of Fe I lines. Run the next cell code for upload the raw data from the excel file and create the Dataframe of the spectrum with columns Wave and Flux.

```

#Data from Vzier without treatment 10000 A- 11000 A
raw_data = pd.read_excel(r"C:\Users\clauw\Documents\
    Programming\Final-Project\Project\Visualizer\Data\
    Test_example.xlsx")

#Convert the wavelength in A cause its in cm^-1
raw_data['Wave A'] = (10**8)/raw_data['Wave (cm)']

#Invert the values for the index in python
raw_data = raw_data.sort_values('Wave A', ascending=True,
    na_position='first').reset_index(drop=True)

```

Feel free to modify this line to read the file type. The idea is the Dataframe results have the columns Wave (cm), nFlux and Wave A. There's no need for the flux to be normalized, because nothing in the code uses this condition. Then run the next cell code for create the Dataframe with calibration lines.

```

#List of Fe I lines
raw_lambda = pd.read_excel(r"C:\Users\clauw\Documents\
    Programming\Final-Project\Project\Visualizer\Data\Nave list
    example.xlsx")

raw_lambda['Nave list'] = (10**8)/raw_lambda['lambda']
raw_lambda = raw_lambda[raw_lambda['Nave list'].between
    (10000,11000,inclusive='right')] #Separate the range for
    use, in this case 10000-11000
raw_lambda = raw_lambda[raw_lambda['class']=='A'].reset_index(
    drop=True) #Just take the quality A lines

```

In this case, we use the Nave list of Fe I lines. A test example list is displayed on the folder Data. For the first filter we use two different functions. The function `find_minimuns` was used to select the closest minimums to the Fe I lines, along with their associated flux values and Fe I

line wavelengths. Beware, these Fe I line wavelengths serve as reference points for selecting bins around each line, rather than representing observed wavelengths. The closest lines to the Nave list values were selected as the minimum from the absolute value between the wavelengths. We discard any lines with distances between minimums and Fe I lines exceeding 10 mÅ. To use the function run the next code line.

```
closer_lines_first_filter = find_minima(raw_data['Wave A'],
                                         raw_data['nFlux'], raw_lambda['Nave list'])
```

The function `width_minima` selects the bins of 50 mÅ and 0.2 Å around the minimal point, respectively for the line core and the line profile. Each window corresponds to one index on the Dataframe of closer Fe I lines. Run the next cell to create the bins for the line core and the the line profile.

```
local_points_first_filter = width_minima(
    closer_lines_first_filter, raw_data, 0.05) #The window for
    the observed wavelength
local_points_bis_first_filter = width_minima(
    closer_lines_first_filter, raw_data, 0.2) #Window for the
    bisector with all the line
```

Then, the function First Filter finds the fourth-order polynomial fit and calculates the minimum point with the second derivative of the fit, that is the observed wavelength. This returns a Dataframe with the value of Fe I line associated, the polynomial fit, and the observed wavelength. In parallel, the line profile bisector is calculated using the midpoint method where equal points of flux are selected for comparison. Use the next line code for call the function.

```
Values_first_filter, Fit_first_filter, Local_first_filter,
Bisector_first_filter = First_Filter(
    local_points_first_filter, closer_lines_first_filter,
    local_points_bis_first_filter)
```

Furthermore, to ensure the typical absorption line shape, fourth-order polynomial fits with non-positive second-order coefficients were discarded. Also an approximation was used to discard

lines that do not belong to the spectrum. A computational form of a slope can be seen as the difference between the maximum and minimum point of the list of points. In terms of flux if it is seen the distance can't be more than a half of the absolute difference. This lets us discard pronounced slopes without affecting or filtering weaker lines.

To display the visualizer, uncomment the following line code in the cell corresponding to it.

```
#CHANGE THIS LINE - The order: local_points, values, fit,
    bisectors
app = OutlierViewer(root, Local_first_filter,
    Values_first_filter,Fit_first_filter,Bisector_first_filter)
```

**Note:** Sometimes the first plot of the visualizer can be displaced due to the Tkinter library. To fix this, just move to another line and back to the wished one.

We recommend eliminating the lines that follow one of the conditions presented. First, the line profile bisector doesn't show a C-curved bisector or it's too affected by the noise. Second, the polynomial fit and the line profile don't follow a common absorption line form. This can be interpreted as the position on other points to the fit. Third, the line core shows two minimums or a protuberance. These are blended lines. An example of this behavior is shown on Figure C.7 and an example of accepted lines is shown in Figure C.8.

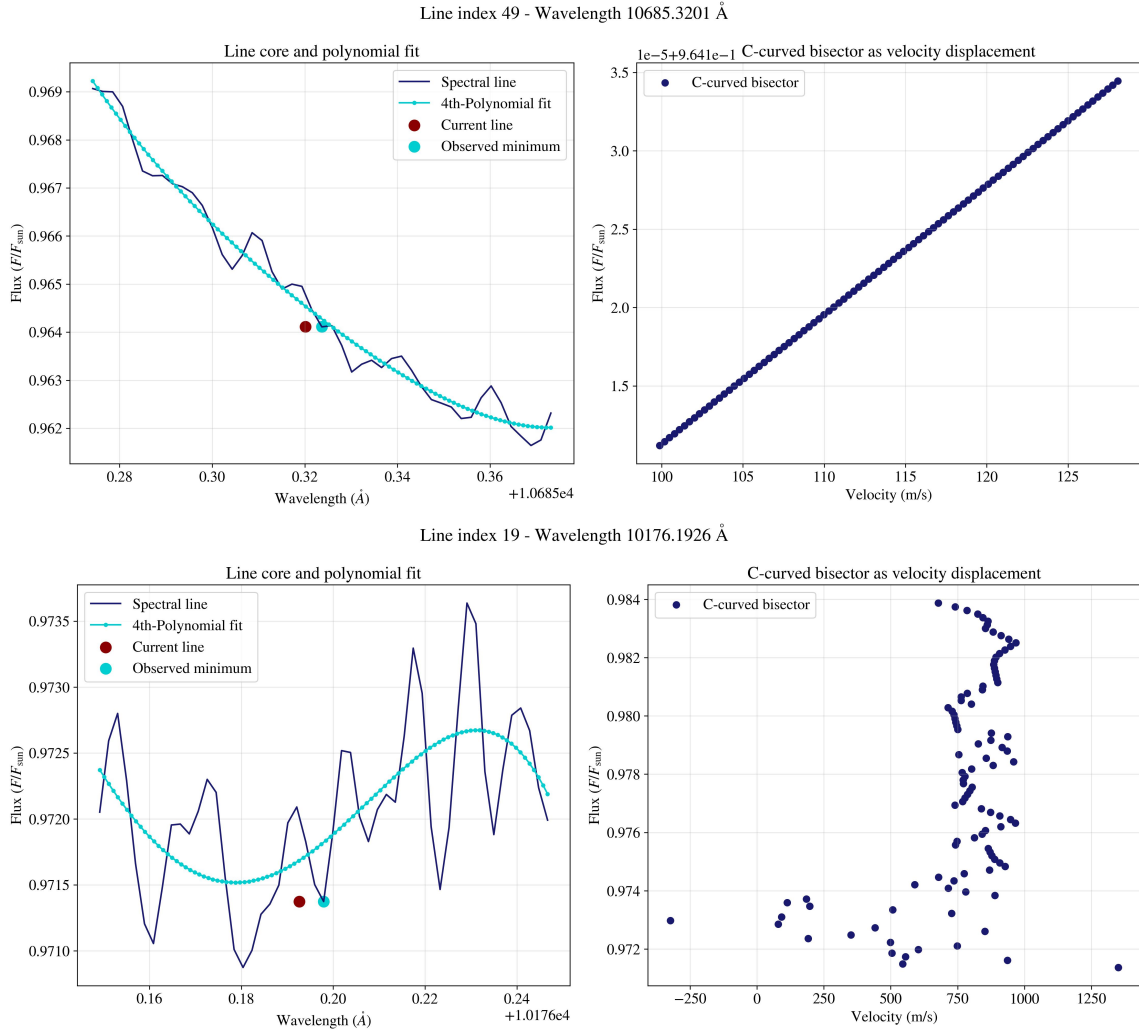


Figure C.7: Examples for discarded lines with the first filter of the visualizer. The line cores and line bisectors of the two plots shows one or more of the conditions presented.

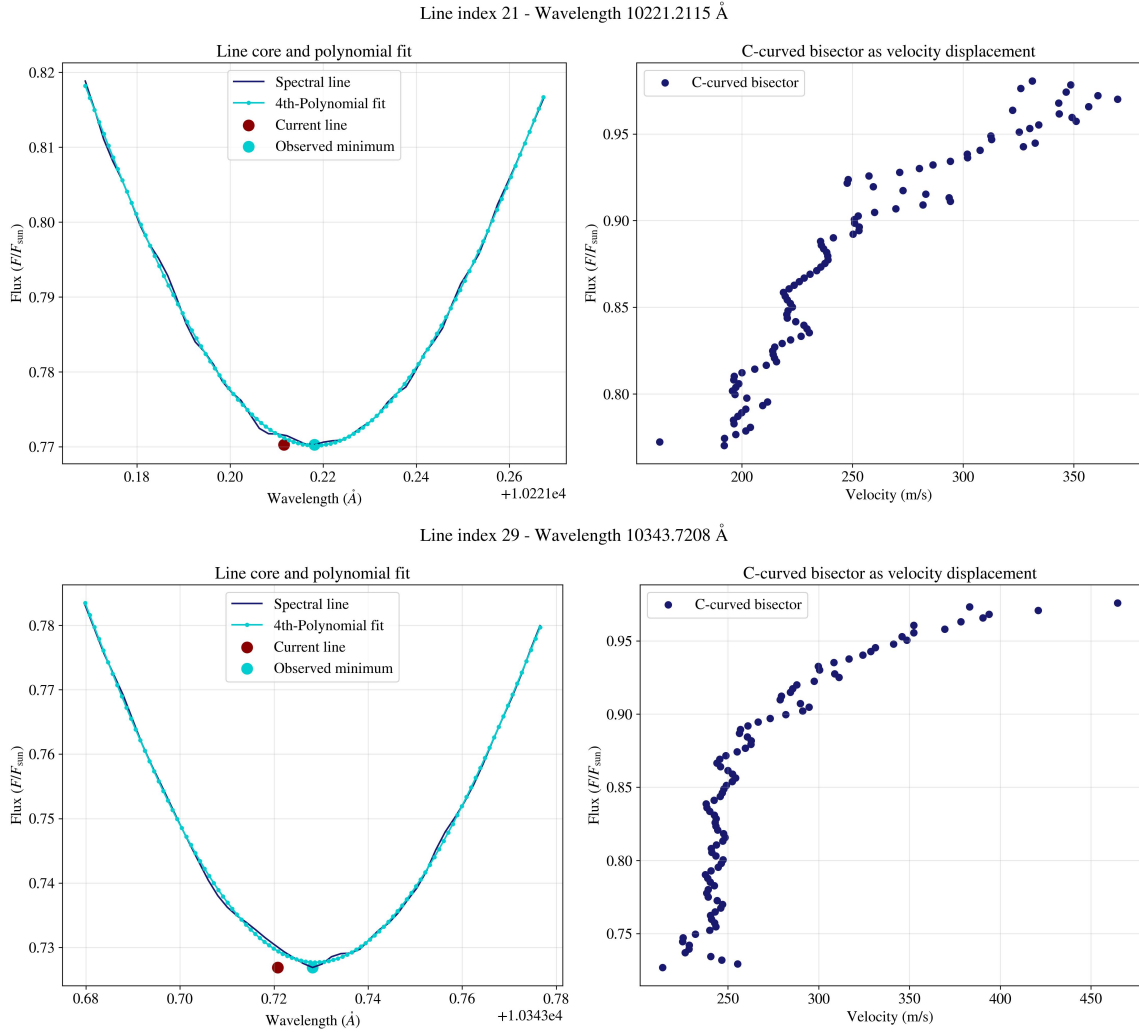


Figure C.8: Examples for accepted lines with the first filter of the visualizer.

**Note:** Make sure that the visualizer is closed after running another cell code.

To extract the Dataframe with the lines to discard or for further analysis run the next cell.

```
#Return the lines which are added to the dataframe of deleting
lines

Filtered_lines_1 = app.return_lines()

#Save the selected lines to drop

Filtered_lines_1['Line'].to_excel('Dropped lines first filter.
```

```
    'xlsx', index=False)
```

The next cell saves the filtered lines in an Excel type file.

```
index_to_drop_1 = Filtered_lines_1.index.values

#Drop the selected lines
New_values_1 = Values_first_filter.drop(index_to_drop_1).
    reset_index(drop=True)

#Save them in a excel file
New_values_1['Nave line'].to_excel('Nave list first filter.
    'xlsx', index=False)
```

The second part of the code calculates the three signatures of convection for the filtered lines.

With this dataset, only run the cell corresponding to the new list of filtered lines for calibration.

```
#Lines from the excel file - This list have filtered values
raw_lambda = pd.read_excel(r"C:\Users\clauw\Documents\
    Programming\Final-Project\Project\Visualizer\Data\Nave list
    first filter.xlsx")
```

For the test example we provide a list for filtered lines in the file `Nave list first filter.xlsx`. Then, run the cell to redefine the closer lines and the corresponding windows of 50 mÅ.

```
closer_lines_second_filter = find_minima(raw_data['Wave A'],
    raw_data['nFlux'], raw_lambda['Nave list'])

local_points_second_filter = width_minima(
    closer_lines_second_filter, raw_data, 0.05)
```

Then, run the next cell for applied the second filter and calculate the three signatures of convection.

```
Values_second_filter, Local_second_filter, Fit_second_filter =
    Second_Filter(local_points_second_filter,
```

```
closer_lines_second_filter['Nave list'])
```

This function calculates the observed wavelength based on the fourth-order polynomial fit. Then, uses the different relations related to the signatures of convection. To display the visualizer of the second filter, uncomment the following line code in the cell corresponding to it

```
#CHANGE THIS LINE - The order: local_points, values, fit
app_2 = OutlierViewer(root, Local_second_filter,
Values_second_filter,Fit_second_filter)
```

**Note:** Make sure that the visualizer is closed after running another cell code.

We recommend eliminating the lines that are affected by noise or don't follow the general behavior on the three signatures of convection. These are blended lines. An example of this behavior is shown on Figure C.9 and an example of accepted lines is shown in Figure C.10.

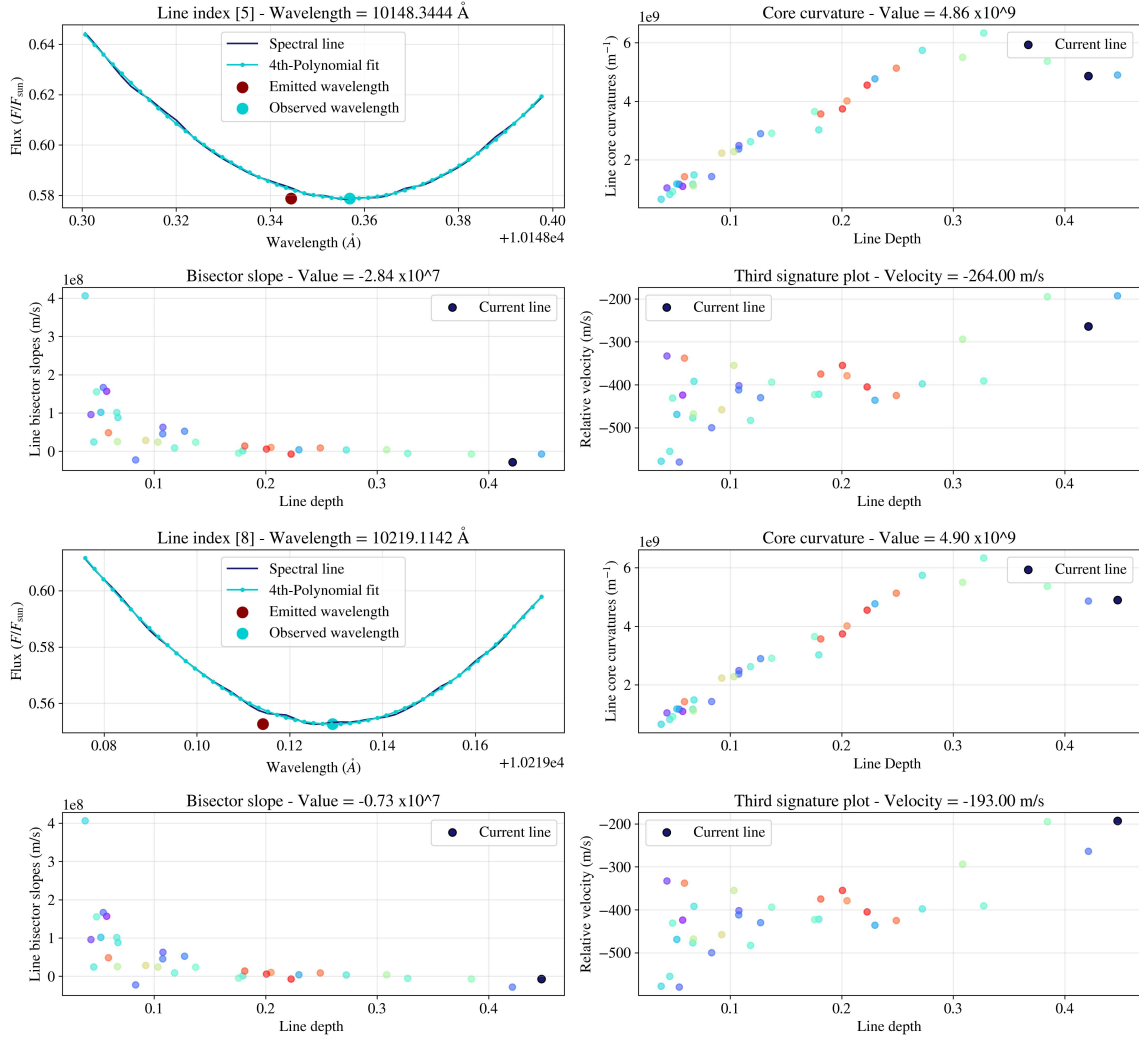


Figure C.9: Examples for discarded lines with the second filter of the visualizer.

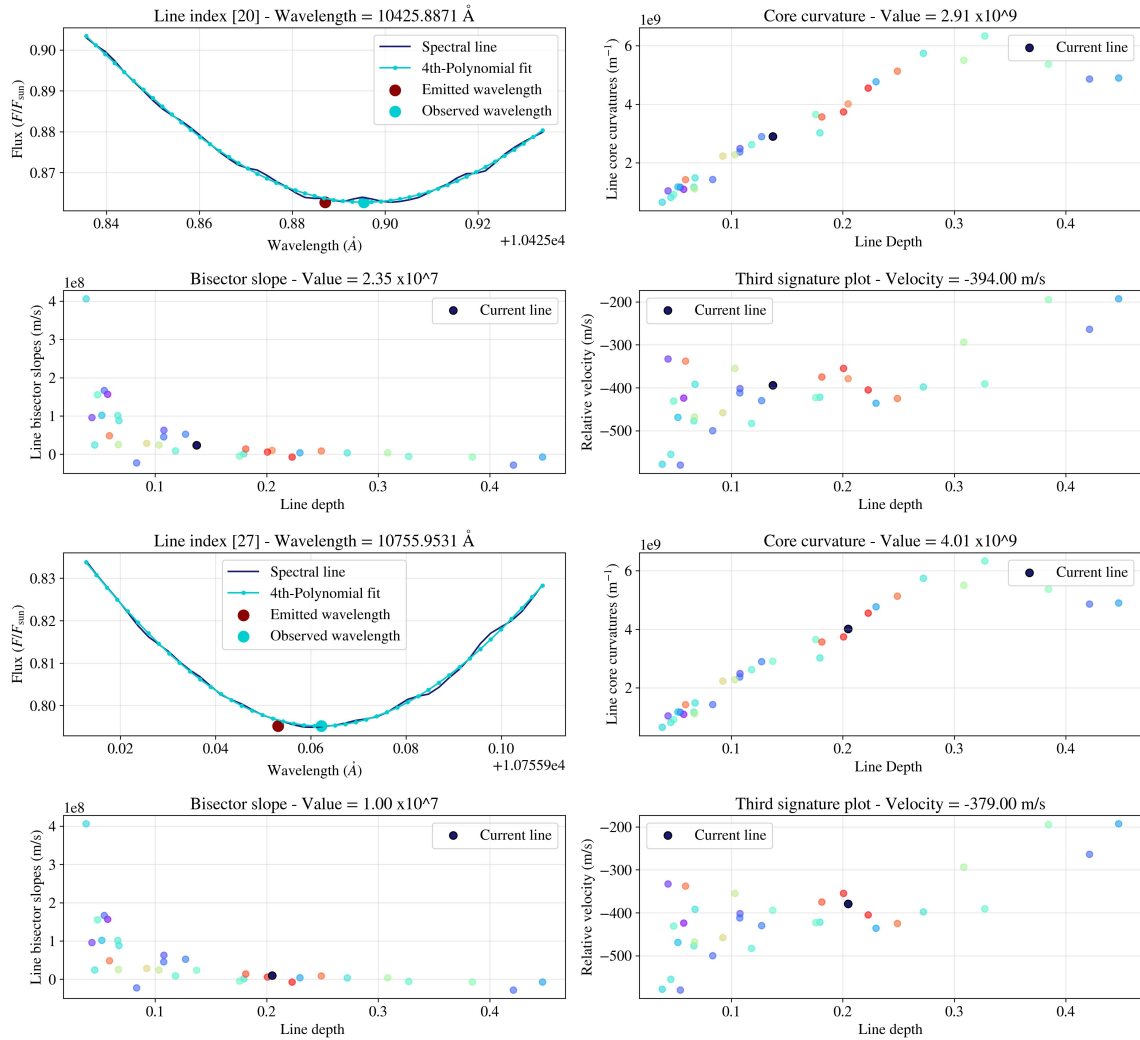


Figure C.10: Examples for accepted lines with the second filter of the visualizer.

To extract the Dataframe with the lines to discard or for further analysis run the next cell.

```
Filtered_lines_2 = app_2.return_lines()

#Save the selected lines to drop
Filtered_lines_2['Line'].to_excel('Dropped lines second filter
.xlsx', index=False)
```

The next cell saves the filtered lines in an Excel type file.

```
index_to_drop_2 = Filtered_lines_1.index.values
```

```
#Drop the selected lines
New_values_2 = Values_second_filter.drop(index_to_drop_2).
    reset_index(drop=True)

#Save them in a excel file
New_values_2.to_excel('Second_filter.xlsx', index=False)
```

After the process, the resulting table is the definitive blend-free list of Fe I lines.

# Bibliography

- [1] D. Gray. The third signature of stellar granulation. *The Astrophysical Journal*, 697(2):1032, May 2009.
- [2] D. Hamilton and J. B. Lester. A technique for the study of stellar convection: The visible solar flux spectrum. *Publications of the Astronomical Society of the Pacific*, 111(763):1132, September 1999.
- [3] D. Dravins, L. Lindegren, and A. Nordlund. Solar granulation - influence of convection on spectral line asymmetries and wavelength shifts. *Astronomy and Astrophysics*, 96:345–364, March 1981.
- [4] P. Foukal. *Solar Astrophysics*. Cambridge research and instrumentation, 1990.
- [5] David F. Gray and T. Pugh. The third signature of granulation in bright-giant and supergiant stars. *The Astronomical Journal*, 143(4):92, March 2012.
- [6] B. Oostra and P. C. Vargas Muñoz. The differential redshift of titanium lines in k stars. *Revista mexicana de astronomía y astrofísica*, 58(2):173–180, 2022.
- [7] G. Nave, S. Johansson, R. C. M. Learner, A. P. Thorne, and J. W. Brault. A new multiplet table for fe i. *The Astrophysical Journal Supplement Series*, 94:221, September 1994.
- [8] A. Reiners, N. Mrotzek, U. Lemke, J. Hinrichs, and K. Reinsch. The iag solar flux atlas: Accurate wavelengths and absolute convective blueshift in standard solar spectra. *Astronomy and Astrophysics*, 587:A65, March 2016.

- [9] M. Ellwarth, B. Ehmann, S. Schäfer, and A. Reiners. Convective characteristics of fe i lines across the solar disc. *Astronomy and Astrophysics*, 680:A62, December 2023.
- [10] E. Priest. *Solar Magnetohydrodynamics*. Kluwer, 1982.
- [11] J. M. Malherbe. Jules janssen: The birth of solar physics, the foundation of meudon observatory and the mont blanc adventure (1875-1895). *HAL CNRS*, August 2022.
- [12] H. H. Plaskett. Solar granulation. *Monthly Notices of the Royal Astronomical Society*, 96:402, March 1936.
- [13] S. A. Hamouda, F. Alfarjani, and F. Y. Elfituri. Sunspots production and relation to other phenomena: A review. *International Journal of Science and Research Methodology*, 06 2018.
- [14] B.W. Carroll and D.A. Ostlie. *An Introduction to Modern Astrophysics*. Cambridge University Press, 2017.
- [15] J. Tatum. Stellar atmospheres, January 2017.
- [16] D. F. Gray and B. Oostra. The solar-flux third granulation signature. *The Astrophysical Journal*, 852:42, January 2018.
- [17] Henri Van Regemorter. Spectral line broadening. *Annual Review of Astronomy and Astrophysics*, vol. 3, p. 71, 3:71, 1965.
- [18] T. A. Nieminen. Solar line asymmetries: Modelling the effect of granulation on the solar spectrum. *arXiv*, August 2017. arXiv:1708.06408 [astro-ph].
- [19] C. Allende Prieto and R. J. Garcia Lopez. Fe i line shifts in the optical spectrum of the sun. *Astronomy and Astrophysics Supplement Series*, 129:41–44, April 1998.
- [20] I.S. McLean. *Electronic Imaging in Astronomy: Detectors and Instrumentation*. Springer Praxis Books. Springer Berlin Heidelberg, 2008.

- [21] John P. Boyd. *Solving Transcendental Equations: The Chebyshev Polynomial Proxy and Other Numerical Rootfinders, Perturbation Series, and Oracles*. SIAM, October 2014.
- [22] J. S. Aponte. *Medición de la Velocidad Convectiva en la Fotosfera Solar*. Bachelor's thesis, Universidad de los Andes, 2017.
- [23] Alessandro Cacciani, Runa Briguglio, Fabrizio Massa, and Paolo Rapex. Precise measurement of the solar gravitational red shift. *Celestial Mechanics and Dynamical Astronomy*, 95:425–437, May 2006.
- [24] Barbara Ryden. *Introduction to Cosmology*. Cambridge University Press, 2016.
- [25] F. Stief, J. Löhner-Böttcher, W. Schmidt, T. Steinmetz, and R. Holzwarth. Convective blueshifts in the solar atmosphere - ii. high-accuracy observations of the fe i 6173.3 Å line and deviations of full-disk dopplergrams. *Astronomy and Astrophysics*, 622:A34, February 2019.
- [26] David F. Gray. *The Observation and Analysis of Stellar Photospheres*. Cambridge University Press, 3 edition, 2005.
- [27] David F. Gray and Kevin I. T. Brown. Precise spectroscopic radial velocity measurements using telluric lines. *Publications of the Astronomical Society of the Pacific*, 118(841):399, March 2006.
- [28] David F. Gray. Empirical decoding of the shapes of spectral-line bisectors. *The Astrophysical Journal*, 710(2):1003, January 2010.
- [29] H. Griem. *Spectral Line Broadening by Plasmas*. Elsevier, 2012.
- [30] S. Owocki. PHYS-633: Introduction to Stellar Astrophysics. Course notes on stellar atmospheres, radiative transfer, spectral lines, and stellar structure. Version of March 27, 2024, 2024.